Membrane tension orchestrates rear retraction in matrix directed cell migration

Joseph H.R. Hetmanski[1], Henry de Belly[2], Ignacio Busnelli[3], Tom Waring[4], Roshna V. Nair[5], Vanesa Sokleva[1], Oana Dobre[1], Angus Cameron[6], Nils Gauthier[7], Christophe Lamaze[8], Joe Swift[1], Aránzazu del Campo[9], Tobias Starborg[1], Tobias Zech[4], Jacky G.Goetz[3], Ewa K. Paluch[2, 9], Jean-Marc Schwartz[1] and Patrick T. Caswell[1*]

[1]Wellcome Trust Centre for Cell-Matrix Research, School of Biological Sciences, Faculty of Biology, Medicine and Health, University of Manchester, Manchester Academic Health Science Centre, Manchester, U.K.

[2]MRC Laboratory for Molecular Cell Biology, University College London, London WC1E 6BT, United Kingdom; Institute for the Physics of Living Systems, University College London, London WC1E 6BT, United Kingdom.

[3]INSERM UMR_S1109, Tumor Biomechanics, Strasbourg 67200, France; Université de Strasbourg, Strasbourg 67000, France; Fédération de Médecine Translationnelle de Strasbourg (FMTS), Strasbourg, F-67000, France.

[4]Institute of Translational Medicine, Cellular and Molecular Physiology, University of Liverpool, Liverpool, England, UK

[5]INM-Leibniz Institute for New Materials, Campus D2 2, 66123, Saarbrücken, Germany.

[6]Barts Cancer Institute, Queen Mary University of London, Charterhouse Square, London EC1M 6BQ, UK.

[7]IFOM, The FIRC Institute for Molecular Oncology, Milan 20139, Italy.

[8]Institut Curie - Centre de Recherche, PSL Research University, CNRS UMR3666, INSERM U1143, Membrane Dynamics and Mechanics of Intracellular Signaling Laboratory, 75248 Paris cedex 05, France.

[9]Department of Physiology, Development and Neuroscience, Downing Street, University of Cambridge, Cambridge, CB2 3DY, UK.

*Lead contact, correspondence to: patrick.caswell@manchester.ac.uk

Summary

In development, wound healing and cancer metastasis vertebrate cells move through 3D interstitial matrix, responding to chemical and physical guidance cues. Protrusion at the cell front has been extensively studied, but the retraction phase of the migration cycle is not well understood. Here we show that fast moving cells guided by matrix cues establish positive feedback control of rear retraction by sensing membrane tension. We reveal a mechanism of rear retraction in 3D-matrix and durotaxis controlled by caveolae, which form in response to low membrane tension at the cell rear. Caveolae activate RhoA-ROCK1/PKN2 signalling via the RhoA-GEF Ect2, to control local F-actin organisation and contractility in this subcellular region and promote translocation of the cell rear. A positive feedback loop between cytoskeletal signalling and membrane tension leads to rapid retraction to complete the migration cycle in fast moving cells, providing directional memory to drive persistent cell migration in complex matrices.

Introduction

Cell migration is a fundamental process that underpins development, health and disease, and is characterised by a cycle of protrusion of the front and retraction of the rear[1]. In 3D matrix, cells move both individually and collectively[2], and in cancer epithelial-mesenchymal transition (EMT) drives the dissemination of elongated single cells to form distant metastases even at very early stages in tumour development[3]. Whilst the mechanisms that govern protrusion are well characterised[4], how retraction

of the cell rear is controlled to complete the migration cycle is still under debate[5]. Contractility driven by the action of non-muscle myosin II (NMII) on actin filaments is key for the generation of force required to actively retract the rear, and RhoGTPase signalling (in particular RhoA) is critical in determining NMIIA/B activity[6]. However, the mechanisms that control rear retraction in restrictive 3D-matrix such as the interstitial fibrillar matrix environment encountered by metastatic cancer cells in vertebrates is not well understood.

The plasma membrane is the physical barrier between intracellular and extracellular environments, and plays an important role in cell migration by both organising signalling and by exerting force (tension) on the underlying cytoskeleton[7–9]. Membrane tension resists membrane deformation, and is established in cells by the in plane tension in the lipid bilayer and membrane to cortex attachment[9]. Membrane tension was thought to propagate rapidly across cells, but recent evidence indicates that the cytoskeleton plays a role in resisting membrane flow[10], allowing cells to establish differential membrane tension across their surface. Membrane tension has recently been shown to be a mechanical signal that regulates formation of focal adhesion complexes[11] and the organisation of actin networks[12] at the leading edge of migrating cells on 2D substrates. Biophysical models have suggested that membrane tension at the cell rear might promote retraction by exerting force[13], however experimental evidence suggests that membrane tension is lower at the rear of migrating fish keratocytes in 2D[14]. In addition, the movement of membrane through endocytic traffic has been postulated to play an important role in gathering membrane from the cell rear for reutilisation at the front[15]. We set out to determine how the cell rear is actively retracted in mammalian cells moving within physiological 3D matrix, focusing on the dynamics of the plasma membrane in this subcellular region.

Results

Rear retraction in 3D matrix and durotaxis is a fast dynamic process

Invasive cancer cells moving within fibrillar collagen and fibronectin 3D cell-derived matrix (CDM)[16,17] followed the topology of fibrils with defined lamellipodial and filopodial protrusions at the cell front[18,19] (Figure 1A; S1A), similar to on 2D substrates. The retracting rear region of the cell was rounded and rapidly translocated with few small retraction fibres, and adhesion complexes or long retraction cables were rarely observed here (Figure 1A; S1G; Movie S1). In the absence of a chemotactic gradient, we hypothesised that the direction of migration up or down bundles of matrix fibrils could be determined by the physical properties of the matrix. Indeed, atomic-force microscopy (AFM) revealed an increase in matrix rigidity directly in front of moving cells (Figure 1A), suggesting strain stiffening of matrix by moving cells[20] could maintain or generate polarity to guide the direction of cell migration. Local softening of the matrix with magnetic trypsin-coated beads[21] (which did not destroy matrix architecture, Figure S1B) established a gradient of rigidity up to 2mm from the targeted area (Figure 1B), and within this gradient region the direction of cell migration over several hours could be changed from random such that cells orientated and moved toward stiffer matrix at a similar rate to cells in untreated matrix (Figure 1B; Movie S1). On 2D substrates, cells responded to a steep gradient of rigidity (>30kPa/mm; Figure 1C) by moving towards the stiffer substrate with a similar rounded and rapidly moving rear that orientated toward the soft substrate (Figure 1C; S1C; Movie S1). These data indicate that cells in 3D-matrix follow mechanical cues, and share morphology with cells migrating in 2D durotactic gradients.

A front-rear membrane tension differential in fast moving cells

Analysis of membrane dynamics at the rear of rapidly moving cells in 3D-matrix suggested that over the timescale of rapid retraction the plasma membrane accumulated, but significant internalisation of labelled membrane was not observed (Figure S1D-E; Movie S2). Membrane accumulation could result in lower plasma membrane tension[9], and we therefore assessed membrane tension by pulling membrane tethers at the cell front and rear[11,14]. Tethers were extracted using an optical trap and the restoring force on the trap was used as a readout of effective membrane tension, which depends on

the in plane tension and the level of attachment between the membrane and the underlying cytoskeleton[9]. We found that there was no significant difference in membrane tension at the cell front versus the cell rear in cells migrating on uniform stiff substrates or on glass (Figure 1D-E; S1F). However, in durotactic cells migrating toward stiffer substrate in a 2D rigidity gradient, membrane tension was significantly lower at the cell rear compared to the front (Figure 1D-E; S1F), suggesting that durotactic cells show front rear polarity through establishment of a membrane tension differential.

In order to analyse membrane tension in cells within a 3D-matrix (and therefore inaccessible via optical trapping) we used Flipper-TR, a small molecule that intercalates into membranes and indicates in-plane membrane tension through changes in fluorescence lifetime of the probe[22]. Live cells showed a striking decrease in fluorescence lifetime specifically at the cell rear (Figure 1F), suggesting that in-plane membrane tension is significantly lower at the rear of cells moving in 3D matrix.

Caveolae accumulate at the rear of fast moving cells

Caveolae are plasma membrane invaginations that can act as a route for endocytosis, but they also play a mechanoprotective role by flattening in response to increased membrane tension[23–27]. Caveolin-1 (a major component of caveolae) and caveolae have previously been shown to polarise at the rear of migrating endothelial cells, fibroblasts and neurons[28–30], although in metastatic cancer cells this is not always observed[31]. We hypothesised that caveolae may form as a consequence of the decrease in membrane tension at the cell rear. We observed caveolin-1 localised to the rear of fast moving cancer cells in 3D matrix (Figure S1G; S2A). Cavin-1, a critical structural component of caveolae[24], was also found to accumulate around the rear of fast moving cancer cells in 3D matrix (Figure 2A; S2B-C) and co-localised with caveolin-1 (Figure 2A). Caveolin-1 and cavin-1 containing structures appeared close to the plasma membrane around the rear of cells moving in 3D and on 2D rigidity gradients (Figure 2A-C; S2D-H) and in cancer cells escaping spheroids in 3D-matrix (which share the elongated morphology of cells moving in 3D CDM; Figure 2D-F). Fibroblasts (MEFs and TIFs) were on average slow moving, elongated and poorly polarised in 3D matrix (Figure S2I-K) and on 2D rigidity gradients were not persistently motile, and did not show a membrane tension differential (Figure S2L). However, a proportion of fibroblasts migrated rapidly in 3D matrix with similar morphology to cancer cells and showed cavin-1 accumulation at the cell rear (Figure S2M-O; Movie S3).

Cavin-1 also colocalised closely with EHD2, which stabilises caveolae at the plasma membrane[32] (Figure 2G), which suggests that relatively stable caveolae form at the rear of fast moving cells. By correlating light microscopy with serial block face scanning electron microscopy (EM), we observed structures that resembled caveolae where caveolin-1 accumulated at the rear of moving cells, but not in other regions of the cells (e.g. perinuclear accumulation of internal caveolin-1; Figure S2P; Movie S4). We correlated light microscopy with higher resolution serial transmission EM (sTEM) and acquired stitched high-resolution TEM images of serial sections (every 100 nm, 65 sections, 6.5 μm) to fully reconstruct migrating cells at nanoscale. TEM demonstrated that caveolae were enriched at the membrane at the rear of the cells in 3D matrix (Figure 2H). Segmentation of caveolae and caveolae-associated vesicles at the rear of the cell revealed numerous individual and multilobed structures, and interestingly many of these possessed a clear 'neck' connected to the plasma membrane[33]. These data indicate that fast moving cells in 3D matrix accumulate caveolae at the rear, which could act as a vast membrane reservoir to collect accumulating membrane.

Caveolae respond to low membrane tension to form at the cell rear

Because caveolae formation is sensitive to membrane tension[23], we used osmotic shock to acutely manipulate membrane tension[11,23]. Introduction of 50% hypo-osmotic medium into the imaging chamber opposed caveolae formation at the rear of cells in 3D matrix and in durotactic gradients, whilst internal mCherry-caveolin-1 in the perinuclear region was relatively unchanged, and forward movement of the rear was suppressed (Figure 3A-B; S3A-C; Movie S5). Returning cells to isotonic medium was sufficient to allow re-establishment of caveolae and rear retraction (Figure 3A-B; Movie

S5). Live imaging of mCherry-caveolin-1 in cells transferred from hypo-osmotic to isotonic medium demonstrated a rapid increase in the average fluorescence intensity of caveolin-1 structures around the cell rear concomitant with re-establishment of rear retraction, whilst the average intensity of caveolin-1 structures in the rest of the cell remained relatively constant (Figure 3C). This indicates that caveolin-1 accumulation at the cell rear does not coincide with removal of caveolin-1 structures from other regions of the cell, rather that caveolin-1 accumulation is perhaps consistent with diffusion in the plasma membrane giving rise to higher average intensity structures. These data suggest caveolae are dynamic structures that can form spontaneously in response to low membrane tension at the rear, rather than being trafficked from other regions of the cell.

In order to locally influence membrane tension in live cells, we expressed constitutively active (CA) ezrin mutant (ezrin T567D-GFP; relieves autoinhibition[34]) to promote membrane-cortex attachment and increase membrane tension[35,36], and took advantage of the finding that this protein accumulates specifically around the rear of cells in 3D matrix (Figure 3D). CA-ezrin significantly abrogated the rate of rear retraction, to a greater extent than wild type ezrin (Figure 3D), and prevented cavin-1 accumulation at the cell rear (Figure 3E). Furthermore, this mutant opposed the membrane tension differential observed in cells moving on 2D durotactic gradients (Figure 3F). Taken together, these data show that caveolae respond to a local decrease in membrane tension to form and become stabilised at the cell rear, and promote retraction of the migrating cell rear.

Caveolae activate RhoA at the cell rear to promote retraction

Caveolin-1 has been implicated in the regulation of RhoGTPases, cell polarity, cell migration and wound healing in the mouse dermis[24,37,38], but the function of caveolae at the rear of migrating cells or role of caveolae/caveolin-1 in rear retraction is not known. In 3D matrix, knockdown of caveolin-1 with either of two independent siRNA oligonucleotides significantly reduced the speed of migration over long timelapses and increased cell length (Figure S4A-D). Caveolin-1 knockdown had little impact on the ability of cells to generate and extend protrusions, but reduced the distance that the cell rear translocated over a 5 minute time period (Figure 4A, Figure S4E-F), demonstrating a clear retraction defect in 3D migration. EHD2 regulates the stability/maturation of caveolae at the plasma membrane[32], and EHD2 knockdown resulted in loss of caveolin-1 localisation at the rear of cells moving in 3D matrix (Figure S4G). EHD2 knockdown cells showed a decreased rate of migration over long time courses, and cells were elongated and showed defective cell rear translocation (Figure S4G-H), supporting a role for caveolae in rear retraction.

Because caveolae have previously been implicated in the regulation of RhoGTPases[24], we hypothesised that caveolae could play a role in the activation of RhoA to organise the actin cytoskeleton and mediate rear retraction. Using a location biosensor to report on active RhoA localisation (GFP-AHPH[39,40]), we observed a punctate distribution of active RhoA concentrated around the retracting rear of cells moving in 3D matrix and in durotaxis (Figure S4I-J). Active RhoA and caveolin-1 co-distributed at the rear of cells moving in 3D matrix and durotactic gradients (Figure 4B; S4K; Movie S8) and high resolution imaging revealed partial co-localisation (Figure 4C), suggesting that caveolae and active RhoA localise in close proximity at the rear of migrating cells. Next, we used a RhoA FRET biosensor to show that RhoA activity, as expected, was elevated at the rear of cells migrating in 3D matrix, but knockdown of caveolin-1 significantly abrogated RhoA activation at the cell rear (Figure 4D). Increasing membrane tension with osmotic shock (which impairs caveolae formation; Figure 3A-C) similarly impaired the activation of RhoA (Figure 4E, S4L), suggesting that caveolae sense and respond to low membrane tension at the cell rear and activate RhoA in this subcellular region.

RhoA coordinates rear retraction by organising F-actin at the cell rear

RhoA plays a key role in regulating actomyosin contractility and retraction of the rear in migrating cells in 2D[1], and we found that RhoA knockdown cells showed a clear defect in rear retraction in 3D migration[41] (Figure S4M). Having identified a rear retraction defect associated with a caveolae-RhoA

pathway, we analysed how this pathway influenced the organisation of actin in cells migrating in 3D. Knockdown of caveolin-1 had very little effect on the intensity of F-actin towards the front of cells moving in 3D matrix, but strikingly decreased F-actin intensity at the rear (Figure 4F). Similarly, Y27632, a selective inhibitor of the ROCK and PKN RhoA effector kinases, decreased F-actin intensity in the rear portion of the cell (Figure S4O). Knockdown of RhoA and individual effector kinases ROCK1 and PKN2 (PRK2) selectively abrogated migration speed, F-actin intensity and organisation at the cell rear (Figure 4G-J, S4N-Q). Strikingly, high resolution imaging revealed that F-actin was organised into cables oriented along the front- rear axis at the cell rear which were lost upon ROCK1 and PKN2 (but not ROCK2, PKN1 or PKN3) depletion (Figure 4H, S4Q). Inhibition of Rho effector kinases[42] or knockdown of caveolin-1 significantly abrogated rear retraction independently, but had no additive effect (Figure 4K), suggesting that caveolin-1 and RhoA effector kinases form part of the same regulatory pathway. These data indicate that caveolae activate RhoA-ROCK1/PKN2 signalling modules which organise F-actin specifically at the cell rear and promote actin organisation and contractility.

Ect2 is recruited by caveolae to activate RhoA and promote rear retraction

Caveolae have been linked to RhoA activity, at least in part by preventing RhoA inactivation by p190RhoGAP[38]. However, GEFs that specifically activate RhoA in this context are not known. By using a GFP-trap/mass spectrometry approach to identify GFP-RhoA binding proteins, we uncovered 6 candidates potentially involved in RhoGTPase activation, the GEFs Ect2, Vav2, ARHGEF2 (GEF-H1), PLEKHG5, DOCK1 and its co-factor ELMO2 (Figure S5A and data not shown). Knockdown of these candidates revealed that 4 (Ect-2, Vav2, ARHGEF2 and PLEKHG5) played a role in motility in 3D matrix (Figure S5A-C). Whilst knockdown of Ect2 and PLEKHG5 resulted in an elongated morphology consistent with a defect in retraction (Figure S5B-D), knockdown of Ect2 alone caused a clear defect in rear retraction in cells moving on 3D matrix (Figure 5A). Moreover, knockdown of Ect2, but not Vav2 or PLEKHG5, significantly reduced the activation of RhoA at the rear of cells moving in 3D matrix (Figure 5B), suggesting that Ect2 acts as the main GEF that activates RhoA to mediate rear retraction.

Ect2 is targeted to the membrane after nuclear envelope breakdown to activate RhoA and execute cytokinesis[43–45], and although it is reported to localise predominantly to the nucleus in interphase cells, Ect2 can also activate RhoA to stabilise cell:cell junctions[40,46]. In fast moving cells in 3D-matrix, Ect2 was distributed between the nucleus and cytoplasm, but accumulated at the cell rear where it colocalised with cavin-1 (Figure 5C). Knockdown of caveolin-1, however, suppressed the accumulation of Ect2 at the cell rear without markedly influencing the nuclear-cytoplasmic balance (Figure 5D). This suggests that Ect2 is specifically recruited to the cell rear by caveolae to activate RhoA and promote rear retraction.

Computational models describe persistent movement in mechanically guided cell migration

In order to gain further insight into the dynamic signalling and mechanical events leading to rear retraction of cells within durotactic gradients and upon strain-stiffening of 3D-ECM, we built a mathematical model based on ordinary differential equations (ODEs) to describe the signalling that controls rear retraction. This model was based upon our key findings as outlined above (Figures 1-5) and literature (see methods section for detailed breakdown of all reactions/nodes and parameters). This models the rear domain and considers the interplay between signalling dynamics and mechanical inputs; because we observe caveolae formation in durotactic migration, polarised substrate stiffness is the only external input, transduced from cell-matrix adhesion complexes at the cell front by actomyosin to initiate forwards translocation of the cell and establish a front-rear membrane tension differential (Figure 6A, B). Our model recapitulates signalling occurring at the cell rear in response to mechanical inputs, leading to F-actin organisation and phosphorylation of NMII via ROCK1/PKN2 (Figure 6A, B). We explicitly modelled an initially non-homogenous ‘polarised substrate stiffness’ (set to 100%) to mimic the strain-stiffened state of matrix in front of cells moving in 3D-matrix and the substrate encountered by cells on 2D rigidity gradients, while all other (non-inhibitory) variables were set as initially zero. Simulations of this non-homogenous modelled domain showed the output ‘rear

retraction' (conceptualised as directional rear movement towards initially stiffer areas, such that a high value corresponds to persistent, fast movement and a low value corresponds to slow migration and/or random, non-persistent directionality) to rapidly increase to a high steady state, while without the external polarised substrate input (uniform throughout), rear retraction levels were negligible (Figure 6C). Sensitivity analysis (Figure S6A) revealed critical model parameters, and halving or doubling critical parameters had little effect on modelled outputs (Figure S6B), suggesting that the model and its overall network topology was robust. Interestingly, if the cell was simulated to transition from a polarised to a uniform substrate, the rear retraction output was near identical to the unperturbed polarised case, while if a cell instead transitioned from a uniform to a polarised substrate then the rear would begin retracting accordingly after the transition (Figure 6C). This indicates that once a rear begins to rapidly retract it can continue to do so independently of the external polarisation conditions. This may reflect the ability of cells to move persistently in disordered 3D matrix and suggests that rear retraction could act as a directional memory to conserve persistent migration in complex matrix.

Simulations of this model were in close agreement with our experimental findings: independent individual reduction of caveolae (knockdown of caveolin-1, EHD2) or RhoA (corresponding to experimental knockdown efficiency) severely reduced F-actin alignment and rear retraction 'speed' (Figure 6D) *in silico*. We could also mimic the reversible osmotic shock protocol, whereby increasing the transition from low to high membrane tension reduced caveolae formation and halted rear retraction, while returning the membrane tension to a decreased state rapidly restored rear caveolae accumulation and efficient retraction (Figure 6E). This gave confidence in the topology and structure of our model and suggested that it could serve as a predictive tool.

Positive feedback reinforcement of RhoA-mediated contractility

During model construction, a potential feedback loop became apparent. We theorised that a gradient of stiffness, transduced by actomyosin contractility generated via integrin-mediated adhesion, would lead to decreased rear membrane tension and formation of caveolae. Because caveolae formation at the cell rear promotes RhoA activation, we predicted a positive feedback loop between RhoA-mediated contractility within the rear domain and caveolae formation via a further decrease in membrane tension (Figure 5A, B). Simulation showed that this feedback loop was a plausible feature of the model, and predicted that it could be broken (and caveolae formation arrested) by inhibition of Rho effector kinases (simulated as an increase in both ROCK1 and PKN2 inactivation rates, *in silico* Y27632 treatment; Figure 6F). Similarly, increasing F-actin turnover, either globally or locally, was predicted to prevent further formation of caveolae and to halt forward movement of the rear (Figure 6G, H).

In order to experimentally verify positive feedback between RhoA signalling and caveolae formation, we first treated cells with Y27632 to inhibit Rho-effector kinases. mCherry-caveolin-1 was rapidly redistributed from the rear of cells migrating in 3D matrix within 10 mins (Figure 7A-B; Movie S6), suggesting that signalling downstream of RhoA through ROCK1/PKN2 is required to maintain positive feedback. Similarly, RhoA knockdown cells failed to recruit mCherry-caveolin-1 to the cell rear in 3D matrix (Figure S7A-B). Knockdown of Ect2, RhoA or ROCK1 suppressed the recruitment of endogenous caveolin-1/cavin-1 to the cell rear in 3D matrix (Figure 7C-E; S7C-D), indicating that RhoA signalling is required to form caveolae at the retracting rear. Furthermore, membrane tension at the rear of cells moving in 3D-matrix was increased by inhibition of Rho-effector kinases (Figure 7G), suggesting that maintenance of low membrane tension requires the RhoA signalling cascade.

Cytochalasin D (CytoD), an agent that can both inhibit actin polymerisation and promote depolymerisation[47], was found to disrupt F-actin and rear caveolae in cells in 3D matrix (Figure S7E). In order to more locally influence F-actin turnover, we used a caged form of CytoD (Nvoc-CytoD[48]; Figure S7F) and analysed the effect of such acute intervention on the formation of caveolae at the rear of cells actively migrating in 3D matrix. Initiating uncaging to release the active compound led to a

reduction in F-actin intensity at the rear and the concomitant redistribution of mCherry-caveolin-1 (Figure 7H; S7G; Movie S7). These data confirm that rear retraction is a dynamic process underpinned by a positive feedback loop centred on the formation of caveolae to amplify RhoA activity at the rear of migrating cells and effect rear retraction.

Discussion

Here we show that cells moving in fibrillar 3D matrix and on durotactic gradients establish a front-rear membrane tension differential, and low membrane tension is sensed at the cell rear by caveolae. Cells follow rigidity gradients on 2D (Figure 1C) and in 3D-matrix (Figure 1B), and in unperturbed 3D-matrix cells strain-stiffen the extracellular matrix in front (Figure 1A), to establish front-rear polarity and in this context active translocation of the rear occurs at >1μm/min. This rapid retraction is mediated by caveolae, which promote contractility signalling by recruiting the RhoAGEF Ect2 to activate RhoA and its effectors ROCK1 and PKN2. Positive feedback could then be established by actomyosin contractility to promote further reduction in membrane tension, caveolae formation and hyperactivation of RhoA. This mechanism explains rapid retraction of the migrating cell rear, allowing single cells to move fast and persistently in 3D matrix and on gradients of rigidity.

Rear retraction in migrating cells is known to require RhoA-mediated signalling to the contractile actin cytoskeleton[1], and in 2D migration some mechanistic detail has emerged revealing how RhoA is regulated and how NMII isoforms organise front rear polarity[49–51]. RhoA activity has also been implicated in driving rearward cortical actin and membrane flow to control the migration of amoeboid cells which lack strong cell-matrix interactions[52,53]. Our study reveals how membrane tension acts as a key mechanical feature of cells moving in gradients of rigidity, to allow formation of caveolae, which in turn coordinate activation of the contractile cytoskeleton. Cells in 3D matrix can strain stiffen their local environment[20] to create or amplify any differences in rigidity that might exist. A gradient of rigidity could generate a membrane tension differential through adhesion complexes at the front of polarised cells, which would encounter higher resistive force resulting in net forward movement of the contractile actin cytoskeleton and lower membrane tension where membrane-cortex interactions are weakened. Using Flipper-TR, we show that the in-plane membrane tension is reduced at the rear of cells moving in 3D (Figure 1F). Optical trap-based tether pulling shows a very similar trend in cells on 2D rigidity gradients, where this approach measures the product of both in-plane membrane tension and membrane cytoskeleton connections. Interestingly, increasing membrane-cytoskeleton attachments using CA-ezrin has a significant effect on caveolae recruitment and rear retraction (Figure 2D, E). This suggests that, in the context of caveolae formation, the in-plane membrane tension and membrane-cytoskeletal linkage could be linked.

Whilst caveolae have been shown to localise to the cell rear in 2D[24,28–31], their function there has been poorly understood. Our data demonstrate that caveolae act to recruit a RhoA GEF, Ect2, which activates RhoA to coordinate the retraction phase of migration. Polarisation of membrane tension (and caveolae) is less apparent on uniformly stiff substrates, but it is possible that caveolae play a similar regulatory role in some cell types during the retraction phase of the migration cycle on these surfaces.

Caveolae are known to function as endocytic carriers[24], but in our study the role of caveolae appears to be related to their capacity to form where the plasma membrane is under low tension. Indeed, acute temporal or spatial manipulation of membrane tension (using osmotic shock or rear-localised CA-ezrin) abrogates caveolae formation and rear retraction (Figure 3). sTEM demonstrate the accumulation of caveolae around the retracting rear membrane, including multilobed structures and caveolae with clear membrane-associated neck structures (Figure 2H). In support of this EHD2, which stabilises the neck of caveolae, is required for rear retraction and localises to caveolae at the cell rear (Figure 2G, S4G). However, in our sTEM images, many caveolae are present close to the retracting rear plasma membrane with no apparent neck (Figure 2H), and it is not clear whether this is a limitation of the z-sectioning approach, or if these represent internal caveolae structures. Given that some

caveolin-1 puncta appear to internalise after breaking the positive feedback loop that establishes rapid retraction (Figure 7), it remains possible that caveolae internalisation can occur from the cell rear and could act as an important step particularly when migrating cells change direction or arrest.

Previous studies have implicated caveolae in substrate stretch-mediated activation of RhoGTPases[54,55], although cell-matrix adhesion complexes play a major role in RhoA activation in response to such uniformly applied strain[56]. Caveolin-1 has been shown to promote RhoA activity by suppressing Src and the RhoA inactivator p190RhoGAP[38], and is implicated in the generation of actomyosin contractility in cancer-associated fibroblasts, activating RhoA to promote reorganisation of stromal matrix[57]. In addition, it is now clear that caveolae play a role in protecting against mechanical strain in numerous cell systems by buffering against increasing membrane tension[23–26]. Our study extends these findings, suggesting that when cells generate directional traction force in a durotactic gradient, contractility within the actin cytoskeleton along the front-rear axis transmits a signal through decreased rear membrane tension that is sensed by caveolae to promote RhoA activation via Ect2, which could itself be directed to the membrane by interaction with lipids, as is the case prior to cytokinesis[43,45]. Downstream of RhoA, the effector kinases ROCK1 and PKN2 each play key roles in actin organisation and rear retraction (Figure 4, S4), and a specific requirement for PKN2 in cell migration has previously been shown in cancer cells and *in vivo*[58,59], suggesting that RhoA effector kinases synergise to control F-actin organisation and contractility in rear retraction. Surprisingly, the effects of caveolae disruption and RhoA signalling intervention are confined to a large region at the back of migrating cells, suggesting that this signal regulating F-actin is compartmentalised to the cell rear. The nucleus is limiting in migration through complex environments and can even rupture under force exerted on it[60–63], and it is therefore possible that this large organelle acts to partition cytoskeletal regulation.

Cell migration is a widely studied phenomenon in 2D, yet still relatively poorly characterised in more physiological 3D environments such as the interstitial matrix encountered by metastatic cancer cells and fibroblasts in wounding[18]. Here, we have identified a mechanism that controls the least well understood phase of the migration cycle, rear retraction. By establishing a positive feedback loop resulting in hyperactivation of RhoA, membrane tension could act as a mechanical signal that allows cells to move rapidly with high directional persistence into fibrotic areas (e.g. wounds) or promote cancer invasion.

Acknowledgements

The Bioimaging Facility microscopes used in this study were purchased with grants from BBSRC, Wellcome and the University of Manchester Strategic Fund. AFM measurements were supported by Dr Nigel Hodson. N15A cells were a kind gift from Prof. Andrew Renehan. We are grateful to Fatima Chunara, Yitong Zhang, Sophie Brett and Eleanor Hinde for technical support. PTC is supported by the MRC (MR/R009376/1), JS is supported by the BBSRC (BB/L024551/1), and The Wellcome Trust Centre for Cell-Matrix Research is supported by grant 203128/Z/16/Z. CLEM experiments were funded by ARC (Programme labellisé, to JG) and by institutional funds from INSERM and University of Strasbourg. IB is supported by ARC (Programme labellisé, to JG) and we are grateful to Luc Mercier for help with the CLEM approach and Cathy Royer (INCI, Strasbourg) for access to TEM.

References

1. Ridley, A. J. *et al.* Cell migration: integrating signals from front to back. *Science* **302**, 1704–9 (2003).

2. Friedl, P. & Alexander, S. Cancer Invasion and the Microenvironment: Plasticity and Reciprocity. *Cell* **147**, 992–1009 (2011).

3. Harper, K. L. *et al.* Mechanism of early dissemination and metastasis in Her2+mammary cancer. *Nature* **540**, 588–592 (2016).

4. Caswell, P. T. & Zech, T. Actin-based cell protrusion in a 3D matrix. *Trends Cell Biol.* (2018). doi:10.1016/j.tcb.2018.06.003

5. Cramer, L. P. Mechanism of cell rear retraction in migrating cells. *Curr. Opin. Cell Biol.* **25**, 591–599 (2013).

6. Ridley, A. J. Life at the Leading Edge. *Cell* **145**, 1012–1022 (2011).

7. Keren, K. Cell motility: The integrating role of the plasma membrane. *Eur. Biophys. J.* **40**, 1013–1027 (2011).

8. Gauthier, N. C., Masters, T. A. & Sheetz, M. P. Mechanical feedback between membrane tension and dynamics. *Trends Cell Biol.* **22**, 527–35 (2012).

9. Diz-Muñoz, A., Fletcher, D. A. & Weiner, O. D. Use the force: Membrane tension as an organizer of cell shape and motility. *Trends Cell Biol.* **23**, 47–53 (2013).

10. Shi, Z., Graber, Z. T., Baumgart, T., Stone, H. A. & Cohen, A. E. Cell Membranes Resist Flow. *Cell* **175**, 1769-1779.e13 (2018).

11. Pontes, B. *et al.* Membrane tension controls adhesion positioning at the leading edge of cells. *J. Cell Biol.* **216**, 2959–2977 (2017).

12. Mueller, J. *et al.* Load Adaptation of Lamellipodial Actin Networks. *Cell* **171**, 188-200.e16 (2017).

13. Keren, K. *et al.* Mechanism of shape determination in motile cells. *Nature* **453**, 475–480 (2008).

14. Lieber, A. D., Schweitzer, Y., Kozlov, M. M. & Keren, K. Front-to-rear membrane tension gradient in rapidly moving cells. *Biophys. J.* **108**, 1599–1603 (2015).

15. Bretscher, M. S. Endocytosis: relation to capping and cell locomotion. *Science* **224**, 681–6 (1984).

16. Cukierman, E., Pankov, R., Stevens, D. R. & Yamada, K. M. Taking cell-matrix adhesions to the third dimension. *Science* **294**, 1708–12 (2001).

17. Bass, M. D. *et al.* Syndecan-4-dependent Rac1 regulation determines directional migration in response to the extracellular matrix. *J. Cell Biol.* **177**, 527–38 (2007).

18. Caswell, P. T. & Zech, T. Actin-based cell protrusion in a 3D matrix. *Trends Cell Biol.* (2018).

19. Paul, N. R. *et al.* alpha-5 beta-1 integrin recycling promotes Arp2/3-independent cancer cell invasion via the formin FHOD3. *J. Cell Biol.* **210**, 1013–1031 (2015).

20. Van Helvert, S. & Friedl, P. Strain Stiffening of Fibrillar Collagen during Individual and Collective Cell Migration Identified by AFM Nanoindentation. *ACS Applied Materials and Interfaces* (2016). doi:10.1021/acsami.6b01755

21. Petrie, R. J., Gavara, N., Chadwick, R. S. & Yamada, K. M. Nonpolarized signaling reveals two distinct modes of 3D cell migration. *J. Cell Biol.* **197**, 439–455 (2012).

22. Colom, A. *et al.* A fluorescent membrane tension probe. *Nat. Chem.* **10**, 1118–1125 (2018).

23. Sinha, B. *et al.* Cells respond to mechanical stress by rapid disassembly of caveolae. *Cell* **144**, 402–413 (2011).

24. Parton, R. G. & del Pozo, M. A. Caveolae as plasma membrane sensors, protectors and organizers. *Nat. Rev. Mol. Cell Biol.* **14**, 98–112 (2013).

25. Cheng, J. P. X. *et al.* Caveolae protect endothelial cells from membrane rupture during increased cardiac output. *J. Cell Biol.* **211**, 53–61 (2015).

26. Lim, Y. W. *et al.* Caveolae Protect Notochord Cells against Catastrophic Mechanical Failure during Development. *Curr. Biol.* **27**, 1968-1981.e7 (2017).

27. Garcia, J. *et al.* Sheath Cell Invasion and Trans-differentiation Repair Mechanical Damage Caused by Loss of Caveolae in the Zebrafish Notochord. *Curr. Biol.* (2017). doi:10.1016/j.cub.2017.05.035

28. Parat, M.-O., Anand-Apte, B. & Fox, P. L. Differential Caveolin-1 Polarization in Endothelial Cells during Migration in Two and Three Dimensions. *Mol. Biol. Cell* **14**, 2372–2384 (2003).

29. Beardsley, A. *et al.* Loss of caveolin-1 polarity impedes endothelial cell polarization and directional movement. *J. Biol. Chem.* **280**, 3541–3547 (2005).

30. Lentini, D. *et al.* Polarization of caveolins and caveolae during migration of immortalized neurons. *J. Neurochem.* **104**, 514–523 (2008).

31. Urra, H. *et al.* Caveolin-1-enhanced motility and focal adhesion turnover require tyrosine-14 but not accumulation to the rear in metastatic cancer cells. *PLoS One* **7**, (2012).

32. Hoernke, M. *et al.* EHD2 restrains dynamics of caveolae by an ATP-dependent, membrane-bound, open conformation. *Proc. Natl. Acad. Sci.* 201614066 (2017). doi:10.1073/pnas.1614066114

33. Ludwig, A. *et al.* Molecular Composition and Ultrastructure of the Caveolar Coat Complex. *PLoS Biol.* **11**, (2013).

34. Gautreau, A., Louvard, D. & Arpin, M. Morphogenic effects of ezrin require a phosphorylation-induced transition from oligomers to monomers at the plasma membrane. *J. Cell Biol.* **150**, 193–203 (2000).

35. Ben-Aissa, K. *et al.* Constitutively active ezrin increases membrane tension, slows migration, and impedes endothelial transmigration of lymphocytes in vivo in mice. *Blood* **119**, 445–454 (2011).

36. Rouven Brückner, B., Pietuch, A., Nehls, S., Rother, J. & Janshoff, A. Ezrin is a Major Regulator of Membrane Tension in Epithelial Cells. *Sci. Rep.* **5**, 1–16 (2015).

37. del Pozo, M. A. *et al.* Phospho-caveolin-1 mediates integrin-regulated membrane domain internalization. *Nat. Cell Biol.* **7**, 901–8 (2005).

38. Grande-García, A. *et al.* Caveolin-1 regulates cell polarization and directional migration through Src kinase and Rho GTPases. *J. Cell Biol.* **177**, 683–94 (2007).

39. Piekny, A. J. & Glotzer, M. Anillin Is a Scaffold Protein That Links RhoA, Actin, and Myosin during Cytokinesis. *Curr. Biol.* **18**, 30–36 (2008).

40. Priya, R. *et al.* Feedback regulation through myosin II confers robustness on RhoA signalling at E-cadherin junctions. *Nat. Cell Biol.* **17**, (2015).

41. Jacquemet, G. *et al.* RCP-driven α5β1 recycling suppresses Rac and promotes RhoA activity via the RacGAP1-IQGAP1 complex. *J. Cell Biol.* **202**, 917–35 (2013).

42. Bain, J. *et al.* The selectivity of protein kinase inhibitors: a further update. *Biochem. J.* **408**, 297–315 (2008).

43. Su, K.-C. C., Takaki, T. & Petronczki, M. Targeting of the RhoGEF Ect2 to the Equatorial Membrane Controls Cleavage Furrow Formation during Cytokinesis. *Dev. Cell* **21**, 1104–1115 (2011).

44. Matthews, H. K. *et al.* Changes in Ect2 Localization Couple Actomyosin-Dependent Cell Shape Changes to Mitotic Progression. *Dev. Cell* **23**, 371–383 (2012).

45. Kotýnková, K., Su, K. C., West, S. C. & Petronczki, M. Plasma Membrane Association but Not Midzone Recruitment of RhoGEF ECT2 Is Essential for Cytokinesis. *Cell Rep.* **17**, 2672–2686 (2016).

46. Ratheesh, A. *et al.* Centralspindlin and α-catenin regulate Rho signalling at the epithelial zonula adherens. *Nat. Cell Biol.* **14**, 1–13 (2012).

47. Casella, J. F., Flanagan, M. D. & Lin, S. Cytochalasin D inhibits actin polymerization and induces depolymerization of actin filaments formed during platelet shape change. *Nature* **293**, 302–305 (1981).

48. Latorre, E. *et al.* Active superelasticity in three-dimensional epithelia of controlled shape. *Nature* **563**, 203–208 (2018).

49. Sastry, S. K. *et al.* PTP-PEST couples membrane protrusion and tail retraction via VAV2 and p190RhoGAP. *J. Biol. Chem.* **281**, 11627–11636 (2006).

50. Raab, M. *et al.* Crawling from soft to stiff matrix polarizes the cytoskeleton and phosphoregulates myosin-II heavy chain. *J. Cell Biol.* **199**, 669–683 (2012).

51. Vicente-Manzanares, M., Ma, X., Adelstein, R. S. & Horwitz, A. R. Non-muscle myosin II takes centre stage in cell adhesion and migration. *Nature Reviews Molecular Cell Biology* (2009). doi:10.1038/nrm2786

52. Paluch, E. K., Aspalter, I. M. & Sixt, M. Focal Adhesion – Independent Cell Migration. *Annu. Rev. Cell Dev. Biol.* **32**, 19.1-19.22 (2016).

53. Neill, P. R. O. *et al.* Membrane Flow Drives an Adhesion-Independent Amoeboid Cell Migration Mode Article Membrane Flow Drives an Adhesion-Independent Amoeboid Cell Migration Mode. *Dev. Cell* **46**, 1–14 (2018).

54. Kawamura, S., Miyamoto, S. & Brown, J. H. Initiation and transduction of stretch-induced RhoA and Rac1 activation through caveolae. Cytoskeletal regulation of ERK translocation. *J. Biol. Chem.* **278**, 31111–31117 (2003).

55. Peng, F. *et al.* RhoA activation in mesangial cells by mechanical strain depends on caveolae and caveolin-1 interaction. *J. Am. Soc. Nephrol.* **18**, 189–198 (2007).

56. Burridge, K. & Guilluy, C. Focal adhesions, stress fibers and mechanical tension. *Exp. Cell Res.* **343**, 14–20 (2016).

57. Goetz, J. G. *et al.* Biomechanical remodeling of the microenvironment by stromal caveolin-1 favors tumor invasion and metastasis. *Cell* **146**, 148–63 (2011).

58. Lachmann, S. *et al.* Regulatory domain selectivity in the cell-type specific PKN-dependence of cell migration. *PLoS One* **6**, (2011).

59. Quétier, I. *et al.* Knockout of the PKN Family of Rho Effector Kinases Reveals a Non-redundant Role for PKN2 in Developmental Mesoderm Expansion. *Cell Rep.* **14**, 440–448 (2016).

60. Wolf, K. *et al.* Physical limits of cell migration: Control by ECM space and nuclear deformation and tuning by proteolysis and traction force. *J. Cell Biol.* **201**, 1069–1084 (2013).

61. Denais, C. M. *et al.* Nuclear envelope rupture and repair during cancer cell migration. *Science (80-.).* **352**, 1–41 (2016).

62. Raab, M. *et al.* ESCRT III repairs nuclear envelope ruptures during cell migration to limit DNA damage and cell death. *Science (80-.).* **352**, 359–362 (2016).

63. Irianto, J. *et al.* DNA Damage Follows Repair Factor Depletion and Portends Genome Variation in Cancer Cells after Pore Migration. *Curr. Biol.* (2017). doi:10.1016/j.cub.2016.11.049

64. Roberts, D. L., O'Dwyer, S. T., Stern, P. L. & Renehan, A. G. Global gene expression in pseudomyxoma peritonei, with parallel development of two immortalized cell lines. *Oncotarget* **6**, (2015).

65. Ishizaki, T. *et al.* Pharmacological properties of Y-27632, a specific inhibitor of rho-associated kinases. *Mol. Pharmacol.* **57**, 976–983 (2000).

66. Yoshizaki, H. *et al.* Activity of Rho-family GTPases during cell division as visualized with FRET-based probes. *J. Cell Biol.* **162**, 223–232 (2003).

67. Hayer, A., Stoeber, M., Bissig, C. & Helenius, A. Biogenesis of caveolae: Stepwise assembly of large caveolin and cavin complexes. *Traffic* **11**, 361–382 (2010).

68. Cukierman, E., Pankov, R., Stevens, D. R. & Yamada, K. M. Taking cell-matrix adhesions to the third dimension. *Science* **294**, 1708–12 (2001).

69. Tse, J. R. & Engler, A. J. Preparation of hydrogel substrates with tunable mechanical properties. *Current Protocols in Cell Biology* **Chapter 10**, Unit 10.16 (2010).

70. Hermanowicz, P., Sarna, M., Burda, K. & Gabry, H. AtomicJ: An open source software for analysis of force curves. *Rev. Sci. Instrum.* **85**, 063703 (2014).

71. Hetmanski, J. H. R., Zindy, E., Schwartz, J. M. & Caswell, P. T. A MAPK-Driven Feedback Loop Suppresses Rac Activity to Promote RhoA-Driven Cancer Cell Invasion. *PLoS Comput. Biol.* **12**, e1004909 (2016).

72. Cardona, A. *et al.* TrakEM2 software for neural circuit reconstruction. *PLoS One* **7**, e38011 (2012).

73. Williams, M. E. *et al.* Cadherin-9 regulates synapse-specific differentiation in the developing hippocampus. *Neuron* (2011). doi:10.1016/j.neuron.2011.06.019

74. Starborg, T. *et al.* Using transmission electron microscopy and 3View to determine collagen fibril size and three-dimensional organization. *Nat. Protoc.* (2013). doi:10.1038/nprot.2013.086

75. Gingras, D., Gauthier, F., Lamy, S., Desrosiers, R. R. & Béliveau, R. Localization of RhoA GTPase to Endothelial Caveolae-Enriched Membrane Domains. *Biochem. Biophys. Res. Commun.* **247**, 888–893 (1998).

76. Lamaze, C. & Torrino, S. Caveolae and cancer: A new mechanical perspective. *Biomed. J.* **38**, 367–79 (2015).

77. Echarri, A. & Del Pozo, M. A. Caveolae - mechanosensitive membrane invaginations linked to actin filaments. *J. Cell Sci.* **128**, 2747–2758 (2015).

78. Zimnicka, A. M. *et al.* Src-dependent phosphorylation of caveolin-1 Tyr-14 promotes swelling and release of caveolae. *Mol. Biol. Cell* **27**, 2090–2106 (2016).

79. Grande-García, A. & del Pozo, M. A. Caveolin-1 in cell polarization and directional migration. *European Journal of Cell Biology* **87**, 641–647 (2008).

80. Breitsprecher, D. & Goode, B. L. Formins at a glance. *J. Cell Sci.* **126**, 1–7 (2013).

81. Ohashi, K. *et al.* Rho-associated kinase ROCK activates LIM-kinase 1 by phosphorylation at threonine 508 within the activation loop. *J. Biol. Chem.* **275**, 3577–3582 (2000).

82. Yang, N. *et al.* Cofilin phosphorylation by LIM-kinase 1 and its role in Rac-mediated actin reorganization. *Nature* **393**, 809–812 (1998).

83. Carlier, M. F. *et al.* Actin depolymerizing factor (ADF/cofilin) enhances the rate of filament turnover: Implication in actin-based motility. *J. Cell Biol.* **136**, 1307–1322 (1997).

84. Hamaguchi, T. *et al.* Phosphorylation of CPI-17, an Inhibitor of Myosin Phosphatase, by Protein Kinase N. *Biochem. Biophys. Res. Commun.* **274**, 825–830 (2000).

85. Morgan, M., Perry, S. V. & Ottaway, J. Myosin light-chain phosphatase. *Biochem. J.* **157**, 687–97 (1976).

86. Hoops, S. *et al.* COPASI - A COmplex PAthway SImulator. *Bioinformatics* **22**, 3067–3074 (2006).

Materials and methods

Cell culture and transient transfection

A2780 human ovarian cancer cells were maintained in RPMI-1640 medium (Sigma-Aldrich) supplemented with 10% (v/v) foetal calf serum, 1% (v/v) L-Glutamine and (v/v) 1% Antibiotic-antimycotic (both Sigma-Aldrich); telomerase-immortalised fibroblasts (TIF) cells, mouse-embryonic fibroblasts (MEF) cells and H1299 human lung cancer cells (expressing control vector or mutant p53-273H) were maintained in Dulbecco's modified Eagle's medium (DMEM, Sigma-Aldrich) containing L-Glutamine and supplemented with 10% (v/v) foetal calf serum, and (v/v) 1% Antibiotic-antimycotic (Sigma Aldrich); and N15A[64] Pseudomyxoma peritonei (PMP) cells were maintained in Dulbecco's modified Eagle's medium (DMEM) (Sigma Aldrich) supplemented with 10% FCS, 25 mM HEPES, 5 µg/ml Insulin, 10 mM L-Glutamine and (v/v) 1% Antibiotic-antimycotic (Sigma Aldrich). All cell lines were incubated at 37 °C in a humidified 5% (v/v) CO2 atmosphere. All siRNAs and fluorescent constructs were transiently transfected by electroporation using a nucleofector (Amaxa, Lonza) using solution T, programme A-23, 3ug DNA / 5µl 20 mM siRNA as per the manufacturer's instructions. Experiments were performed ~24 h after nucleofection unless otherwise stated.

Reagents

ROCK/PKN inhibitor Y-27632 [65] was used at 10 µM; ROCK inhibitor H-1152 was used at 2 µM; actin polymerisation inhibitor Cytochalasin-D (Sigma) was used at 2 µM; caged Cytochalasin-D was developed in the del Campo lab (manuscript in submission) and used at 50 µM as outlined below. siRNAs were as follows: Cav-1 – individual Hs_CAV1_9 FlexiTube 5' AAGCATCAACTTGCAGAAAGA (Qiagen) and Hs_CAV1_10 FlexiTube 5' AAGCAAGTGTACGACGCGCAC (Qiagen) (referred to as Cav-1 siRNA-A and Cav-1 siRNA-B respectively here, all Cav-1 knockdown experiments were performed with each individual siRNA at separate times in comparison with separate control siRNAs); EHD2 – pooled FlexiTube GeneSolution (Qiagen); RhoA – 5' ATGGAAAGCAGGTAGAGTT (Eurofins); ROCK1 – Silencer Select Pre-Designed (Life Technologies, 5' -GCTTGTAGGTGATACACCTTT); ROCK2 – Silencer Select Pre-Designed (Life Technologies, 5'-GAGATTACCTTACGGAAAATT); PKN1-3- SMARTpool siRNA (Dharmacon); PKN-2 – individual 5' GGAGCGCTCTGATGGACA (Eurofins); Ect2 – individual Hs_Ect2_5 FlexiTube 5' TTGCCTAGAGATAGCAAGAAA and Hs_Ect2_7 FlexiTube 5' GTCGCCCGTTGTATTGTACAA; Ect2, Vav2, PLEKHG5, DOCK1, ELMO2 – all pooled Flexitube GeneSolution (Qiagen); ARHGEF2 - SMARTpool: ON-TARGET plus ARHGEF2 siRNA. Sufficient knockdown was achieved with a single transfection after 24h for Cav-1-A; after 72h for ROCK1 and ROCK2; and double transfection after 2x24h for Cav-1-B, RhoA, EHD2, Ect2-A, Ect2-B, Ect2 (pool), Vav2, PLEKHG5, DOCK1, ELMO2 and ARHGEF2. FRET biosensor Raichu-1237X [66] RhoA was kindly provided by Prof. M. Matsuda; mCherry-Caveolin-1 construct [67] was kindly provided by Dr M. Bass; the GFP-AHPH Anillin construct [40] kindly provided by Prof. A. Yap; Emerald-Lifeact construct was kindly provided by Dr C. Ballestrem; farnesylGFP (GFP-membrane) construct was kindly provided by Prof. J Norman; GFP-Paxillin construct was kindly provided by Prof. M. Humphries; GFP-Ezrin wild type (WT) and GFP-Ezrin constitutively active (CA) were from [34]. The following antibodies were used: Mouse anti-Fibronectin (Sigma-Aldrich); Rabbit anti-Caveolin-1 (BD Biosciences); Mouse anti-EHD2 (Santa Cruz Biotechnology, for western blot); Goat anti-EHD2 (Abcam, for IF); Rabbit anti-PTRF (Abcam); Rabbit anti-RhoA (Santa Cruz Biotechnology); Rabbit anti-ROCK1 and Rabbit anti-ROCK2 (both Cell Signalling); Mouse anti-Ect2 (Santa Cruz Biotechnology, for IF); Rabbit anti-Ect2 (kind gift from Dr M. Petronczki, for western blot); Rabbit anti-Vav2 (Abcam); Rabbit anti-ARHGEF2 (GeneTex); Mouse anti-PLEKHG5 (Novus Biologicals); Rabbit anti-DOCK1 (ProteinTech); Goat anti-ELMO2 (Abcam); Mouse anti-Tubulin (DM1A), Mouse anti Akt-2 and Rabbit anti-Erk (Santa Cruz Biotechnology).

SDS-PAGE and quantitative western blotting

Cells were lysed in non-denaturing lysis buffer (200 mM NaCl, 75 mM Tris-HCl, pH 7.4, 15 mM NaF, 1.5 mM Na3VO4, 7.5 mM EDTA, 7.5 mM EGTA, 1.5% (v/v) Triton X-100, 0.75% (v/v) NP-40, 50 µg/ml leupeptin, 50 µg/ml aprotinin, and 1 mM 4-(2-aminoethyl)-benzenesulfonyl fluoride). Lysates were

clarified by centrifugation at 10,000 g for 10 min at 4°C. Cell lysates were resolved under denaturing conditions by SDS-PAGE (4–12% Bis-Tris gels; Invitrogen) and transferred to nitrocellulose membrane. Membranes were blocked with 1x Blocking Buffer (Sigma) and incubated overnight at 4°C with the appropriate primary antibody in 5% BSA and then at room temperature for 1 h with the appropriate fluorophore-conjugated secondary antibody in 1x Blocking Buffer. Membranes were scanned using an infrared imaging system (Odyssey; LI-COR Biosciences). siRNA efficiency was quantified in ImageJ following appropriate normalisation to a relevant loading control.

CDM production

Cell derived matrices were generated according to the method developed by the Yamada lab [68]. Briefly, 6/12-well plastic (Corning) or 35 mm glass bottom (Mattek) plates were coated with 0.2% gelatin (v/v, Sigma Aldrich), crosslinked with 1% glutaraldehyde (v/v, Sigma Aldrich) and quenched with 1M glycine (Thermo Fisher) before TIFs were confluently seeded. DMEM medium supplemented with 0.25% ascorbic acid (v/v, Sigma Aldrich) was changed every 48h for 8 days. Cells were denuded with extraction buffer (20 mM ammonium hydroxide (NH4OH); 0.5% (v/v) Triton X-100) to leave only matrix; finally 1 nm DNAse was used for cleavage of phosphodiester linkages in the DNA backbone.

Gradient CDMs with a stiffness differential were created by softening a region of the CDM using trypsin-coated magnetic beads, as trypsin has been shown to alter the stiffness of CDM [21]. Specifically, 10 µl magnetic trypsin beads (TakaRa) were pipetted onto a CDM and localised with a magnet, such that a small, crescent shaped region of the CDM grown on the circular glass bottom area of the dish (Mattek) was subjected to a high concentration of trypsin beads. CDMs were incubated with magnetic trypsin beads for 10 minutes at 37 °C in a humidified 5% (v/v) CO2 atmosphere, before being washed 3x with PBS(+). Cells were plated onto non-uniform CDMs and imaged ~24 h after magnetic trypsin treatment, where the region of the interface of the softened, trypsin treated CDM (i.e. the area directly above the magnet during treatment) and the untreated CDM was carefully, manually identified and cells within this region subsequently analysed.

Generation of polyacrylamide stiffness gradients (2D durotactic gradients)

Polyacrylamide gels were made according to the Tse and Engler[69] protocol with modification for gradient generation. Briefly, large area glass bottom plates (Nunc/Ibidi) or glass microscope slides (DeltaLab) were functionalised by coating with 0.1M NaOH then with 3-Aminopropyltriethoxysilane (APES, Sigma Aldrich), before being crosslinked with 0.5% glutaraldehyde (Sigma Aldrich) and dried; meanwhile manually cut 18 x 6 mm coverslips were rendered hydrophobic by coating with Dichlorodimethylsilane (DCDMS) for 4 minutes before also being dried. Statically compliant hydrogels were prepared by mixing appropriate concentrations of 40% (w/v) acrylamide, 2% (w/v) bis-acrylamide stock solutions (both Sigma-Aldrich) and distilled water and rapidly polymerized by the enzymatic activity of 1/100 10% (w/v) ammonium persulfate (APS) and 1/1000 Tetramethylethylenediamine (TEMED, both Sigma Aldrich). Acrylamide/bis-acrylamide concentrations for our two gels were: soft – 7.5% acrylamide, 1.5% bis-acrylamide, 91% H_2O; and stiff - 25% acrylamide, 11.25% bis-acrylamide, 63.75% H_2O. Gradients were formed by pipetting 2.7 or 5.4 µl of two different stiffnesses of gel (depending on working distance requirements for subsequent microscopy) approx. 15 mm apart on the aforementioned functionalised glass before engaging the 6 x 18 mm hydrophobic coverslips on the top surface of both gels. Natural diffusion and fluid flow of the two different gels into each other formed a confined 1-D gradient covering the 6 x 18 mm area at an approx. thickness of 50 or 100 µm. Hydrophobic coverslips were removed in distilled water. Gels were then uniformly covered with the heterobifunctional protein cross-linker 0.2mg/ml sufosuccinimidyl-6-(4-azido-2-nitrophenylamino)-hexanoate (sulfo-SANPAH; Thermo-fisher) which required activation by exposure with a 365-nm UV light source for 10 minutes. Finally, cells were coated with 10 µg/ml fibronectin in 50 nM Hepes buffer for 16 h before use.

Atomic force microscopy (3D-CDM)

AFM experiments were conducted on a Nanowizard® 3 atomic force microscope (JPK Instruments AG), which was built onto an LSM 880 confocal microscope (Carl Zeiss AG). Colloidal probes for all experiments were prepared as follows. 10µm diameter polystyrene beads (Polysciences Inc.) were resuspended in ethanol before a drop was applied to a clean microscope slide. Epoxy resin was mixed, and a 20µl pipette tip used to apply a small amount of resin to the slide. A tip-less cantilever (Arrow™ TL2, NanoWorld) was then mounted onto the AFM, and the slide mounted onto the stage. Using the AFM, the cantilever was first lowered onto the epoxy resin, with any excess resin being removed by tapping the cantilever onto the glass surface. The cantilever was then lowered into contact with a single bead and raised, with a visual inspection via brightfield to confirm bead attachment and desired placement. Once attached, the resin was left to dry in air for a minimum of 20 minutes. Colloidal probes were used within 1 day of preparation.

For front/rear stiffness measurements, the cells were kept at 37ºC within a PetriDishHeater™ (JPK Instruments AG) for the duration of the experiment. Cantilever calibration was conducted using the contact-free thermal noise method (at 37ºC within medium) prior to each experiment. Measurements of matrix stiffness were conducted with a threshold of 0.5nN and approach speed of 3µm/s. To obtain front and rear measurements the cantilever was manually positioned close to the pseudopod or cell rear, as determined by observation of direction of cell migration, and five repeat force/distance curves were obtained. To obtain stiffness gradient measurements a series of positions were probed; with an initial measurement at the border of a trypsinised area, followed by additional positions at ~600µm steps away from the area. At each position, an 8x8 grid of force/distance curves was collected within a 100µm^2 area.

All force/distance curves were analysed using the AtomicJ software[70]. Contact points were automatically calculated via the robust golden methodology, and curves fitted using the Sneddon model for spherical indenters assuming a Poisson ratio of 0.5. Mis-identified contact points were manually corrected if the contact point was visually obvious. Curves that could not be accurately fitted by the model were excluded from further analysis. For front/rear measurements, the Young's Modulus for each curve was calculated and then each set of 5 were averaged to obtain a mean stiffness value. For gradient measurements, each set of 64 readings were averaged to obtain a mean stiffness value for the area at each position.

Atomic Force Microscopy (2D gradients)

Reduced Young's Moduli of entire long-axis profiles of polyacrylamide gels were calculated using atomic force microscopy on a Bruker Catalyst mounted on a Nikon Eclipse Ti inverted light microscope, with a Bruker cantilever (OTESPA; 4-10nm tip radius). While the absolute long-axis of the gel containing the stiffness gradient was ~18 mm (see above), the total measurable distance by AFM was the middle 12-13 mm of the gel. Therefore the far left reachable point was taken as distance point 0, the far right point was taken as normalised distance 1 and other points (centre, three quarters etc) were measured and sampled relative to these extrema for all gels. End and centre points were first measured, and then further points were iteratively sampled based on neighbours to locate the position of the steep gradient in all gels. N = 25 to 100 readings were taken around a 2.5-5 µm sided square for each reading. Three gradients were analysed in this manner and showed clear consistency in absolute stiffness values and gradient location. AFM was performed on 100 µm thick gels.

Membrane tension measurements by optical trap

Membrane tension measurements were attained using the optical trap method. Tether pulling experiments were realised using a custom made optical trap (4W 1064nm Laser Quantum Ventus) with a 100x oil immersion objective (CFI Plan Fluor DLL, Nikon) on an inverted microscope (Nikon Eclipse TE2000-U) equipped with a motorised stage (PRIOR Proscan). The optical trap calibration was performed as described[14]. Measurements were performed by attaching

concanavalin-A coated (50 µg/ml) latex beads (1.9µm diameter) to cells. Bead position was recorded in bright field after tether formation. Trap force was then calculated using a custom made ImageJ script. Trap force was measured twice for each cell (front and rear). All polyacrylamide gradients used for membrane tension measurements were 50 µm thick gels to fit within the working distance of the 100x objective.

Live fluorescence imaging

All fluorescent images were acquired using a CSU-X1 spinning disc confocal (Yokagowa) on a Zeiss Axio-Observer Z1 microscope with a 63x/1.40 Plan-Apochromat objective for CDMs or a 63x/1.15 LD C-Apochromat Korr water objective or 100x/1.30 Plan-Neofluar objective for polyacrylamide gradients (as stated) to allow for greater working distance. An Evolve EMCCD camera (Photometrics) and motorised XYZ stage (ASI) was used. The 445, 488, 515 and 561nm lasers were controlled using an AOTF through the laserstack (Intelligent Imaging Innovations (3I)) allowing both rapid 'shuttering' of the laser and attenuation of the laser power. Images were captured using SlideBook 6.0 software (3i). Randomly chosen representative polarised Lifeact-EGFP, Lifeact-Emerald, GFP-AHPH, GFPmembrane, Lifeact-RFP, mCherry-Caveolin-1, GFP-Cavin-1, GFP-Ezrin-WT, GFP-Ezrin-CA and GFP-paxillin expressing cells were captured with the appropriate excitation/emission spectrum and exposure time following ~ 4h spreading time on CDM and ~ 20h spreading time on gradient gels in Ham F12 medium or 1x Opti-Klear medium (Marker Gene Technologies Inc) supplemented with 10% (v/v) FCS (488 nm, 50 ms exposure for GFP-Lifeact or Emerald Lifeact; 488 nm, 10 ms exposure for GFP-AHPH; 488 nm, 100 ms exposure for GFP membrane, GFP-Ezrin-WT and GFP-Ezrin-CA; 561 nm, 50 ms exposure for RFP-Lifeact; 561 nm, 20 ms exposure for mCherry-Caveolin-1) every 15s – 1 minute for 5 - 10 minutes as indicated. Where appropriate, rear translocation was measured for all imaged cells in ImageJ across this 5 minute period by comparing the position of a part of the rear of the cell at the start of the timelapse with the exact same part of the rear at the end of the timelapse. For Colocalisation analysis of Cav-1 and Cavin-1, the Coloc2 tool in ImageJ was used to generate Pearson's correlation coefficients in manually derived rear and perinuclear regions. Images are pseudocoloured using the red hot LUT (ImageJ) where appropriate to reveal differences in intensity.

Forster Resonance Energy Transfer (FRET) imaging of RhoA activity was performed and quantified as described in detail previously [71]. Concisely, randomly chosen polarised Raichu-RhoA expressing cells were captured every 15s for 5 minutes with 3 different excitation/emission spectra: CFP (445 nm) donor – CFP acceptor at 200 ms exposure; YFP (515 nm) donor – YFP acceptor at 50 ms exposure; and CFP donor – YFP acceptor at 200 ms exposure. Ratiometric FRET activity was then calculated by dividing the CFP-YFP channel by the CFP-CFP channel following automated image alignment. The YFP-YFP channel was used to create a binary mask of the cell as it had the best signal to noise. Using this mask, a ring of the outermost 40 pixels of the cell was created and the front and rear quarters of the cell were isolated based on long-axis identification. The average of every ratiometric pixel value in a 40 pixel wide, rearmost 25% area of the cell was then obtained and averaged over the 5 minute timelapse period to obtain the final single 'average rear RhoA FRET ratio' value per cell.

Membrane tension measurements by FLIM microscopy

For membrane tension measurements for cell in 3D CDM, the fluorescent probe Flipper-TR was used. Cells were spread on CDM for 4 hours in normal growth medium which was replaced with imaging medium (1x OptiKlear + 10% FCS) containing 1µM Flipper TR, and incubated at 37˚C for 15 minutes to achieve appropriate labelling prior to imaging. Cells were imaged on a SP8 gSTED microscope using PicoQuant hardware/software for fluorescent lifetime imaging (FLIM) with 488 nm excitation and 575-625 emission and a pixel dwell time of > 19.58 µs. Following imaging, a double exponential was fit to ensure a close fit (chi squared < 1.5) and the counts per pixel and lifetime per pixel images exported as 256x256 pixel single time-point, single Z-plane images. For quantification, membrane regions at the cell rear and cell front were manually identified using the count per pixel images, and the mean average lifetimes measured by assigning these front/rear ROIs to the lifetime per pixel images. For the

lifetime representative images, the lifetime per pixel image was smoothed by application of a Guassian blur with 1.0 pixel radius, multiplied by a mask created using the counts per pixel image to remove background/matrix lipid staining, and recoloured with a 16 colour LUT.

Long term cell migration assay

Cells were seeded at sparse (<25%, ~50,000 cells/well) confluency in typical growth medium on 6/12-well CDMs and allowed to spread for ~ 6h. Images were acquired on an Eclipse Ti inverted microscope (Nikon) using a 20x/ 0.45 SPlan Fluar objective, the Nikon filter sets for Brightfield and a pE-300 LED (CoolLED) fluorescent light source with imaging software NIS Elements AR.46.00.0. Point visiting was used to allow multiple positions to be imaged within the same time-course and cells were maintained at 37°C and 5% CO2. The images were collected using a Retiga R6 (Q-Imaging) camera. 6 randomly chosen positions per cell were captured every 10 minutes over 16h. 5 randomly chosen cells per position (meaning 30 cells tracked per condition per experiment) were individually manually tracked using the ImageJ plugin MTrackJ every 3 frames (i.e. using 30 minute timepoint intervals). The Chemotaxis and Migration Tool was used to calculate the average speed and representative images of individual cells are shown where appropriate.

Fixed cell high resolution imaging

Cells were fixed in 4% paraformaldehyde (PFA) at room temperature following ~ 4h spreading on CDM or ~ 20h spreading on polyacrylamide gradients after non-confluent (~50,000 cells/plate) seeding. Membranes were permeabilised with 0.2% (v/v) Triton-X and blocked in 5% (w/v) heat-denatured bovine serum albumin (BSA) before being stained with appropriate antibodies as in reagents section. Cells were incubated with secondary antibodies Rabbit Alexa Fluor 647-conjugated, Rabbit Alexa Fluor 594-conjugated, Rabbit Alexa Fluor 405-conjugated, Mouse Alexa Fluor 594 conjugated, Goat Alexa Fluor 594-conjugated (all Invitrogen), and/or Mouse Cy3-conjugated (Jackson ImmunoResearch) as appropriate. For detailed visualisation of actin structures, cells were stained with Phalloidin Alexa Fluor 488-conjugated (Invitrogen) or SIR-Actin (Spirochrome) as indicated, while Hoechst 33258 (ThermoFisher) was used for nucleus staining. Plates were finally mounted in Prolong Gold or Diamond antifade reagent (Life technologies). All cell lines (A2780s, H1299s, MEFs and TIFs) were fixed and stained using the same protocol.

Cells were imaged using a Leica TCS SP8 STED 3X microscope with an HC PL APO 100 x/1.40 oil objective using a HyD1 detector. A pinhole with 0.7 - 1 Airy units was used to further improve resolution while a notch filter was used for background reduction where possible. Images were captured using a white light laser (WLL) with excitation wavelengths 488, 550, 594 and 653 nm and appropriate emission spectra for green, cy3/red and far red respectively, while a Diode 405 laser was used with appropriate emission spectra for blue. For whole cells, Z-stacks were captured covering the entire Z-profile of the cell with captured at intervals of 0.3 µm at a zoom of 1x to 1.23x. Zoomed rear images were all captured separately at higher resolution (i.e. smaller pixel size) as Z-stacks covering the entire Z-profile with 0.2 µm z-step and a zoom of 4x. Images were deconvolved post capture using Huygens professional software with default settings. All subsequent analysis and quantification was performed on maximum intensity projections (MIPs) in ImageJ; all representative images shown throughout are MIPs (pseudocoloured using the red hot LUT where appropriate to reveal differences in intensity).

3D spheroid invasion assay

Spheroids of N15A/A2780 cells were grown using the hanging drop method. Cells were detached by chelation using PBS containing 3 mM EDTA and 0.6 mM DTT (N15As) or trypsin (A2780s), pelleted by centrifugation and resuspended at ~800,000 cells/ml in 1ml of 20% (v/v) Methocel (Sigma) and 80% (v/v) complete appropriate medium (see Cell culture section). 20 µl drops of cell suspension (containing ~16,000 cells each) were pipetted onto the underside of a standard 10cm tissue culture plate (Corning), inverted to form hanging drops and incubated for 24h at 37 °C in a humidified 5% (v/v)

CO2 atmosphere to allow formation of spheroids. 3-5 spheroids were extracted from the hanging drops by re-inversion and washing with complete medium using a Pasteur pipette, and resuspended in 100 µl collagen gel containing the following (all % denote v/v): 29.3% high molecular weight rat tail collagen (Corning); 0.7% 1M NaOH; 17.8% 10x PBS (Sigma); 3.6% 1mg/ml rat fibronectin (Sigma); 7.1% 1mg/ml laminin (Sigma); and 41.5% neat medium (Sigma). This collagen gel/spheroid mixture was reverse pipetted into a well of an 8-well µ-slide (Ibidi) and allowed to polymerise for 10 minutes at room temperature and a further 30 minutes at 37 °C in a humidified 5% (v/v) CO_2 atmosphere. Following polymerisation, complete medium supplemented with 30 ng/ml EGF and 25 ng/ml HGF was added to the well of the µ-slide, and incubated for 24h at 37 °C in a humidified 5% (v/v) CO2 atmosphere to allow time for cells to invade, before fixation for 15 minutes at room temperature in 4% PFA. Spheroids/cells were stained similarly as in the 'Fixed cell high resolution imaging' section above (doubling incubation times to allow for diffusion through the collagen gels).

Fixed samples were imaged by Spinning disc microscopy with a 20x/0.8 Plan-Apochromat air objective for zoomed out, edge of spheroid images with a Z-stack covering 200 µm with slices every 10 µm, while higher resolution Z-stacks of individually invading cells were imaged on the same microscope with a 63x/1.15 LD C-Apochromat Korr water objective with slices every 1 µm. All analysis was performed on the higher resolution images, MIPs shown.

Correlative Light and Electron Microscopy (serial TEM)

For performing CLEM of polarized caveolae, we used 35 mm glass bottom dish (MatTek P35G-1.0-20-C) for confocal imaging, allowing to select cells with polarized caveolin-1 (mCherry-Cav1). Low-magnification images were acquired for mapping the position of the cell in relation to the micropatterns, that are visible using transmitted light. Once imaged, cells were first fixed in Glutaraldehyde 2.5% + paraformaldehyde 2% in PHEM buffer (0.1M) for 1h on ice. A secondary fixation of 0.05% Malachite Green + 2.5% Glutaraldehyde in cacodylate buffer (0.1M) was performed (for 25 min on ice) before a post-fixation with 1%OsO4 + 0.8% KFe(CN)6 in cacodylate buffer (0.1M) (for 30 min on ice). After 3x10 min water rinses, cells were stained with 1% uranyl acetate. The cells were dehydrated in sequential gradient alcohol baths and infiltrated with Epon (resin). Pipette tips were mounted over the cell of interest following overnight polymerization at 60°C. The following day, the tips were filled with Epon and polymerized again overnight at 60°C. For relocating the region of interest, the surface of the resin block was imaged using a stereomicroscope allowing accurate positioning of the cell of interest according to the micro-pattern. Precise trimming was performed around the cell of interest. Finally, the resin block was serially sectioned (thickness : 100 nm) and all the sections were collected on electron microscope slot formvar grids (65 sections, distributed over 13 grids). Sample sections were imaged on a transmitted electron microscope (Hitachi). Transmitted electron microscopy images were stitched, aligned and stacked with TrakEM2[72]. 3D rendering of the electron microscopy acquisitions were performed with Amira aviso software.

Correlative Light and SBFSEM

Cells imaged on CDMs in gridded glass bottom plates were processed for SBFSEM using a high-density staining method involving reduced osmium, thiocarbohydrazide, osmium, uranyl acetate and lead aspartate[73]. The samples were dehydrated in staged ethanol (30, 50, 75, 90, 100, 100%) and then infiltrated with a mixture of Epon 812 (TAAB Laboratory Supplies Limited, UK) and ethanol (25% resin overnight, 50% resin for 8 hours, 75% resin overnight). The next day the 75% resin was removed carefully with blue roll and rinsed twice with warm fresh 100% resin in order to remove the ethanol. The cells were left to infiltrate in 100% resin for 5 hours. Cells were embedded in fresh resin by part curing a thin layer of resin for 4 hours, then applying a BEEM capsule with the tip removed (Agar Scientific, UK). The BEEM capsule was filled with fresh resin to form an extension to allow easier manipulation. The resin was cured at 60°C overnight. The glass coverslip was separated from the

resin by freezing for a few hours then snapping off the embedded cells leaving the imprint of the etched glass on the surface of the resin. Using the imprint of the finder grid it was possible to localise the stained cells of interest. These were crudely excised using a hacksaw and attached to 3view pins (EM Resolutions, UK). Once attached to the pin they were trimmed more carefully for examination with a Gatan 3view[74]. Note that the cell layer was never perpendicular to the cutting face, but this meant that it was possible to setup the microscope focus and imaging conditions after trimming the peak of the block. The rest of the sample was left under the surface until the correct depth had been cut. The block was coated in gold palladium in order to reduce charging in the microscope, thus in order to localise the cells of interest the pre-coated trimmed blocks were imaged using a dissecting microscope. The dimensions of the block face and relative position of the cells could then be mapped and this information transferred onto the EM block face image. Serial block face runs were collected using a Gatan 3view (Gatan Inc) within an FEI Quanta 250 FEG (Thermo Fischer Scientific) scanning electron microscope at 3.8kV using 12nm pixels and 50nm cut thickness chamber pressure 0.4 Torr.

Generation of rose plots for analysis of caveolae/actin/cell rear direction on gradient gels

Angles of Cav-1 peak, leading edge protrusion and rear location in live experiments were manually calculated using the ImageJ angle tool by creating a segment from drawing a line parallel with the idealised direction of stiffness gradient (i.e. exactly right to left in all shown soft – left to stiff – right images) to the point of interest – Cav-1/Actin protrusion peak – and then a line from this point of interest to the centre of the nucleus: i.e. a point of interest exactly left of, right of, above or below the centre point would give angles 0, 180, 90 and -90^{o} respectively. Rose plots were created in MatLab, angles were binned into twenty 18^{o} segments; relative sizes of triangular segments are directly proportional to the number of cells with angles contained within each bin.

Quantification of Cav-1/Cavin-1, Ect2 and Actin structures in fixed cells and membrane, Ezrin-WT and Ezrin-CA in live cells

For quantification of localised Cavin-1 intensity, whole cell images were analysed with the interactive 3-D surface plot v2.31 in ImageJ using a 128 grid size and smoothing factor of 3.0. Under these conditions, the peak intensities of the rear and non-rear or rear and nuclear cell regions were manually identified and the ratio rear peak / non-rear peak or rear peak / nuclear peak calculated, therefore providing inherent normalisation avoiding staining/expression discrepancies. For quantification of actin structures, a similar 3-D surface plot approach was used to manually identify the rear peak and leading edge peak of phalloidin 488 staining intensity to produce the normalised rear / leading edge ratio. For the quantification of localised GFP-membrane, GFP-Ezrin-WT and GFP-CA in live fluorescent cells, the interactive 3-D surface plot approach was similarly used on the first time-frame to measure the rear and front peaks of cells. These values were then normalised by dividing by the average of the rear and front peak intensities, such that when linked, pairwise front and rear values are plotted, all lines pass through the normalised peak intensity value 1.0. For Ect2, the normalised value for nuclear staining was additionally measured and normalised linked data of rear, nucleus and front shown. For line profiles of Cavin-1 intensity, the line profile tool was used in ImageJ: representative lines of length 14.8021 µm were used from the rearmost point of the cell through towards the cell middle in zoomed images. Absolute Cavin-1 intensity was then quantified every 0.0507 µm (pixel width), smoothed by averaging with the neighbouring 5 pixel values and the average of all cells plotted with SEM. Cavin-1 peak intensity position was determined by identifying the distance from the rearmost cell point of the single, non-smoothed pixel with the highest Cavin-1 value.

Quantification of localised adhesion numbers

A2780 cells transiently transfected with EGFP-Paxillin and mCherry-Caveolin-1 were imaged for 5 minutes (1 minute per frame) with 9 Z-slices with a step size of 1 µm. Adhesions were manually identified by observing high intensity paxillin regions which persist > 2 frames within individual Z-slices, and all such adhesions were counted across all Z-slices (where it was assumed that the step-

size was large enough to avoid duplicate countings). Adhesions behind the rearmost boundary of the nucleus were assigned as 'behind', while all other adhesions in advance of this boundary were counted as 'in front' relative to nucleus position.

Reversible hypo-osmotic shock protocol and quantification of Cav-1 localisation and accumulation

For live imaging experiments using the reversible hypo-osmotic shock, cells expressing Emerald lifeact + mCherry-Caveolin-1 were imaged in isotonic control medium (1x Opti-Klear with 10% (v/v) FCS) as outlined in the section above for 10 minutes using point visiting, capturing at 1 minute intervals. The medium was then rapidly (~4 minutes) replaced using an aspirator and 1ml pipette with 50% 1x Opti-Klear + 50% distilled water and all cells were subsequently imaged for 10 minutes in osmotic shock conditions. The osmotic medium was then rapidly (~4 minutes) replaced with isotonic 100% 1x Opti-Klear using an aspirator and pipette and imaged for a further 20 minutes. As a result, the same cells were imaged and analysed in isotonic conditions pre-shock, osmotic shock conditions, and isotonic conditions post-shock.

For quantification of Cav-1 intensity during the reversible hypo-osmotic shock assay, the intensity of mCherry-Caveolin-1 expression was measured in manually drawn regions at the rear and in the centre of imaged cells using ImageJ software. The same drawn ROIs were moved according to cell translocation so that the intensities were determined for the 11 timepoints pre-shock, the 11 timepoints under shock conditions and the 11 timepoints post-shock. All measured intensities were background subtracted and normalised to the intensity at the first timepoint t = 0, such that normalised timecourse profiles for the rear and central regions of all cells for the full > 30 minutes of the assay were generated. Each timepoint was then averaged across all cells analysed and the average timecouse profiles for all rear and all central regions was plotted with SEM bars shown.

For live analysis of Cav-1 accumulation at the rear of cells, osmotic shock was used to induce cells into a state with initially low rear Cav-1 (by incubation in osmotic medium for ~10 minutes) before the medium was replaced with isotonic medium via rapid aspirator pump and immediate pipetting. Throughout this process, laser-based (point visiting) Definite Focus was used via Slidebook software such that cells were captured 30-60s post media change without need for manual refocusing. Cells were imaged for a further >10 minutes using Definite Focus. For quantification, the segmentation tool used for FRET analysis (above) was adapted to create a binary mask using the mCherry-Cav-1 staining. The mean average intensity of the mCherry-Cav-1 intensity within the rear 10% and remaining 90% within the binary mask corresponding to the whole cell was then automatically measured for the pre and all post media change timepoints, and normalised upon division by the maximum value (such that all other values < 1). The average time-course lines for the normalised average Cav-1 intensity were plotted for the rear and rest of cell regions, with quadratic curves fitted in GraphPad Prism to indicate a smooth, quadratic accumulation of Cav-1 at the cell rear.

Hypo-osmotic shock for fixed cells and FRET analysis

Cells expressing Raichu-RhoA were imaged in control medium as outlined in the section above for 5 minutes. The medium was then rapidly replaced with 50% Ham F12 + 50% distilled water and cells were subsequently imaged between 10 – 30 minutes post osmotic shock. Quantification of cell rear movement and FRET ratiometric activity were performed as before. For fixed cell imaging experiments using hypo-osmotic shock, cells were seeded on CDMs and left to spread for ~4h. The medium was then replaced with either normal growth medium for the control case or 50% medium + 50% distilled water for the hypo-osmotic shock and incubated for 10 minute before being fixed, stained and imaged as above.

Live Y27632 and H1152 treatment

For experiments using live Y27632 treatment, cells expressing mCherry-Caveolin-1 were captured in the control state across a period of 5 minutes, treated with Y27632 via direct addition to the medium, rapidly refocused within ~ 5 minutes and the same cells imaged for a further 1h, capturing every 30s.

Cells were also left for 1h without treatment to affirm that rear Cav-1 loss was not as an artefact of longer term imaging. For quantification, the rear / non-rear ratio of Cav-1 intensity was calculated using the 3-D surface plot in ImageJ (see Quantification of Cav-1/Cavin-1, Ect2 and Actin structures in fixed cells and membrane, Ezrin-WT and Ezrin-CA in live cells section above) for the first time point before Y27632 treatment and for a randomly chosen time point between 30 and 60 minutes post treatment, averaged across all captured cells and compared.

For live H1152 treatment, cells expressing Emerald-Lifeact and either control or Cav-1 siRNA-A were imaged for 5 minutes, treated with H1152 via direct addition to the medium, then imaged for a further 5 minutes. Throughout, Definite Focus was used to avoid any manual refocusing time, such that frames were taken every 30s before, (during) and after drug treatment. The forward translocation of the rear was manually measured for both transfection conditions without (before) and with (after) H1152 treatment, where negative values correspond to backwards movement.

Global and caged Cytochalasin-D treatment

For global Cytochalasin-D treatment, cells expressing GFP-lifeact + mCherry-Caveolin-1 were treated with cytochalasin-D at 2 µM and imaged 10 minutes following treatment with typical capture conditions. Photo-activatable 'caged' Cytochalasin-D was produced in the del Campo lab (manuscript in submission) and used as follows: Cells expressing GFP-lifeact + mCherry-Caveolin-1 were first treated with 50 µM immediately prior to capture. A 5 x 5 µm ROI was drawn using Slidebook 6.0, positioned such that the ROI was completely outside the cell area (as determined by lifeact expression) but within ~ 10 µm the rear of the cell (and such that the rear was the closest part of the cell to the ROI). After 2 fluorescent frame captures using the 488 nm and 561 nm lasers (to ascertain the GFP-lifeact and mCherry-Caveolin-1 expression pre photo-manipulation) the 405 nm emission photo-manipulation laser was used to illuminate each pixel in the previously drawn ROI for 10ms each (meaning the whole region was photo-activated for a total of ~6.5s since there are 5.12 pixels per micron). Cells were then imaged for a further 10 minutes with normal fluorescent conditions (as it was deemed that with captures longer than 10 minutes the activated Cytochalasin-D may diffuse to other areas of the cell). For the control comparison, cells were subjected to exactly the same photo-manipulation protocol in the absence of any drug treatment.

For quantification, the average mCherry-Caveolin-1 intensity within a manually drawn region at the rear of the cell pre-photo-manipulation (called rear pre), a region at the rear of the cell 10 minutes post-photo-manipulation (rear post), a region at the centre of the cell pre-photo-manipulation (centre pre), and a region at the centre of the cell 10 minutes post-photo-manipulation (centre post) were all measured using ImageJ and background subtracted. The ratio ((rear pre)/(rear post))/(centre pre)/(centre post)) was then calculated and used as a single metric to describe rear Cav-1 loss upon caged Cytochalasin-D treatment, where the treated cells were compared to untreated (but photo-manipulated) cells.

Statistical analysis of experimental results

Box and whisker plots show mean as '+', whiskers generated using Tukey method. All statistics shown on box and whisker graphs with two conditions describe unpaired student T tests while for all box and whisker graphs with > two conditions a one-way ANOVA test for multiple comparisons has been used. For all linked line graphs concerning trap force data, pairwise Mann-Whitney tests were used to compare the front and rear membrane of the same cells directly, while data from all other linked line graphs have been subjected to paired T tests. All statistical analysis has been performed with GraphPad Prism software, where **** denotes $p < 0.0001$, *** denotes $p < 0.001$, ** denotes $p < 0.01$ and * denotes $p < 0.05$.

Model construction

Our model of rear retraction incorporates 19 variables of which 12 are individual proteins (shown in green, yellow or cyan), 6 are empirical entities pertaining to stiffness, tension, polarisation, actin

alignment and retraction itself (in orange, pink or red) and the caveolae complex simplified to a single node. While all variables coloured orange, yellow, pink or red - and reactions there-between - are included based on findings/hypotheses confirmed or originated in this paper, variables coloured green or cyan are included to augment our study based on literature evidence. Green nodes link caveolae to RhoA activity while cyan nodes are intermediaries between ROCK1/PKN-2 activation and actin alignment/MLC phosphorylation. We included Src, the GTPase activating protein (GAP) p190RhoGAP and Ect2 as the RhoA guanidine nucleotide exchange factor (GEF) as 'green nodes' with activation/inhibition reactions as shown since: (i) Cav1 can interact with RhoA [75] but shows no structural evidence of being a GEF [76] so naturally must act via a GEF for GTP hydrolysis of the small GTPase; (ii) Cav1 can interact with the RhoA activator/GEF Ect2 and control the localisation and activity of a RhoA inactivator/GAP p190RhoGAP to regulate RhoA activity [77]; and (iii) Src can phosphorylate Cav1 on Y14 to influence Cav1 expression and promote caveolae formation [77], or oligomerisation and release [78]. Src also controls p190RhoGAP activity which directly inhibits RhoA [79], and pY14-Cav1 binds to and activates Csk, a ubiquitously expressed inhibitor of Src [79]. DRF (Diaphanous-related formin), Limk, Cofilin, CPI-17 and MLCP (Myosin-light-chain phosphatase) and activation/inhibition reactions there-between were included as 'cyan nodes' based on the strong evidence that: (i) Formins are always required to some extent for efficient F-actin polymerisation and can be activated directly by RhoA or Rock1 [80]; (ii) ROCK activates LIM-kinase 1 by phosphorylation at threonine 508 within the activation loop [81]; (iii) Limk phosphorylates cofilin at Ser 3 both *in vitro* and *in vivo* which abolishes the ability of cofilin to bind and depolymerize actin [82]; (iv) Cofilin universally disassembles actin filaments so acts as an inhibitor to rear actin alignment [83]; (v) Phosphorylation of CPI-17 at Thr(38) by Pkn-2 or ROCK1 enhances the inhibitory potency of CPI-17 towards MLCP [84]; and (vi) the primary function of MLCP is to oppose myosin phosphorylation whereby kinase and phosphatase activities are mutually antagonistic and in competition [85].

ODEs formulation

The ordinary differential equations (ODE) model was built with the following specifications:

(i) All reactions use mass-action kinetics; this is the simplest kinetic scheme to use and in the absence of either more detailed numerical data or suggestions of other more relevant dynamics at play in vitro, is the most sensible starting point for a kinetic model.

(ii) All variables, both proteins and biophysical entities, can be in an active, inactive or bound state with a conserved moiety; proteins can certainly be active, inactive or bound in cells. The biophysical entities are assigned an 'active' or 'high' state, and an 'inactive' or 'low' state to be consistent with the protein variables within the same model as convention, although the 'inactive' or 'low' states can be regarded as dummy variables, while the 'high' states are the actual outputs of interest. For example the 'high rear retraction' corresponds to the instantaneous velocity of the rear, while the 'high polarised substrate stiffness' input corresponds to the steepness of theoretical gradient of the substrate. This also ensures all variables remain finite, see below.

(iii) The value of all variables is normalised and confined between 0 and 100 units for all time; This ensures that the value of all variables in the model remain finite (i.e. that a cell cannot express an infinite amount of protein or that rear retraction cannot be infinitely fast which would be biologically implausible). This normalisation is such that protein and biophysical entity levels can be comparable and conceptualised on the same scale, while also conveniently overcomes the lack or real experimental expression level data.

(iv) Reactions involving two proteins are two step processes whereby the proteins first bind together then the activation state of one/both proteins change/s as desired; evidence suggests for many protein-protein interactions that activation or inhibition requires binding of the proteins before a state change, for example The GEF Ect2 binds to GDP bound RhoA before promoting the switch to the GTP active form of RhoA.

(v) Reactions involving at least one biophysical entity are one step processes whereby the activation state of at least one variable involved in the reaction changes directly as desired; it makes no sense to conceptualise that polarised contractility binds to high membrane tension for example, therefore one step state changes are sufficient for the required kinetics.

(vi) All reactions which only involve proteins or only involve biophysical variables are reversible where the backwards direction is at most 10% the rate of the forward direction, decreased tension activating caveolae and aligned Actin and p-MLC activating Acto-myosin contractility are non-reversible; Reversibility of protein-protein interactions are well reported, keeping most reactions as reversible to a small extent prevents an implausible high resting state, while a biophysical entity relapsing to a protein or vice versa is conceptually impossible.

(vii) All proteins and biophysical entities are subject to a turnover term, whereby there is a constant flux from the active state to the inactive state for all variables when not explicitly activated upstream. Without turnover and/or reversibility, variables such as rear retraction stay in an active, high level steady state despite lack of active upstream activators which is physiologically unrealistic: rear retraction requires Acto-myosin contractility and aligned Actin constantly and this formulation ensures this.

Note since the potent inhibitor of p-MLC, MLCP is already included explicitly in the model, and these are almost like two forms of the same protein, the turnover of p-MLC is not included. To balance this and since p-MLC is not a protein but a specific state thereof, the activation of p-MLC is one-step rather than two step binding then activation. Implementing p-MLC with binding and turnover does not alter general findings of the model provided rates are balanced accordingly.

Initial conditions

For unperturbed simulations, the initial conditions (ICs) used are the input 'polarised substrate stiffness' set to the maximum 100, active Src set to 50, active Cofilin and MLCP set to 100, while the active form of all other is set to 0. The polarised substrate stiffness IC was taken as it is the nominated external input of the model, required to initiate the proceeding dynamics downstream. Cofilin and MLCP were set to 100 since these are inhibitory variables with no explicit activators, such that the only way these can be active is when they start active, while Src is set at 50% active initially since it has no upstream activator but has both an activator and inhibitory role on downstream effectors.

Parameter values

All parameter values were based on order of magnitude predictions, i.e. were subject to the constraint that all values were 1×10^{-n} for an integer n greater or equal to 1. The order of magnitude approach was adopted since the appropriate kinetic data was unavailable, and more specific rates would not be justifiable and may promote an over-determined model. All rates were checked with half and double values, and the general topology and behaviour was unchanged. Parameters were initially set based on literature findings and certain assumptions and then iteratively, improved based on biological plausibility of simulated outputs. In particular, it was assumed that protein-protein interactions occur with higher rates than those involving biophysical entities because: (i) protein-protein interactions are two step (binding then state change) so are already going to be slower overall, and (ii) it is known that protein-protein interactions such as binding can be incredibly quick *in vitro*, while the precise kinetics of polarised contractility leading to decreased tension for example are likely to be slower as these events are more complex at the molecular level. All parameter rates used can be seen in the full list of ODEs used in the model below.

Model simulation and perturbation

The model was built and simulated using Copasi software version 4.15 [86]. Deterministic simulations were performed using the LSODA method for the first 10000 seconds with an interval size of 25s. The time-course outputs for all variables in the model were checked for plausibility, however the outputs

for a chosen subset of variables are shown for simplicity. For *a priori* knockdown simulations, all variables were kept the same as the unperturbed simulation apart from the initial amount of the relevant variable (RhoA, and Cav-1), which were both reduced to 12% of total concentration. For substrate transition simulations, 'polarised substrate stiffness' was assigned to change from 100 to 0 or 0 to 100 at t = 4000s. For simulation of the osmotic shock assay, the rate of transition from decreased membrane tension to increase membrane tension was increased 1000-fold (from 0.01 to 10) at time t = 4000s, and then returned to the original value (0.01) at t = 7000s to mimic return to isotonic conditions. For mimicry of Y-27632 treatment, an event at t = 5000s was added to the simulation where the turnover rate for Rock1 and Pkn-2 was increased 1000-fold (from 0.01 to 10); for 'global' cytochalasin-D treatment, the turnover rate of F-actin (i.e. the rate at which F-actin transitions to G-actin) was increased 100-fold (from 0.01 to 1) while for 'caged' cytocholasin-D treatment the turnover rate of F-actin was increase 20-fold (from 0.01 to 0.2), both events occurring at t = 5000s.

Parameter sensitivity analysis

Parameter sensitivity analysis was performed using the built-in Copasi tool with Retraction/Recoil as the target and all rates in the model as the analysed objects. Scaled parameter analysis was run, such that the concurrent rates used in the model were factored in to the apparent importance of each parameter, while the total of the scaled parameter sensitivity sums to zero.

ODE equations

The full list of ODE equations used in the model, including all rate values, are included in the following pages (where GEF denotes Ect2).

Code will be made available upon acceptance in the Biomodels database (https://www.ebi.ac.uk/biomodels-main/).

$$\frac{d([RhoAgdp]\cdot V_{rear})}{dt} = +V_{rear}\cdot((0.1\cdot[RhoA:Rock1]-0.01\cdot[Rock1a]\cdot[RhoAgdp]))$$
$$-V_{rear}\cdot((0.1\cdot[Gefa]\cdot[RhoAgdp]-0.01\cdot[\text{"Rho-Gef"}]))$$
$$+V_{rear}\cdot(0.01\cdot[RhoAgtp])$$
$$+V_{rear}\cdot((0.1\cdot[RhoA:PKN2]-0.01\cdot[PKN2a]\cdot[RhoAgdp]))$$
$$+V_{rear}\cdot((0.1\cdot[RhoA:Drf]-0.01\cdot[DRFa]\cdot[RhoAgdp]))$$
$$+V_{rear}\cdot((0.1\cdot[p190GAP:RhoA]-0.01\cdot[p190GAPi]\cdot[RhoAgdp]))$$

$$\frac{d([RhoAgtp]\cdot V_{rear})}{dt} = -V_{rear}\cdot((0.001\cdot[RhoAgtp]\cdot[Rock1i]-0.0001\cdot[RhoA:Rock1]))$$
$$-V_{rear}\cdot((0.001\cdot[RhoAgtp]\cdot[DRFi]-0.0001\cdot[RhoA:Drf]))$$
$$-V_{rear}\cdot((0.001\cdot[RhoAgtp]\cdot[PKN2i]-0.0001\cdot[RhoA:PKN2]))$$
$$-V_{rear}\cdot(0.01\cdot[RhoAgtp])$$
$$-V_{rear}\cdot((0.001\cdot[p190GAPa]\cdot[RhoAgtp]-0.0001\cdot[p190GAP:RhoA]))$$
$$+V_{rear}\cdot((0.1\cdot[\text{"Rho-Gef"}]-0.01\cdot[RhoAgtp]\cdot[Gefi]))$$

$$\frac{d([Rock1i]\cdot V_{rear})}{dt} = -V_{rear}\cdot((0.001\cdot[RhoAgtp]\cdot[Rock1i]-0.0001\cdot[RhoA:Rock1]))$$
$$+V_{rear}\cdot((0.01\cdot[ROCK1:CPI17]-0.001\cdot[Rock1i]\cdot[\text{"CPI-17a"}]))$$
$$+V_{rear}\cdot((0.01\cdot[ROCK1:DRF]-0.001\cdot[Rock1i]\cdot[DRFa]))$$
$$+V_{rear}\cdot((0.001\cdot[Rock1a]\cdot[pMLCi]-0.0001\cdot[Rock1i]\cdot[pMLCa]))$$
$$+V_{rear}\cdot(0.01\cdot[Rock1a])$$
$$+V_{rear}\cdot((0.01\cdot[\text{"ROCK1-LIMK"}]-0.001\cdot[LIMKa]\cdot[Rock1i]))$$

$$\frac{d([Rock1a]\cdot V_{rear})}{dt} = +V_{rear}\cdot((0.1\cdot[RhoA:Rock1]-0.01\cdot[Rock1a]\cdot[RhoAgdp]))$$
$$-V_{rear}\cdot((0.0001\cdot[Rock1a]\cdot[\text{"CPI-17i"}]-1e\text{-}005\cdot[ROCK1:CPI17]))$$
$$-V_{rear}\cdot((0.01\cdot[Rock1a]\cdot[DRFi]-0.001\cdot[ROCK1:DRF]))$$
$$-V_{rear}\cdot((0.001\cdot[Rock1a]\cdot[pMLCi]-0.0001\cdot[Rock1i]\cdot[pMLCa]))$$
$$-V_{rear}\cdot(0.01\cdot[Rock1a])$$
$$-V_{rear}\cdot((0.001\cdot[Rock1a]\cdot[LIMKi]-0.0001\cdot[\text{"ROCK1-LIMK"}]))$$

$$\frac{d([RhoA:Rock1]\cdot V_{rear})}{dt} = +V_{rear}\cdot((0.001\cdot[RhoAgtp]\cdot[Rock1i]-0.0001\cdot[RhoA:Rock1]))$$
$$-V_{rear}\cdot((0.1\cdot[RhoA:Rock1]-0.01\cdot[Rock1a]\cdot[RhoAgdp]))$$

$$\frac{d([DRFi]\cdot V_{rear})}{dt} = +V_{rear}\cdot((0.1\cdot[DRF:Actin]-0.01\cdot[DRFi]\cdot[Actinf]))$$
$$-V_{rear}\cdot((0.001\cdot[RhoAgtp]\cdot[DRFi]-0.0001\cdot[RhoA:Drf]))$$
$$-V_{rear}\cdot((0.01\cdot[Rock1a]\cdot[DRFi]-0.001\cdot[ROCK1:DRF]))$$
$$+V_{rear}\cdot(0.01\cdot[DRFa])$$

$$\frac{d([DRFa]\cdot V_{rear})}{dt} = -V_{rear}\cdot((0.1\cdot[DRFa]\cdot[Actinag]-0.0001\cdot[DRF:Actin]))$$
$$+V_{rear}\cdot((0.01\cdot[ROCK1:DRF]-0.001\cdot[Rock1i]\cdot[DRFa]))$$
$$-V_{rear}\cdot(0.01\cdot[DRFa])$$
$$+V_{rear}\cdot((0.1\cdot[RhoA:Drf]-0.01\cdot[DRFa]\cdot[RhoAgdp]))$$

$$\frac{d([PKN2i]\cdot V_{rear})}{dt} = +V_{rear}\cdot((0.01\cdot[PKN2:CPI17]-0.001\cdot[\text{"CPI-17a"}]\cdot[PKN2i]))$$
$$-V_{rear}\cdot((0.001\cdot[RhoAgtp]\cdot[PKN2i]-0.0001\cdot[RhoA:PKN2]))$$
$$+V_{rear}\cdot(0.01\cdot[PKN2a])$$
$$+V_{rear}\cdot((0.001\cdot[\text{"Pkn2-Actin"}]-0.0001\cdot[PKN2i]\cdot[Actinf]))$$

$$\frac{d([RhoA:PKN2]\cdot V_{rear})}{dt} = +V_{rear}\cdot((0.001\cdot[RhoAgtp]\cdot[PKN2i]-0.0001\cdot[RhoA:PKN2]))$$
$$-V_{rear}\cdot((0.1\cdot[RhoA:PKN2]-0.01\cdot[PKN2a]\cdot[RhoAgdp]))$$

$$\frac{d([PKN2a]\cdot V_{rear})}{dt} = -V_{rear}\cdot((0.01\cdot[PKN2a]\cdot["CPI\text{-}17i"]-0.001\cdot[PKN2:CPI17]))$$
$$-V_{rear}\cdot(0.01\cdot[PKN2a])$$
$$+V_{rear}\cdot((0.1\cdot[RhoA:PKN2]-0.01\cdot[PKN2a]\cdot[RhoAgdp]))$$
$$-V_{rear}\cdot((0.001\cdot[PKN2a]\cdot[Actinag]-0.0001\cdot["Pkn2\text{-}Actin"]))$$

$$\frac{d([LIMKi]\cdot V_{rear})}{dt} = +V_{rear}\cdot(0.01\cdot[LIMKa])$$
$$-V_{rear}\cdot((0.001\cdot[Rock1a]\cdot[LIMKi]-0.0001\cdot["ROCK1\text{-}LIMK"]))$$
$$+V_{rear}\cdot((0.01\cdot["LIMK\text{-}Cofilin"]-0.001\cdot[LIMKi]\cdot[Cofilini]))$$

$$\frac{d(["ROCK1\text{-}LIMK"]\cdot V_{rear})}{dt} = +V_{rear}\cdot((0.001\cdot[Rock1a]\cdot[LIMKi]-0.0001\cdot["ROCK1\text{-}LIMK"]))$$
$$-V_{rear}\cdot((0.01\cdot["ROCK1\text{-}LIMK"]-0.001\cdot[LIMKa]\cdot[Rock1i]))$$

$$\frac{d([LIMKa]\cdot V_{rear})}{dt} = -V_{rear}\cdot(0.01\cdot[LIMKa])$$
$$+V_{rear}\cdot((0.01\cdot["ROCK1\text{-}LIMK"]-0.001\cdot[LIMKa]\cdot[Rock1i]))$$
$$-V_{rear}\cdot((0.01\cdot[LIMKa]\cdot[Cofilina]-0.001\cdot["LIMK\text{-}Cofilin"]))$$

$$\frac{d([Cofilina]\cdot V_{rear})}{dt} = -V_{rear}\cdot((0.0001\cdot[Cofilina]\cdot[Actinf]-1e\text{-}005\cdot[Cofilin:Actin]))$$
$$+V_{rear}\cdot((0.01\cdot[Cofilin:Actin]-0.001\cdot[Actinag]\cdot[Cofilina]))$$
$$-V_{rear}\cdot((0.01\cdot[LIMKa]\cdot[Cofilina]-0.001\cdot["LIMK\text{-}Cofilin"]))$$

$$\frac{d(["LIMK\text{-}Cofilin"]\cdot V_{rear})}{dt} = +V_{rear}\cdot((0.01\cdot[LIMKa]\cdot[Cofilina]-0.001\cdot["LIMK\text{-}Cofilin"]))$$
$$-V_{rear}\cdot((0.01\cdot["LIMK\text{-}Cofilin"]-0.001\cdot[LIMKi]\cdot[Cofilini]))$$

$$\frac{d([Cofilini]\cdot V_{rear})}{dt} = +V_{rear}\cdot((0.01\cdot["LIMK\text{-}Cofilin"]-0.001\cdot[LIMKi]\cdot[Cofilini]))$$

$$\frac{d([Actinag]\cdot V_{rear})}{dt} = -V_{rear}\cdot((0.1\cdot[DRFa]\cdot[Actinag]-0.0001\cdot[DRF:Actin]))$$
$$+V_{rear}\cdot((0.01\cdot[Cofilin:Actin]-0.001\cdot[Actinag]\cdot[Cofilina]))$$
$$+V_{rear}\cdot(0.01\cdot[Actinf])$$
$$-V_{rear}\cdot((0.001\cdot[PKN2a]\cdot[Actinag]-0.0001\cdot["Pkn2\text{-}Actin"]))$$

$$\frac{d([DRF:Actin]\cdot V_{rear})}{dt} = +V_{rear}\cdot((0.1\cdot[DRFa]\cdot[Actinag]-0.0001\cdot[DRF:Actin]))$$
$$-V_{rear}\cdot((0.1\cdot[DRF:Actin]-0.01\cdot[DRFi]\cdot[Actinf]))$$

$$\frac{d([Actinf]\cdot V_{rear})}{dt} = +V_{rear}\cdot((0.1\cdot[DRF:Actin]-0.01\cdot[DRFi]\cdot[Actinf]))$$
$$-V_{rear}\cdot((0.0001\cdot[Cofilina]\cdot[Actinf]-1e\text{-}005\cdot[Cofilin:Actin]))$$
$$-V_{rear}\cdot(0.01\cdot[Actinf])$$
$$+V_{rear}\cdot((0.001\cdot["Pkn2\text{-}Actin"]-0.0001\cdot[PKN2i]\cdot[Actinf]))$$

$$\frac{d([Cofilin:Actin]\cdot V_{rear})}{dt} = +V_{rear}\cdot((0.0001\cdot[Cofilina]\cdot[Actinf]-1e\text{-}005\cdot[Cofilin:Actin]))$$
$$-V_{rear}\cdot((0.01\cdot[Cofilin:Actin]-0.001\cdot[Actinag]\cdot[Cofilina]))$$

$$\frac{d(["CPI\text{-}17i"]\cdot V_{rear})}{dt} = -V_{rear}\cdot((0.01\cdot[PKN2a]\cdot["CPI\text{-}17i"]-0.001\cdot[PKN2:CPI17]))$$
$$-V_{rear}\cdot((0.0001\cdot[Rock1a]\cdot["CPI\text{-}17i"]-1e\text{-}005\cdot[ROCK1:CPI17]))$$
$$+V_{rear}\cdot((0.001\cdot[CPI17:MLCP]-0.0001\cdot["CPI\text{-}17i"]\cdot[MLCPi]))$$

$$\frac{d([PKN2:CPI17]\cdot V_{rear})}{dt} = +V_{rear}\cdot((0.01\cdot[PKN2a]\cdot["CPI\text{-}17i"]-0.001\cdot[PKN2:CPI17]))$$
$$-V_{rear}\cdot((0.01\cdot[PKN2:CPI17]-0.001\cdot["CPI\text{-}17a"]\cdot[PKN2i]))$$

$$\frac{d(["CPI\text{-}17a"]\cdot V_{rear})}{dt} = +V_{rear}\cdot((0.01\cdot[PKN2:CPI17]-0.001\cdot["CPI\text{-}17a"]\cdot[PKN2i]))$$
$$+V_{rear}\cdot((0.01\cdot[ROCK1:CPI17]-0.001\cdot[Rock1i]\cdot["CPI\text{-}17a"]))$$
$$-V_{rear}\cdot((0.01\cdot["CPI\text{-}17a"]\cdot[MLCPa]-0.001\cdot[CPI17:MLCP]))$$

$$\frac{d([ROCK1:CPI17]\cdot V_{rear})}{dt} = +V_{rear}\cdot((0.0001\cdot[Rock1a]\cdot["CPI\text{-}17i"]-1e\text{-}005\cdot[ROCK1:CPI17]))$$
$$-V_{rear}\cdot((0.01\cdot[ROCK1:CPI17]-0.001\cdot[Rock1i]\cdot["CPI\text{-}17a"]))$$

$$\frac{d([MLCPa]\cdot V_{rear})}{dt} = -V_{rear}\cdot((0.01\cdot["CPI\text{-}17a"]\cdot[MLCPa]-0.001\cdot[CPI17{:}MLCP])) -V_{rear}\cdot((0.01\cdot[MLCPa]\cdot[pMLCa]-0.001\cdot["MLCP\text{-}PMLC"])) +V_{rear}\cdot((0.01\cdot["MLCP\text{-}PMLC"]-0.001\cdot[MLCPa]\cdot[pMLCi]))$$

$$\frac{d([MLCPi]\cdot V_{rear})}{dt} = +V_{rear}\cdot((0.001\cdot[CPI17{:}MLCP]-0.0001\cdot["CPI\text{-}17i"]\cdot[MLCPi]))$$

$$\frac{d([CPI17{:}MLCP]\cdot V_{rear})}{dt} = +V_{rear}\cdot((0.01\cdot["CPI\text{-}17a"]\cdot[MLCPa]-0.001\cdot[CPI17{:}MLCP])) -V_{rear}\cdot((0.001\cdot[CPI17{:}MLCP]-0.0001\cdot["CPI\text{-}17i"]\cdot[MLCPi]))$$

$$\frac{d([RhoA{:}Drf]\cdot V_{rear})}{dt} = +V_{rear}\cdot((0.001\cdot[RhoAgtp]\cdot[DRFi]-0.0001\cdot[RhoA{:}Drf])) -V_{rear}\cdot((0.1\cdot[RhoA{:}Drf]-0.01\cdot[DRFa]\cdot[RhoAgdp]))$$

$$\frac{d([ROCK1{:}DRF]\cdot V_{rear})}{dt} = +V_{rear}\cdot((0.01\cdot[Rock1a]\cdot[DRFi]-0.001\cdot[ROCK1{:}DRF])) -V_{rear}\cdot((0.01\cdot[ROCK1{:}DRF]-0.001\cdot[Rock1i]\cdot[DRFa]))$$

$$\frac{d([pMLCa]\cdot V_{rear})}{dt} = +V_{rear}\cdot((0.001\cdot[Rock1a]\cdot[pMLCi]-0.0001\cdot[Rock1i]\cdot[pMLCa])) -V_{rear}\cdot((0.01\cdot[MLCPa]\cdot[pMLCa]-0.001\cdot["MLCP\text{-}PMLC"]))$$

$$\frac{d([pMLCi]\cdot V_{rear})}{dt} = -V_{rear}\cdot((0.001\cdot[Rock1a]\cdot[pMLCi]-0.0001\cdot[Rock1i]\cdot[pMLCa])) +V_{rear}\cdot((0.01\cdot["MLCP\text{-}PMLC"]-0.001\cdot[MLCPa]\cdot[pMLCi]))$$

$$\frac{d(["MLCP\text{-}PMLC"]\cdot V_{rear})}{dt} = +V_{rear}\cdot((0.01\cdot[MLCPa]\cdot[pMLCa]-0.001\cdot["MLCP\text{-}PMLC"])) -V_{rear}\cdot((0.01\cdot["MLCP\text{-}PMLC"]-0.001\cdot[MLCPa]\cdot[pMLCi]))$$

$$\frac{d(["Cavi\text{-}Src"]\cdot V_{rear})}{dt} = -V_{rear}\cdot((1e\text{-}006\cdot["Cavi\text{-}Src"]-1e\text{-}007\cdot[Cav1a]\cdot[Srca])) +V_{rear}\cdot((1e\text{-}006\cdot[Cav1i]\cdot[Srca]-1e\text{-}007\cdot["Cavi\text{-}Src"]))$$

$$\frac{d([Cav1a]\cdot V_{rear})}{dt} = -V_{rear}\cdot((1e\text{-}006\cdot[Cav1a]\cdot[Srca]-1e\text{-}007\cdot["Cava\text{-}Src"])) -V_{rear}\cdot((0.01\cdot[Cav1a]\cdot[Gefi]-0.001\cdot["Cav\text{-}Gef"])) +V_{rear}\cdot(0.01\cdot[Tension.D]\cdot[Cav1i]) -V_{rear}\cdot(0.01\cdot[Cav1a]) +V_{rear}\cdot((1e\text{-}006\cdot["Cavi\text{-}Src"]-1e\text{-}007\cdot[Cav1a]\cdot[Srca]))$$

$$\frac{d([Srca]\cdot V_{rear})}{dt} = -V_{rear}\cdot((1e\text{-}006\cdot[Cav1a]\cdot[Srca]-1e\text{-}007\cdot["Cava\text{-}Src"])) -V_{rear}\cdot((0.01\cdot[Srca]\cdot[p190GAPi]-0.001\cdot["Src\text{-}p190"])) +V_{rear}\cdot((1e\text{-}006\cdot["Cavi\text{-}Src"]-1e\text{-}007\cdot[Cav1a]\cdot[Srca])) -V_{rear}\cdot((1e\text{-}006\cdot[Cav1i]\cdot[Srca]-1e\text{-}007\cdot["Cavi\text{-}Src"]))$$

$$\frac{d([Cav1i]\cdot V_{rear})}{dt} = +V_{rear}\cdot((1e\text{-}006\cdot["Cava\text{-}Src"]-1e\text{-}007\cdot[Cav1i]\cdot[Srci])) +V_{rear}\cdot((0.1\cdot["Cav\text{-}Gef"]-0.01\cdot[Cav1i]\cdot[Gefa])) -V_{rear}\cdot(0.01\cdot[Tension.D]\cdot[Cav1i]) +V_{rear}\cdot(0.01\cdot[Cav1a]) -V_{rear}\cdot((1e\text{-}006\cdot[Cav1i]\cdot[Srca]-1e\text{-}007\cdot["Cavi\text{-}Src"]))$$

$$\frac{d([Srci]\cdot V_{rear})}{dt} = +V_{rear}\cdot((1e\text{-}006\cdot["Cava\text{-}Src"]-1e\text{-}007\cdot[Cav1i]\cdot[Srci])) +V_{rear}\cdot((0.01\cdot["Src\text{-}p190"]-0.001\cdot[Srci]\cdot[p190GAPa]))$$

$$\frac{d(["Cav\text{-}Gef"]\cdot V_{rear})}{dt} = +V_{rear}\cdot((0.01\cdot[Cav1a]\cdot[Gefi]-0.001\cdot["Cav\text{-}Gef"])) -V_{rear}\cdot((0.1\cdot["Cav\text{-}Gef"]-0.01\cdot[Cav1i]\cdot[Gefa]))$$

$$\frac{d([Gefi]\cdot V_{rear})}{dt} = -V_{rear}\cdot((0.01\cdot[Cav1a]\cdot[Gefi]-0.001\cdot["Cav\text{-}Gef"])) +V_{rear}\cdot(0.01\cdot[Gefa]) +V_{rear}\cdot((0.1\cdot["Rho\text{-}Gef"]-0.01\cdot[RhoAgtp]\cdot[Gefi]))$$

$$\frac{d([\text{Gefa}]\cdot V_{rear})}{dt} = +V_{rear}\cdot((0.1\cdot[\text{"Cav-Gef"}]-0.01\cdot[\text{Cav1i}]\cdot[\text{Gefa}])) -V_{rear}\cdot((0.1\cdot[\text{Gefa}]\cdot[\text{RhoAgdp}]-0.01\cdot[\text{"Rho-Gef"}])) -V_{rear}\cdot(0.01\cdot[\text{Gefa}])$$

$$\frac{d([\text{p190GAPi}]\cdot V_{rear})}{dt} = -V_{rear}\cdot((0.01\cdot[\text{Srca}]\cdot[\text{p190GAPi}]-0.001\cdot[\text{"Src-p190"}])) +V_{rear}\cdot((0.1\cdot[\text{p190GAP:RhoA}]-0.01\cdot[\text{p190GAPi}]\cdot[\text{RhoAgdp}]))$$

$$\frac{d([\text{"Src-p190"}]\cdot V_{rear})}{dt} = +V_{rear}\cdot((0.01\cdot[\text{Srca}]\cdot[\text{p190GAPi}]-0.001\cdot[\text{"Src-p190"}])) -V_{rear}\cdot((0.01\cdot[\text{"Src-p190"}]-0.001\cdot[\text{Srci}]\cdot[\text{p190GAPa}]))$$

$$\frac{d([\text{p190GAPa}]\cdot V_{rear})}{dt} = +V_{rear}\cdot((0.01\cdot[\text{"Src-p190"}]-0.001\cdot[\text{Srci}]\cdot[\text{p190GAPa}])) -V_{rear}\cdot((0.001\cdot[\text{p190GAPa}]\cdot[\text{RhoAgtp}]-0.0001\cdot[\text{p190GAP:RhoA}]))$$

$$\frac{d([\text{Actomyo.High}]\cdot V_{rear})}{dt} = -V_{rear}\cdot(0.01\cdot[\text{Actomyo.High}]) +V_{rear}\cdot(1e\text{-}005\cdot[\text{pMLCa}]\cdot[\text{Actomyo.Low}]\cdot[\text{Actinf}])$$

$$\frac{d([\text{Polcont.High}]\cdot V_{rear})}{dt} = -V_{rear}\cdot(0.001\cdot[\text{Polcont.High}]) +V_{rear}\cdot(0.0001\cdot[\text{Polystiff.High}]\cdot[\text{Polcont.Low}])$$

$$\frac{d([\text{Polcont.Low}]\cdot V_{rear})}{dt} = +V_{rear}\cdot(0.001\cdot[\text{Polcont.High}]) -V_{rear}\cdot(0.0001\cdot[\text{Polystiff.High}]\cdot[\text{Polcont.Low}])$$

$$\frac{d([\text{Recoil.Fast}]\cdot V_{rear})}{dt} = +V_{rear}\cdot((1e\text{-}005\cdot[\text{Actinf}]\cdot[\text{Actomyo.High}]\cdot[\text{Recoil.Slow}]-1e\text{-}006\cdot[\text{Actinf}]\cdot[\text{Actomyo.High}]\cdot[\text{Recoil.Fast}])) -V_{rear}\cdot(0.01\cdot[\text{Recoil.Fast}])$$

$$\frac{d([\text{Tension.D}]\cdot V_{rear})}{dt} = +V_{rear}\cdot((0.0001\cdot[\text{Tension.I}]\cdot[\text{Recoil.Fast}]-1e\text{-}005\cdot[\text{Tension.D}]\cdot[\text{Recoil.Fast}])) -V_{rear}\cdot(0.01\cdot[\text{Tension.D}]) +V_{rear}\cdot(1e\text{-}006\cdot[\text{Polcont.High}]\cdot[\text{Tension.I}])$$

$$\frac{d([\text{Tension.I}]\cdot V_{rear})}{dt} = -V_{rear}\cdot((0.0001\cdot[\text{Tension.I}]\cdot[\text{Recoil.Fast}]-1e\text{-}005\cdot[\text{Tension.D}]\cdot[\text{Recoil.Fast}])) +V_{rear}\cdot(0.01\cdot[\text{Tension.D}]) -V_{rear}\cdot(1e\text{-}006\cdot[\text{Polcont.High}]\cdot[\text{Tension.I}])$$

$$\frac{d([\text{Actomyo.Low}]\cdot V_{rear})}{dt} = +V_{rear}\cdot(0.01\cdot[\text{Actomyo.High}]) -V_{rear}\cdot(1e\text{-}005\cdot[\text{pMLCa}]\cdot[\text{Actomyo.Low}]\cdot[\text{Actinf}])$$

$$\frac{d([\text{Recoil.Slow}]\cdot V_{rear})}{dt} = -V_{rear}\cdot((1e\text{-}005\cdot[\text{Actinf}]\cdot[\text{Actomyo.High}]\cdot[\text{Recoil.Slow}]-1e\text{-}006\cdot[\text{Actinf}]\cdot[\text{Actomyo.High}]\cdot[\text{Recoil.Fast}])) +V_{rear}\cdot(0.01\cdot[\text{Recoil.Fast}])$$

$$\frac{d([\text{p190GAP:RhoA}]\cdot V_{rear})}{dt} = +V_{rear}\cdot((0.001\cdot[\text{p190GAPa}]\cdot[\text{RhoAgtp}]-0.0001\cdot[\text{p190GAP:RhoA}])) -V_{rear}\cdot((0.1\cdot[\text{p190GAP:RhoA}]-0.01\cdot[\text{p190GAPi}]\cdot[\text{RhoAgdp}]))$$

$$\frac{d([\text{"Rho-Gef"}]\cdot V_{rear})}{dt} = +V_{rear}\cdot((0.1\cdot[\text{Gefa}]\cdot[\text{RhoAgdp}]-0.01\cdot[\text{"Rho-Gef"}])) -V_{rear}\cdot((0.1\cdot[\text{"Rho-Gef"}]-0.01\cdot[\text{RhoAgtp}]\cdot[\text{Gefi}]))$$

$$\frac{d([\text{"Cava-Src"}]\cdot V_{rear})}{dt} = +V_{rear}\cdot((1e\text{-}006\cdot[\text{Cav1a}]\cdot[\text{Srca}]-1e\text{-}007\cdot[\text{"Cava-Src"}])) -V_{rear}\cdot((1e\text{-}006\cdot[\text{"Cava-Src"}]-1e\text{-}007\cdot[\text{Cav1i}]\cdot[\text{Srci}]))$$

$$\frac{d([\text{"Pkn2-Actin"}]\cdot V_{rear})}{dt} = +V_{rear}\cdot((0.001\cdot[\text{PKN2a}]\cdot[\text{Actinag}]-0.0001\cdot[\text{"Pkn2-Actin"}])) -V_{rear}\cdot((0.001\cdot[\text{"Pkn2-Actin"}]-0.0001\cdot[\text{PKN2i}]\cdot[\text{Actinf}]))$$

Figure Legends

Figure 1: Cell rear dynamics in matrix directed cells.

(A) Left: A2780 ovarian cancer cells expressing mEmerald-Lifeact were seeded in 3D cell-derived matrix (CDM) for 4 hours before spinning disk confocal microscopy. Single z-slice stills from movies are shown 300s apart. Dashed yellow line indicates the position of the rearmost part of the cell in the first frame; Top right: Matrix Stiffness measurements immediately in front of and behind cells migrating in CDM assessed by AFM (10μm polystyrene bead mounted to the cantilever; each cell's measurement joined by a black line, N=20 cells analysed across 3 repeats); Bottom right: Orientation of migration in untreated matrix shown by rose plot (N>35 cells across 3 repeats). (B) Left: 3D CDM were locally softened using trypsin-coated magnetic beads to generate gradient CDMs, and A2780 cells expressing mEmerald-Lifeact seeded and imaged as in (A; cells between ~500 and 1500μm from the softened area were imaged); Top right: Average stiffness measurements in CDM relative to softened area area assessed by AFM before seeding of cells (3 separate CDMs analysed with 25-100 readings per area; Bottom right: Orientation of migration with respect to area of locally softened matrix (at 360°) shown by rose plot (N>35 cells across 3 repeats). (C) Left: A2780 cells expressing mEmerald-Lifeact were seeded onto 2D FN-coated durotactic gradients for 16 hours and imaged as in (A); Top right: AFM measurement of stiffness of 2D durotactic gradients (4-10nm tip; N=3); Bottom right: Orientation of migration with respect to the gradient shown by rose plot (N=58 cells across 3 repeats). (D) Representative images from optical trap membrane tether based analysis of membrane tension. Rear and front images of the same cells taken in different fields of view; white dotted line indicates separation of images. (E) Left: Paired trap force measurements at the front and rear of cells on durotactic gradients (N=29 cells across 3 repeats); Right: Paired trap force measurements at the front and rear of polarised cells migrating on uniform stiff gradients (N=10 cells across 3 repeats). (F) Left, centre: Representative cells migrating in CDM stained with Flipper-TR membrane tension probe ~30 minutes prior to FLIM imaging where (Left) shows photon counts per pixel and (Centre) shows FLIM lifetime per pixel with a 16-colour look up table (LUT) applied as shown; Right: Pairwise average Flipper-TR lifetime in manually identified membrane regions at the front and rear of cells (N=9 cells across 3 repeats, note lower lifetime corresponds to lower membrane tension). Yellow arrows indicate direction of movement. *, $p < 0.05$; **, $p < 0.01$; ****, $p < 0.0001$; ns, not significant.

Figure 2: Low membrane tension promotes caveolae formation at the rear of fast moving cells in 3D and durotactic gradients.

(A) Left: A2780 cells expressing EGFP-cavin-1 and mCherry-caveolin-1 were seeded and imaged as in Fig. 1(A) Right: Pairwise Pearson's correlation coefficient for co-localisation of EGFP-cavin-1 and mCherry-caveolin-1 in rear compared to peri-nuclear regions (mean values shown above, N=28 cells across 2 repeats analysed). (B) A2780 cells expressing Lifeact-EGFP and mCherry-caveolin-1 were seeded and imaged as in Fig. 1(A), maximum intensity projection (MIP) shown for whole cell (left), individual Z-slices for rear regions panel (right). (C) Left: A2780 cells expressing mCherry-caveolin-1 were seeded onto 2D durotactic gradients and imaged as in Figure 1C (yellow line indicates outline of the cell); Right: orientation of caveolae with respect to the gradient shown by rose plot (N=58 cells across 3 repeats). (D, E) A2780 (D) or N15A (E) cell spheroids within collagen and fibronectin hydrogels were incubated for 24h to allow individual cells invade the local ECM. Left: Cells stained for F-actin (phalloidin) and Cavin-1 showing the spheroid (edge denoted by yellow dotted line) and an individual invading cells (yellow dotted box); Inset: Higher resolution image of the highlighted individual invading cells; MIPs of Z-stacks shown captured by long distance spinning disc confocal microscopy. (F) Pairwise quantification of normalised rear and nuclear Cavin-1 intensity in individual invading A2780 and N15 cells away from spheroids, N>8 cells analysed form 3 different spheroids. (G) A2780 cell seeded in 3D CDM and fixed and stained for F-actin, cavin-1 and EHD2; whole cell and separately captured zoomed rear MIPs of confocal stacks shown. (H) Fluorescence image of A2780 cells expressing mCherry-Caveolin-1 allows targeting of single cells. Serial Transmitted electron microscopy (sTEM, 100 nm) of

the exact same cell is displayed (middle panels). Manual segmentation of the nucleus, the plasma membrane and caveolae is performed and displayed as a 3D model over the entire cell. Both caveolae connected to the plasma membrane (yellow) and caveolae-associated vesicles (pink) were segmented (segm. + sTEM image). Both structures were merged in yellow in the overall model. An individual sTEM image is presented. Insets show higher resolution images of multilobed (arrows) or membrane-attached (arrowhead) caveolae (different z-section of the same cells). Scale bar 500nm (inset: 100nm). ***, $p < 0.001$; ****, $p < 0.0001$.

Figure 3: Increasing membrane tension abrogates rear caveolae formation and forward translocation.

(A) A2780 cells expressing Lifeact-EGFP and mCherry-caveolin-1 were seeded into 3D CDM and imaged by spinning disk confocal microscopy before and during hypo-osmotic shock (0.5Xmedia), and after recovery in isotonic media. (B) Quantification of rear mCherry-caveolin-1 intensity before and during osmotic shock, and after recovery in isotonic medium. N=12 cells analysed across 3 repeats, SEM bars shown. (C) Top left: A2780 cells expressing mCherry-caveolin-1 were seeded as in (A) and imaged in osmotic shock (0.5Xmedia) and recovery isotonic media every 30-60 seconds immediately post- media change using Definite Focus; Top right: quantification of average normalised mCherry-caveolin-1 intensity in 10% rear mask (white inset in images) and rest of cell regions over time following osmotic to isotonic switch (N=17 cells across 3 repeats, error bars show SEM, fitted quadratic curves showed in red and blue); Bottom: Montage of zoomed, 90˚ rotated rear region (highlighted by yellow box) immediately prior to and every 30s post- osmotic-isotonic switch showing mCherry-caveolin-1 accumulation. (D) Left: A2780 cells seeded for 4 hours in 3D CDM expressing GFP-membrane (left), Ezrin wild type (WT, centre) or Ezrin constitutively active (CA, right) and imaged for a 5 minute timelapse to assess rear retraction; Centre: Pairwise quantification of normalised peak Ezrin WT (left) and CA (right) intensity within front and rear regions (N>32 cells per condition across 3 repeats); Right: Quantification of average rear forward movement during 5 minute timelapse of cells expressing GFP membrane, Ezrin WT and CA (N >39 cells per condition across 3 repeats). (E) Left: A2780 cells expressing GFP membrane, Ezrin WT or CA seeded in 3D CDM for 4 hours, fixed with PFA and stained for endogenous F-actin (phalloidin) and cavin-1, MITs of Z-stacks shown for merged (top) and cavin-1 (bottom) channels; Centre: Quantification of rear/nuclear peak caveolin-1 staining intensity ratio for cells expressing GFP membrane, Ezrin WT and CA (N>11 cells per condition across 3 repeats); Right: Paired trap force measurements at the front and rear of cells expressing CFP Ezrin-CA on durotactic gradients (N=10 cells across 3 repeats). **, $p < 0.01$; ****, $p < 0.0001$; ns, not significant.

Figure 4: Caveolae activate RhoA at the cell rear to control contractility and F-actin architecture.

(A) Left: Lifeact-mRFP expressing, control/caveolin-1 knockdown A2780 cells were plated in 3D CDM and retraction of the cell rear over 5 minutes measured by spinning disk confocal microscopy; Right: forward movement of cells over a 5 minute timelapse (N>74 cells per condition across 3 repeats). (B) Active RhoA location biosensor GFP-AHPH expressing A2780 cells were seeded in 3D CDM, fixed after 6 hours and stained for endogenous caveolin-1, Z-stacks were captured by confocal microscopy (MIP shown). (C) Cell treated as in (B) imaged at high resolution, Pearson correlation 0.52; Spearman's rank 0.65. (D) Left: Ratiometric FRET imaging of control or caveolin-1 knockdown A2780 cells expressing Raichu-RhoA migrating in 3D CDM. Right: Quantification of ratiometric FRET in caveolin-1 knockdown cells (N>36 cells per condition across 3 repeats). (E) Quantification of ratiometric FRET of Raichu-RhoA expressing control and osmotic shock (0.5xmedia) treated cells in 3D CDM (N>27 cells per condition across 3 repeats). (F) Left: Control or caveolin-1 knockdown A2780 cells were seeded into 3D CDM and fixed after 4 hours, F-actin was visualized using SiR-actin and confocal imaging (MIPs are shown); Right: Ratio of F-actin intensity of the rear / front of cell (N>17 cells per condition across 3 repeats). (G) Control or RhoA knockdown A2780 cells were seeded into 3D CDM and fixed after 4 hours, F-actin was visualized using SiR-actin and confocal imaging (MIPs are shown). (H) Control, ROCK1 or ROCK2 knockdown cells were seeded into 3D CDM and fixed after 4 hours; F-actin was visualized using SiR-actin and confocal imaging, high resolution MIPs of rear cell regions shown. (I) Quantification of rear

/ front peak F-actin staining intensity of control and RhoA knockdown cells (N=10 cells per condition across 3 repeats). (J) Quantification of rear / front peak F-actin staining intensity of control, ROCK1 and ROCK2 knockdown cells (N>17 cells per condition across 3 repeats). (K) Left: Control (left) and caveolin-1 knockdown (right) Emerald-Lifeact expressing A2780 cells seeded in 3D CDM for 4 hours and imaged by spinning disc confocal microscopy for 5 minutes prior to- (top) and 5 minutes post- (bottom) treatment with 1 µM H1152; Right: Quantification of rear movement of control and caveolin-1 knockdown cells during 5 minute timelapses pre- and post- H1152 treatment (N=21 cells per condition across 3 repeats, note positive values correspond to forward movement and negative values to backwards movement of the rear). ***, $p < 0.001$; ****, $p < 0.0001$.

Figure 5: Ect2 is recruited by caveolae to activate RhoA

(A) Left, centre: Control (left) and Ect2 knockdown (centre) A2780 cells expressing membrane-targeted Raichu-RhoA were seeded in 3D CDM for 4 hours and imaged by spinning-disc microscopy for 5 minutes timecourses to assess forward rear membrane translocation; Right: Quantification of average forward rear movement during 5 minute timecourse of control, Ect2, Vav-2 and PLEKHG5 knockdown cells (N>46 cells per condition across 3 repeats). (B) Left: Ratiometric FRET imaging of control, Ect2, Vav-2 and PLEKHG5 knockdown cells treated as in (A); Right: Quantification of average rear region ratiometric FRET in control, Ect2, Vav-2 and PLEKHG5 knockdown cells (N>32 cells per condition across 3 repeats). (C) Left: Untransfected cells were seeded in 3D-CDM for 4 hours, fixed with PFA and stained for endogenous nuclei (Hoescht), F-Actin (phalloidin), Ect2 and Cavin-1, MIPs of whole cell and separately captured zoomed rear region shown for the merged, cavin-1 and Ect2 channels right: Quantification of peak Ect2 staining intensity in rear, nuclear and front regions of the same cell (linked by black dashed line, N=17 cells across 3 repeats). (D) Left: Control (left) and individual caveolin-1-A knockdown cells (right) were seeded in 3D CDM for 4 hours, fixed with PFA and stained for endogenous F-actin (phalloidin) and Ect2, MIPs of Z-stacks shown for merged (top) and Ect2 (bottom) channels; Right: quantification of rear peak / leading edge peak Ect2 intensity levels of control and caveolin-1 knockdown cells (N>20 cells per condition across 3 repeats). ***, $p < 0.001$; ****, $p < 0.0001$; ns, not significant.

Figure 6: Mathematical modelling implicates a positive feedback based mechanism of rear retraction.

(A) Schematic summary of key rear retraction events for migrating cells in 3D or durotaxis. (B) Wiring diagram of mechanical and protein-protein signalling interactions which leads to coordinated retraction, upon which the ODE model and simulations are based. (C) Simulations output of rear recoil speed (% activity) against time with polarized substrate stiffness remaining at 100% (red) or at 0% throughout the time course (yellow), or transitioning from 100% to 0% (gradient to uniform, blue, hidden by red line) or 0% to 100% (uniform to gradient, green) at time t = 4000s. (D) Simulation outputs for rear recoil speed and F-actin alignment (% activity) for unperturbed, RhoA and caveolae knockdown initial conditions. (E) In silico simulation of the reversible osmotic shock assay, where membrane tension is increased at t = 4000s and returned to basal level at t = 7000s; rear recoil speed and caveolae formation shown. (F) Predictive simulation of Y-27632 treatment effect on caveolae dynamics/rear recoil speed, where at t = 5000s ROCK1/PKN-2 inactivation rates are greatly increased. (G) Predictive simulation of 'global' cytochalasin-D treatment on caveolae dynamics/rear recoil speed, where at t = 5000s F-actin turnover rate is greatly increased. (H) As in G but for 'local' cytochalasin-D, where at t = 5000s F-actin turnover rate is moderately increased.

Figure 7: F-actin stability and contractility maintain caveolar rear localization in migrating cells.

(A) mCherry-caveolin-1 expressing A2780 cells were seeded onto 3D CDM and imaged after 4 hours by spinning disk confocal microscopy before (left panels) and after treatment with 10 µM Y27632. (B) Quantification of rear caveolin-1 intensity of cells as in (A) (N=23 cells across 3 repeats). (C) Control or ROCK1 knockdown cells were seeded into 3D CDM and fixed after 4 hours and stained for endogenous cavin-1 and F-actin (phalloidin), MIPs of confocal z-stacks are shown. (D) Line profile based

quantification of cavin-1 intensity across the rear portion of cells as in (C) (N>20 cells per condition across 3 repeats). (E) Distance in µm of peak cavin-1 intensity from the rear of cells as in (C) (N>20 cells per condition across 3 repeats). (F) Control or individual Ect2 knockdown cells were seeded into 3D CDM, fixed after 4 hours and stained for nuclei (Hoescht), F-Actin (phalloidin) and cavin-1, MIPs of confocal z-stacks are shown. (G) Left,: Cells were seeded in 3D CDM and stained with Flipper-TR > 15 minutes prior to imaging as in Fig. 1F, same cell shown pre- (left) and ~30 minutes post- (right) Y27632 treatment where (top) shows photon counts per pixel, (bottom) shows FLIM lifetime per pixel with a 16-colour look up table (LUT) applied as shown; Right: Unpaired (top) and pairwise (bottom) average Rear – Front Flipper-TR lifetime difference in manually identified membrane regions pre- and post-Y27632 treatment (N>9 cells pre condition across 3 repeats). (H) A2780 cells expressing Lifeact-GFP and mCherry-caveolin-1 were seeded onto 3D CDM and imaged after 4 hours in the presence of caged-CytoD (50 µM) before and after uncaging of a specific region behind the cell rear (indicated by yellow box). Right: Quantification of rear caveolin-1 intensity in cells before and 10 minutes after uncaging (N>30 cells per condition across 3 repeats). **, $p < 0.01$; ***, $p < 0.001$; ****, $p < 0.0001$.

Figure

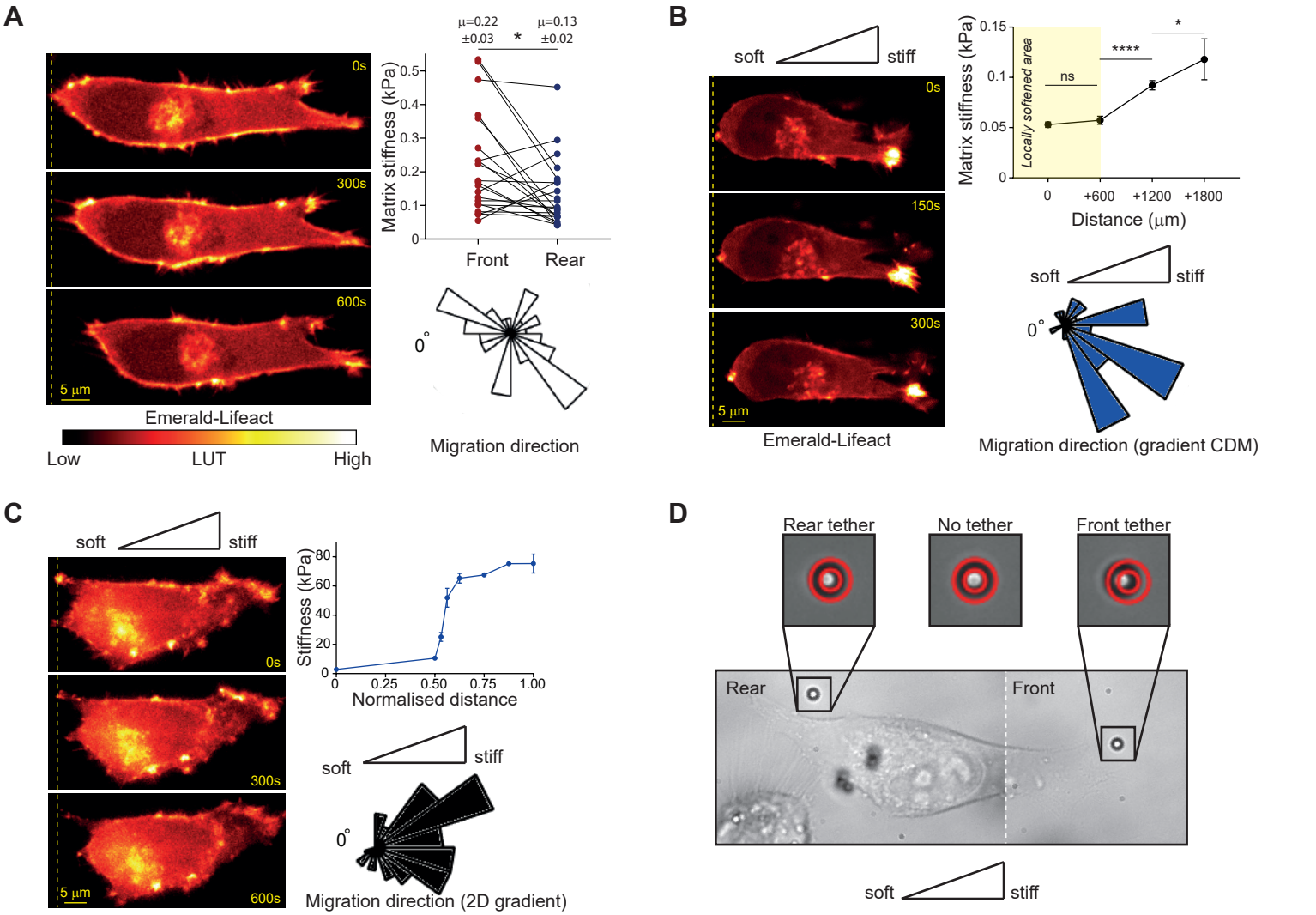

Figure 1 Hetmanski et al

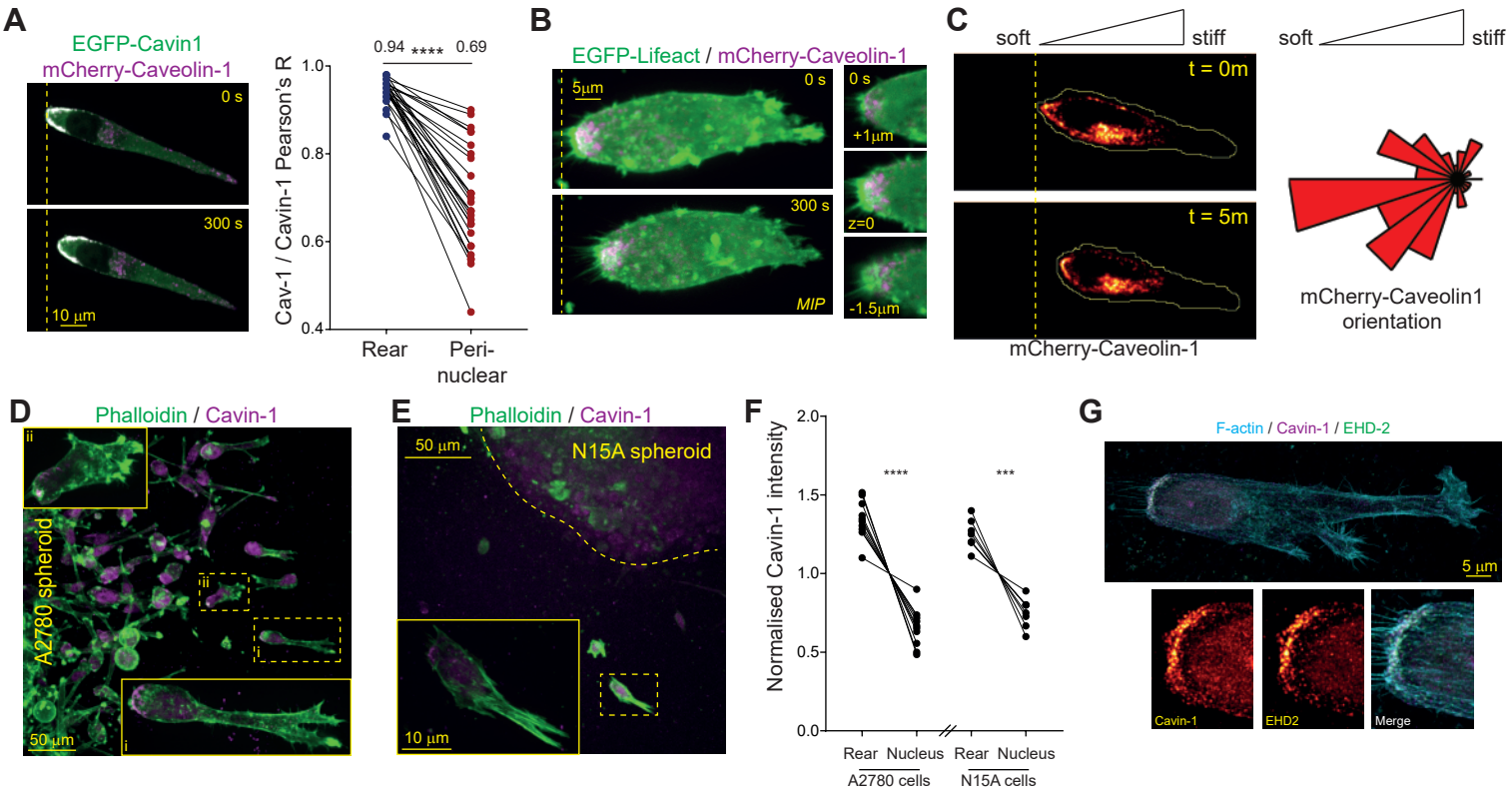
A
EGFP-Cavin1
mCherry-Caveolin-1
0 s
300 s
10 µm
0.94 **** 0.69
Cav-1 / Cavin-1 Pearson's R
1.0
0.8
0.6
0.4
Rear
Peri-nuclear
B
EGFP-Lifeact / mCherry-Caveolin-1
5µm
0 s
300 s
MIP
0 s
+1µm
z=0
-1.5µm
C
soft
stiff
t = 0m
t = 5m
mCherry-Caveolin-1
soft
stiff
mCherry-Caveolin1 orientation
D
Phalloidin / Cavin-1
A2780 spheroid
ii
iii
i
50 µm
E
Phalloidin / Cavin-1
50 µm
N15A spheroid
10 µm
F
Normalised Cavin-1 intensity
2.0
1.5
1.0
0.5
0.0
****
***
Rear
Nucleus
Rear
Nucleus
A2780 cells
N15A cells
G
F-actin / Cavin-1 / EHD-2
5 µm
Cavin-1
EHD2
Merge
H
Fluorescence (mCherry-Caveolin-1)
invasion
sTEM
Z
Nucleus
PM
Segmentation
Nucleus PM Caveolae
Nucleus Caveolae
Segm. + sTEM
Caveolae (open neck)
Caveolae
Nucleus
PM
Caveolae
Segmentation
Nucleus
PM
Caveolae
sTEM
100nm
500nm

Figure

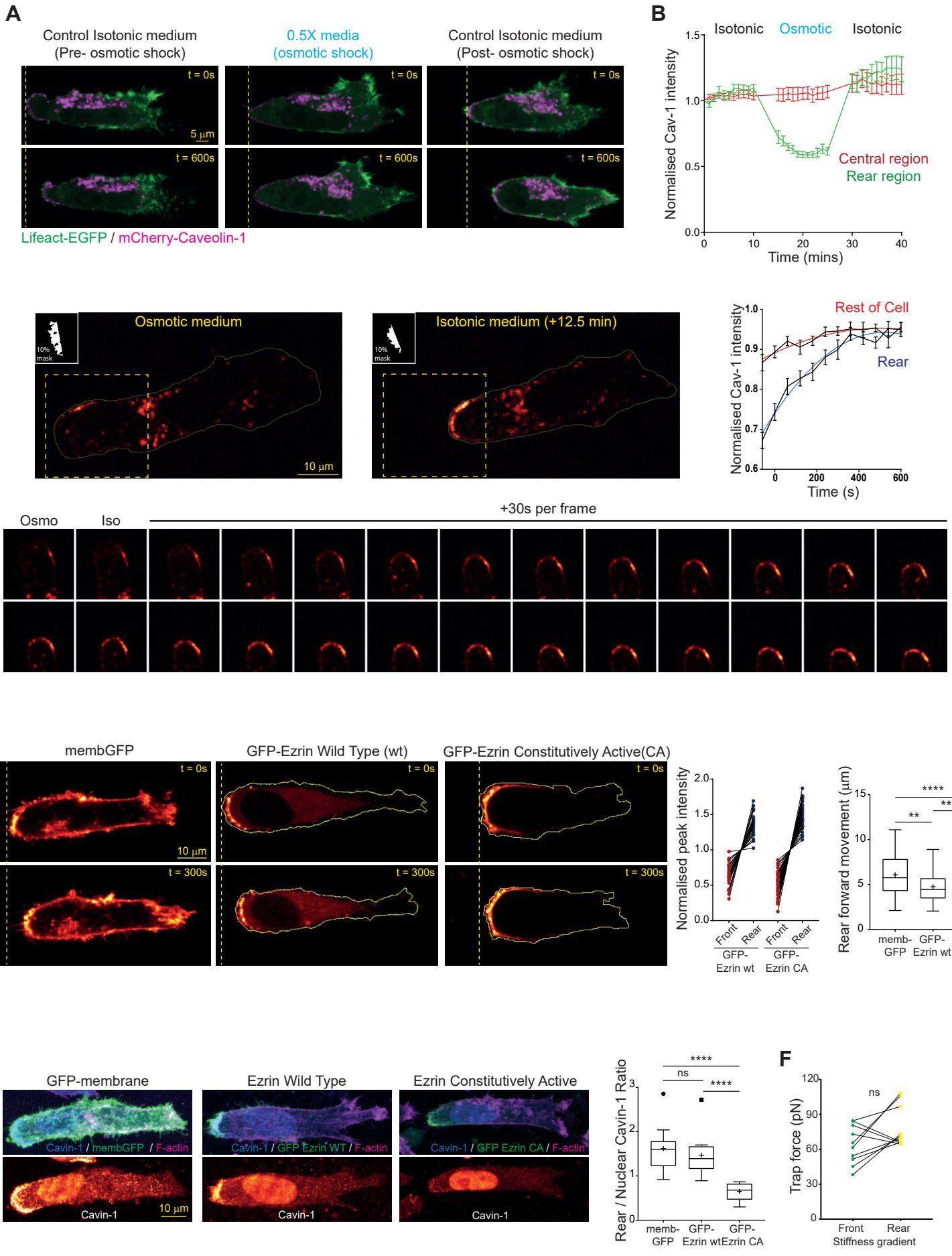

Figure 3 Hetmanski et al

Figure

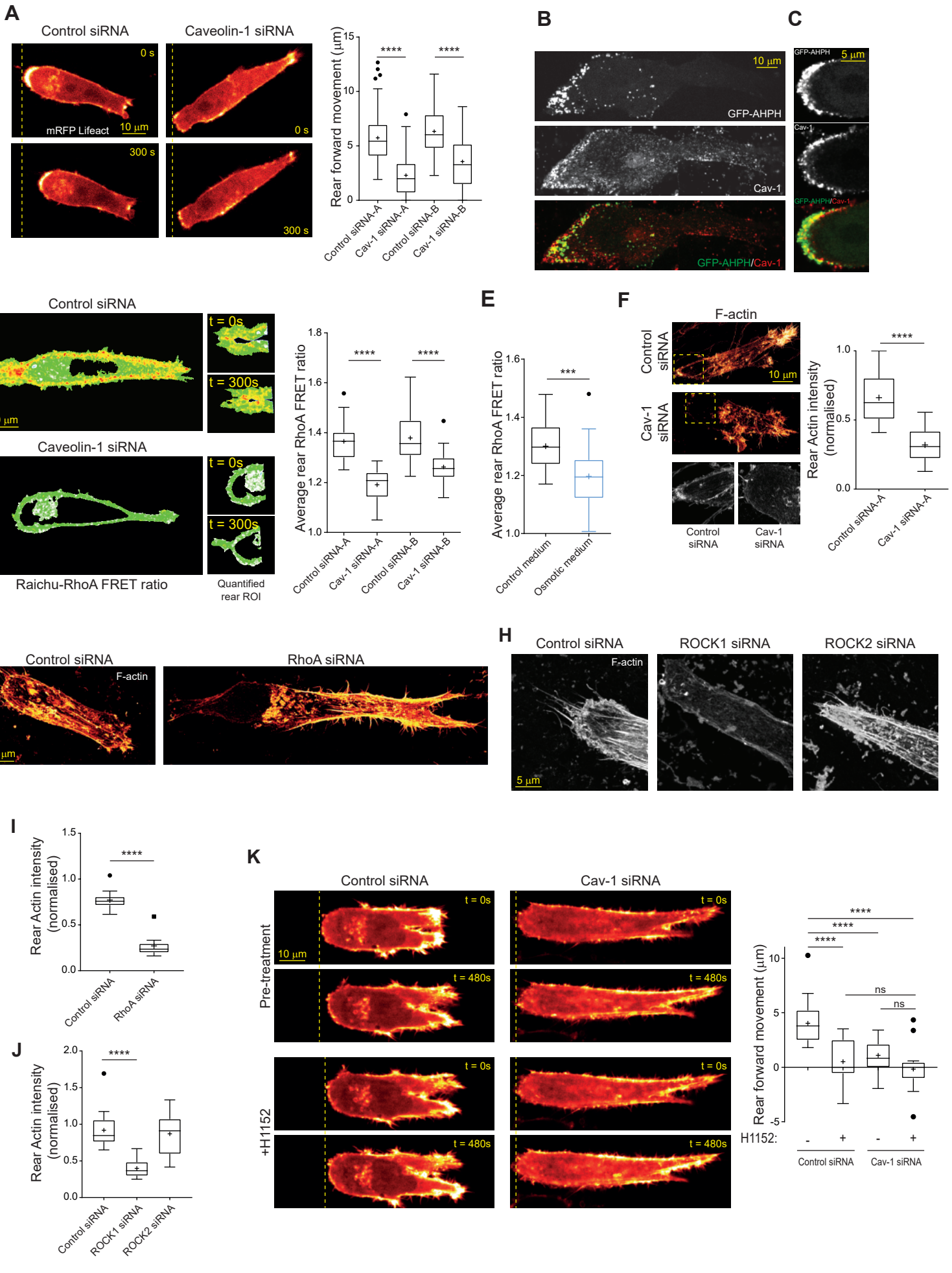

Figure 4 Hetmanski et al

Figure

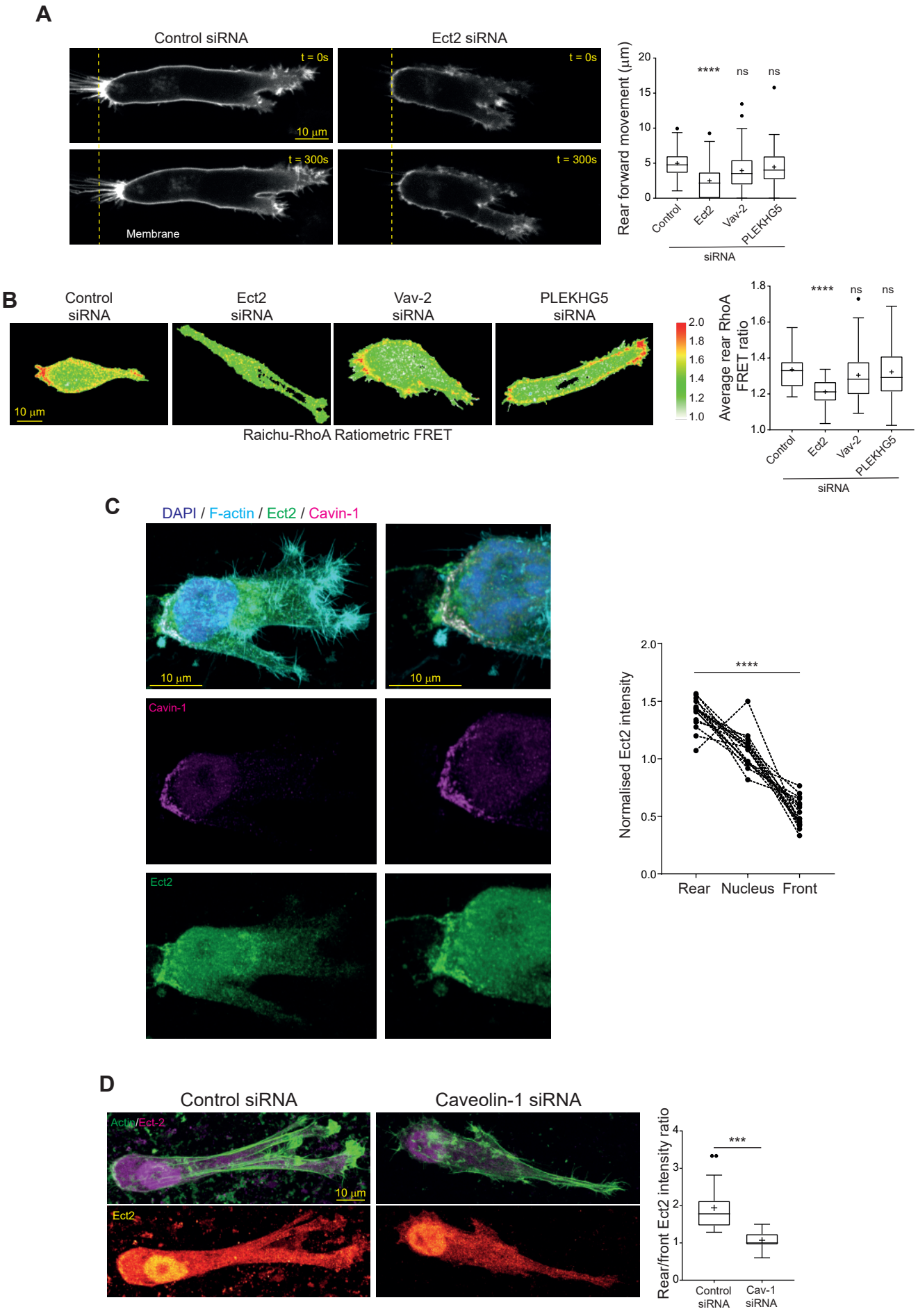

Figure 5 Hetmanski et al

Figure

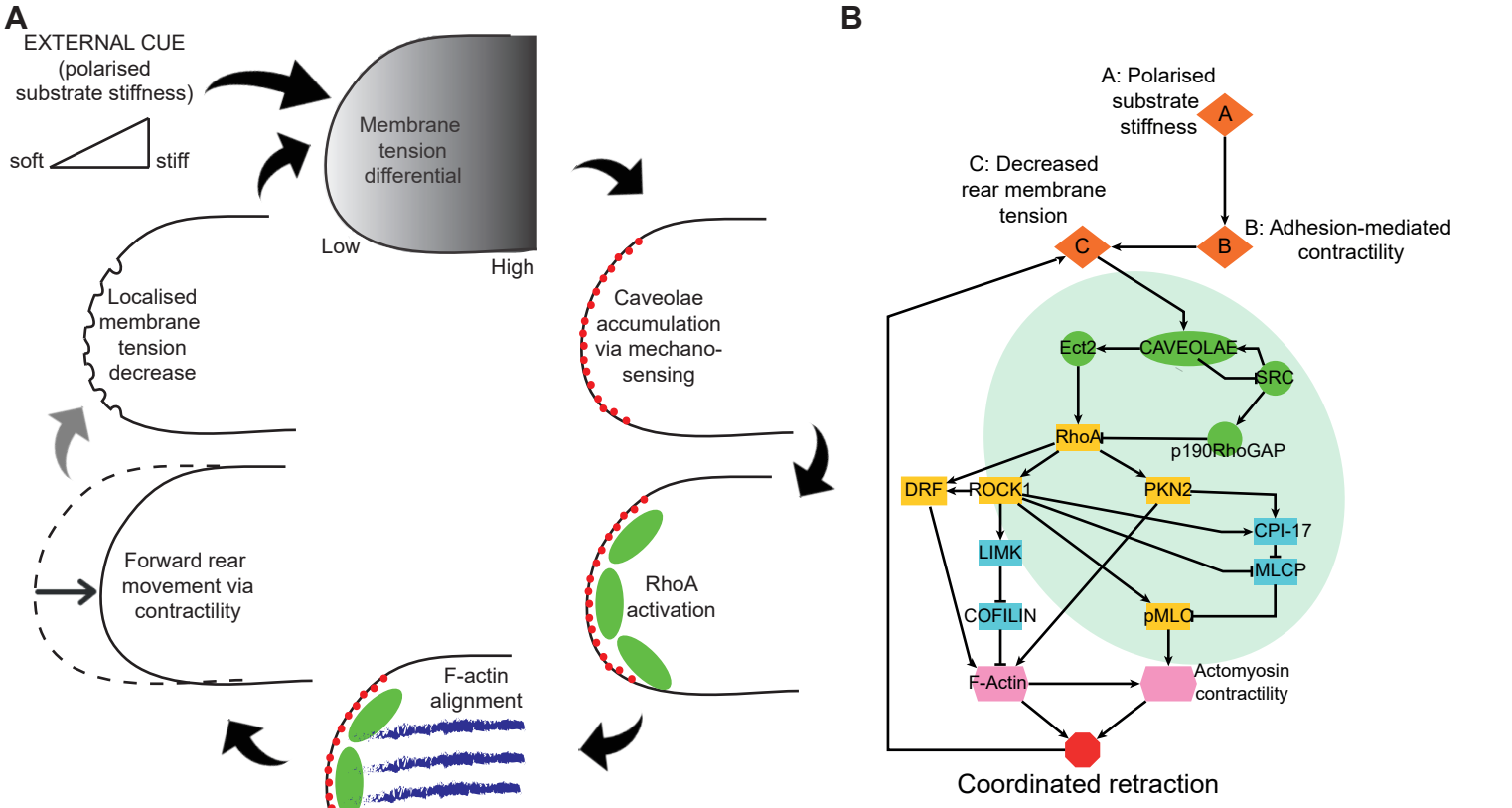

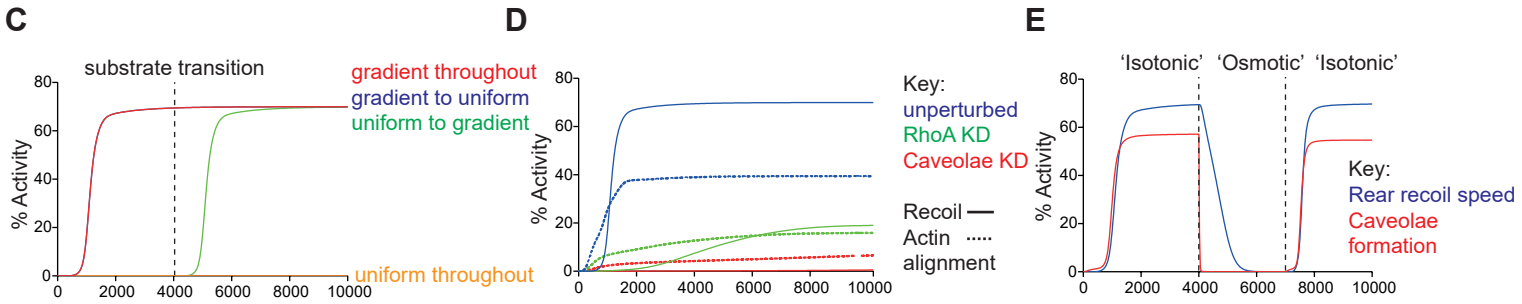

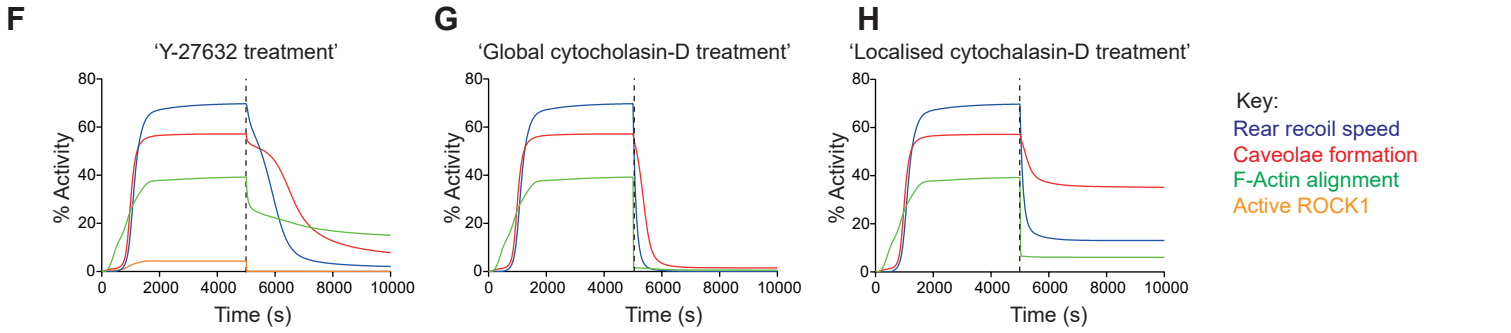

Figure 6 Hetmanski et al

Figure

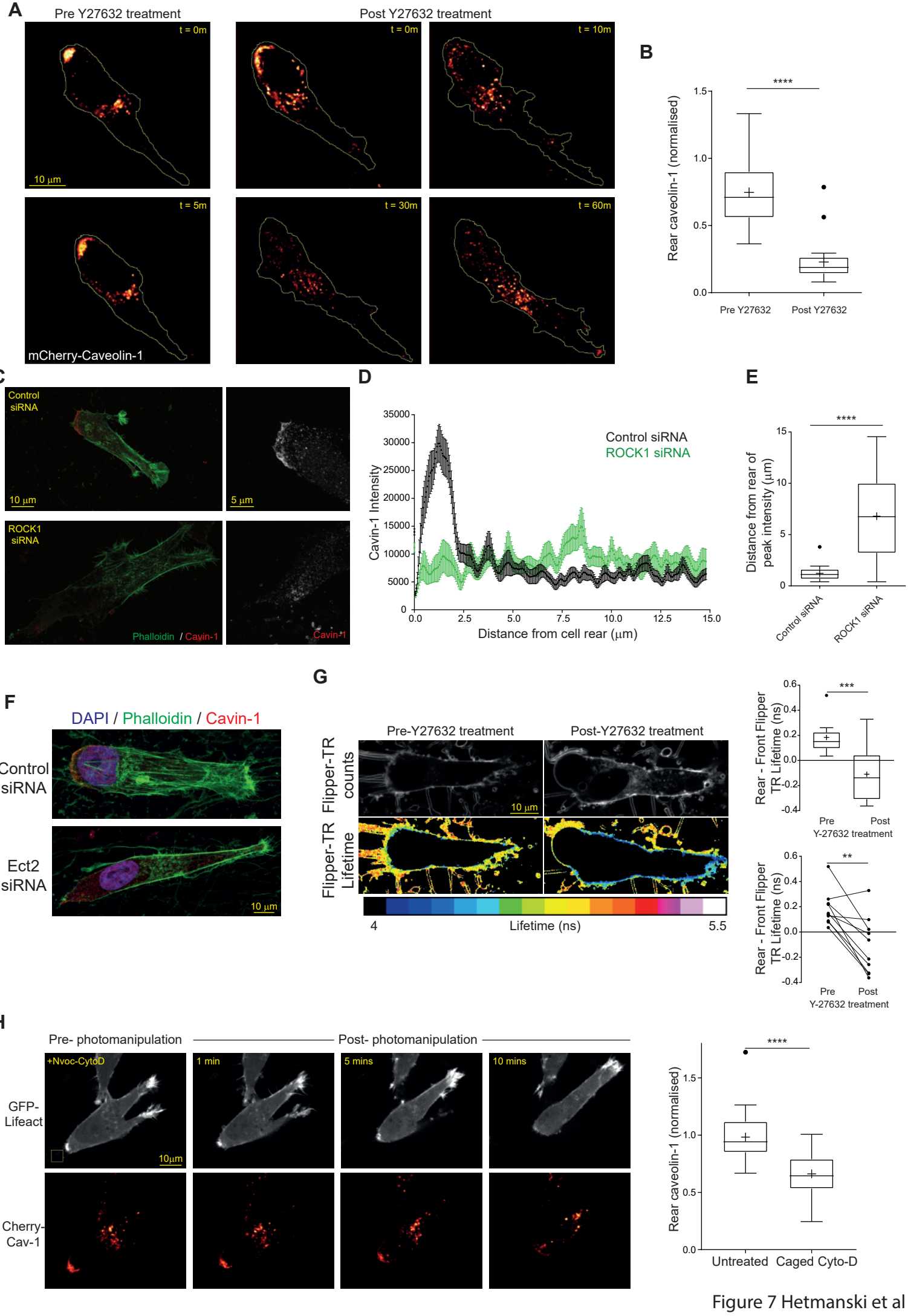

Figure 7 Hetmanski et al

Supplementary information

Figure S1-S7

Movie S1-7

Supplementary Figure Legends

Figure S1: 3D migration in fibrillar matrix.

(A) A2780 cells seeded within 3D CDM. Representative single plane images above, through and below the cell (top) and an xz projection s (bottom), where each dashed line denotes the relative positions of the single plane images. Cells/matrix were fixed and stained for fibronectin and F-actin (SiR-actin) prior to imaging with a Z step size of 0.27 µm. (B) A2780 cells moving in an unperturbed CDM (left) or a locally softened CDM (right), representative maximum intensity projections (MIPs) shown. Cells were fixed and imaged as in A. (C) H1299 cells were seeded onto FN-coated 2D durotactic gradients for 16 hours and imaged, orientation of migration with respect to the gradient is shown by rose plot. (D) Left: A2780 cells expressing farnesyl-EGFP (GFPmembrane) were seeded onto 3D CDM and imaged as in Fig. 1A. Right: Pairwise quantification of normalised GFP-membrane peak intensity at the front and rear of A2780 cells (N=33 cells across 3 repeats). (E) A2780 expressing Lifeact-GFP stained with lipophilic dye (DiI) moving in 3D CDM. Timelapse of the cell rear captured using Zeiss Airyscan. (F) Trap force at the front and rear of unpaired cells on durotactic gradients, untreated glass and uniform stiff gels and single membrane measurements of unpolarised cells on uniform soft gels; N>31 cells per condition analysed across 3 repeats for gradient; N>18 per condition across 3 repeats for glass, N>12 cells per condition across 3 repeats for uniform stiff, N=6 cells across 2 repeats for uniform soft. (G) A2780 cells expressing EGFP-paxillin and mCherry-caveolin-1 were seeded in CDM for 4 hours then imaged for 5 minutes, 9 Z-planes imaged every 1µm by spinning-disc confocal microscopy, representative MIPs of merged (left) and paxillin (right) channels shown; Right: Pairwise quantification of number of adhesions in front/nucleus region compared to behind nucleus region, N=31 cells across 3 repeats. ****, $p<0.0001$.

Figure S2: Caveolae localization in cells in 3D matrix and durotactic gradients.

(A) H1299 cells expressing Lifeact-mEmerald and mCherry-caveolin-1 were seeded in 3D CDM and imaged as in Fig. 2(B). (B) H1299 non-small cell lung cancer cells were seeded in 3D CDM and fixed and stained for F-actin and cavin-1. MIPs of confocal stacks are shown. (C) A2780 cells seeded on a CDM locally softened via trypsin beads, fixed as in B and stained for F-actin (SiR-actin) and cavin-1. Representative MIP shown. (D) A2780 cells in 3D CDM were fixed and stained for endogenous caveolin-1. Representative MIP of confocal stacks are shown. (E) H1299 cells expressing Lifeact-mEmerald and mCherry-caveolin-1 were seeded on 2D durotactic gradients and imaged as in Fig. 2(C). (F) A2780 cells on 2D soft, stiff, or durotactic gradients of stiffness (all coated with fibronectin) stained for F-actin (phalloidin) and cavin-1. Representative MIP shown. (G) A2780 cells on 2D soft, stiff, or durotactic gradients of stiffness (all coated with fibronectin) stained for F-actin (SiR-actin) and caveolin-1. Representative MIP shown. (H) Orientation of caveolin-1 in cells as in (F) with respect to the stiffness gradient (N=30 cells across 3 repeats). (I) Average speed of A2780, H1299, Telomerase-immortalized fibroblasts (TIFs) or mouse embryonic fibroblasts (MEFs) cells in 3D CDM during 16 hours timelapse. (J) Average intensity of mCherry-caveolin-1 at the rear of A2780, H1299, MEF and TIF cells moving in 3D CDM. (K) TIFs or MEFs were seeded in 3D CDM and fixed stained and imaged as in (B), representative images of poorly polarized highly spread morphology of TIFs and MEFs in 3D CDM. (L) Trap force measurements at the front and rear of elongated TIF cells, N=10 cells across 3 repeats. (M) TIFs and MEFs as in (K), displaying the polarised, shorter phenotype. (N) Morphology of TIFs and MEFs when undergoing rapid migration in 3D CDM. (O) Proportion of TIFs and MEFs that show elongated (typical) morphology versus shortened (rapid) morphology, and proportion of cells that exhibit high versus low/unpolarized cavin-1 at the cell rear. (P) A2780 cells expressing mEmerald-Lifeact and mCherry-caveolin-1 were imaged migrating in 3D CDM, and fixed and processed for Serial Block Face SEM (SBFSEM). The relative ease of data collection using SBFSEM meant that it was possible to generate correlative EM data from 9 different motile cells with sufficient resolution to allow identification of caveolae. A volume render of the EM data is compared with the light microscope image to show that the cell morphology has not been

affected by fixation. The enlargements show evidence of caveolae/multilobed caveolae (yellow arrowheads) at the rear of the cell, but no evidence of caveolae was seen in the peri-nuclear region. ****, p<0.0001.

Figure S3: Increasing membrane tension supresses rear caveolae assembly in durotactic gradients and CDM.

(A) A2780 cells expressing Lifeact-EGFP and mCherry-caveolin-1 were seeded onto 2D durotactic gradients and imaged before and during osmotic shock treatment (0.5Xmedia). (B) A2780 cells were seeded onto CDM and treated with osmotic shock (0.5Xmedia) or isotonic media, before fixation, staining and imaging of endogenous caveolin-1. MIPs are shown. Yellow line indicates outline of the cell. Insets MIPs of the cell rear captured using high resolution imaging. (C) Distance of rear retraction of A2780 cells in isotonic versus hypo-osmotic shock in a 5 minute timelapse. N>61 cells per condition across 3 repeats. ****, p<0.0001.

Figure S4 Caveolae control rear retraction through RhoA-ROCK1/PKN2 actin organisation

(A) Caveolin-1 knockdown A2780 cells were plated in 3D CDM and speed of migration measured by timelapse microscopy over 16 hours. N=90 cells per condition across 3 repeats. (B) Representative images of control and caveolin-1 knockdown A2780 cells moving through 3D CDM. (C) Quantification of control and caveolin-1 knockdown cell length whilst migrating in 3D CDM. N=90 cells analysed per condition across 3 repeats. (D) Efficiency of knockdown of caveolin-1 in A2780 cells. (E) Efficiency of knockdown of caveolin-1 in H1299 cells. (F) Left: Lifeact-mRFP expressing, caveolin-1 knockdown H1299 cells were plated in 3D CDM, imaged by spinning disk confocal microscopy and retraction of the cell rear over 5 minutes measured. Right: Forward movement of H1299s cells over a 5 minute timelapse. N>74 cells per condition across 3 repeats. (G) Left: Control and EHD2 knockdown A2780 cells expressing Lifeact-EGFP and mCherry-caveolin-1 migrating in 3D CDM imaged by spinning disk confocal microscopy. Centre: Average migration speed of control and EHD2 knockdown cells migrating in 3D CDM for 16 hours. N=90 cells analysed per condition across 3 repeats. Top right: Distance of rear retraction of control and EHD2 knockdown A2780 cells in 3D CDM during a 5 minute timelapse N>80 cells per condition across 3 repeats. Bottom right: EHD2 knockdown efficiency in A2780 cells. (H) Left: Representative images of control and EHD2 knockdown A2780cells with coloured bars indicating cell length. Right: Quantification of control and EHD2 knockdown cell length whilst migrating in 3D CDM. N=90 cells analysed per condition across 3 repeats. (I) Active RhoA location biosensor GFP-AHPH expressing A2780 cells were seeded in 3D CDM and fixed after 6 hours. F-actin was visualized with SiR-actin, and cells imaged at high resolution. MIPs are shown. (J) Active RhoA location biosensor GFP-AHPH expressing A2780 cells were seeded on 2D durotactic gradients for 16 hours and imaged by spinning disk microscopy using a long working distance 63x objective. (K) Active RhoA location biosensor GFP-AHPH and mCherry-caveolin-1 expressing A2780 cells were seeded in 3D CDM and imaged by spinning disk confocal microscopy after 6 hours. (L) Raichu-RhoA in osmotic shock. (M) Left: Control or RhoA knockdown cells were seeded into 3D CDM and imaged by spinning disk confocal microscopy after 4 hours. Single z-slice stills from movies are shown 300s apart. Centre: Forward movement of control and RhoA knockdown cells over a 5 minute timelapse. N>54 cells per condition across 3 repeats. Right: RhoA knockdown efficiency in A2780 cells. (N) Control, ROCK1 or ROCK2 knockdown cells were seeded into 3D CDM and fixed after 4 hours. F-actin was visualized using SiR-actin and confocal imaging. MIPs are shown. (O) A2780 cells were seeded into 3D CDM and treated with Y27632 (10 µM) for 2 hours before fixation. F-actin (phalloidin) was visualized by confocal microscopy, MIPs shown. (P) Left: Speed of migration of A2780 cells in 3D CDM over 16 hour timelapse was analysed in control, ROCK1, ROCK2 and ROCK1+2 knockdown cells. N=90 cells analysed per condition across 3 repeats. Right: Efficiency of ROCK1 and ROCK2 knockdown in A2780 cells. (Q) Top left: Speed of migration of A2780 cells in 3D CDM over 16 hour timelapse was analysed in control, PKN1, PKN2 and PKN3 knockdown cells N=90 cells analysed per condition across 3 repeats. Top right: Effect of PKN2 knockdown on architecture of F-actin at the rear of A2780 cells migrating in 3D CDM (representative high resolution MIP shown). Bottom left: Efficiency of PKN1, PKN2 and PKN3 knockdown in A2780 cells, assessed using a pan-pPKN antibody. Quantification of blots from 3 independent experiments shown in graph. Bottom right: Efficiency of PKN2 knockdown in A2780 cells, assessed using a PKN2 specific antibody. ****, p<0.0001; *, p<0.05.

Figure S5: Systematic identification of GEFs activating RhoA at the cell rear

(A) Quantification of average speed of control, Ect2, Vav2, ARHGEF2, DOCK1, ELMO2 and PLEKHG5 A2780 cells in long-term (16h) migration in 3D CDM, N>60 cells per condition across 3 repeats, dashed line indicates

control mean. (B) Quantification of cell length ~20h after spreading for cells is in (A), N>60 cells per condition across 3 repeats. (C) Quantification of average speed of control and 2 individual Ect2 oligo knockdown A2780 cells, N=30 cells analysed per condition across 2 repeats. (D) Representative single control and Ect2 knockdown cells migrating in 3D CDM over 150 minutes. (E) Quantification of rear / front peak F-actin staining intensity of control, and Ect2 knockdown cells (individual oligos). (F) Efficiency of knockdown of Ect2, Vav2, ARHGEF2, DOCK1, ELMO2 and PLEKHG5 in A2780 cells. (G) Knockdown of Ect2 with individual siRNA oligos; #5 and #7 were used in subsequent experiments. ****, p<0.0001; *, p<0.05.

Figure S6: Model outputs are robust to wide parameter value ranges.

(A) Summary parameter sensitivity analysis showing normalised effect of all rates in the model on the rear retraction output. Parameters which have > 0.02 positive scaled effect on rear retraction are shown in green, parameters which have < 0.02 negative scaled effect shown in red, while all other parameters with less drastic effects are represented by the blue bars. (B) Range of rear retraction temporal dynamics given halving and doubling of the 9 most influential rates in the model (6 positive regulators in green, 3 negative regulators in red) showing general model outputs are robust to even large parameter alterations.

Figure S7: Effect of RhoA knockdown and CytoD on caveolae localization.

(A) Control and RhoA knockdown A2780 cells expressing mCherry-caveolin-1 were seeded into 3D CDM and imaged by spinning disk confocal microscopy after 4 hours. Single z-slice stills from movies are shown 300s apart. (B) Intensity of mCherry-caveolin-1 at the rear of cells as in (A) N=76 cells per condition across 3 repeats. (C) Control and RhoA knockdown cells were seeded into 3D CDM and fixed after 4 hours. Endogenous F-actin, caveolin-1 and cavin-1 were visualized, representative MIPs shown. (D) High resolution images of endogenous cavin-1 at the rear of control and RhoA knockdown A2780 cells migrating in 3D CDM as in (C). (E) Quantification of the average rear/front cavin-1 intensity ratio of control and individual oligo Ect2 knockdown A2780 cells. (F) A2780 cells expressing Lifeact-EGFP and mCherry-caveolin-1 were seeded in 3D CDM for 4 hours before and imaging in the presence of 2μM CytoD. (G) Caged CytoD is a photoactivatable derivative of the potent actin disruptor Cytochalasin D (CytoD), which possesses nitroveratryloxycarbonyl (Nvoc) photoremovable group located at the bioactive hydroxyl group of CytoD. The Nvoc group inhibits the binding activity of CytoD, which can be restored upon photolysis reaction with light exposure under microscopy setups. Upon light exposure, caged CytoD enables dosed delivery of CytoD in living cells at time scale of seconds and with subcellular resolution. (H) A2780 cells expressing Lifeact-GFP and mCherry-caveolin-1 were seeded onto 3D CDM and imaged after 4 hours in the absence of caged-CytoD before and after photomanipulation of a specific region behind the cell rear (indicated by yellow box, as in Figure 6G). ****, p<0.0001.

Supplementary Movie Legends

Movie S1: (Part I) A2780 cell expressing mEmerald-Lifeact migrating in 3D CDM over 10 minutes, with a Red-hot LUT applied. (Part II) A2780 cell expressing mEmerald-Lifeact migrating for 5 minutes in a non-uniform CDM with a (trypsinised) softened region to the left and the unperturbed stiffer region to the right. (Part III) A2780 cell expressing mEmerald-Lifeact migrating from soft (left) to stiff (right) on a gradient poly-acrylamide gel for 10 minutes.

Movie S2: A2780 cell expressing farnesyl-EGFP (GFP membrane) migrating in CDM over 5 minutes.

Movie S3: Single representative A2780, H1299, typical MEF, rapid MEF, typical TIF and rapid TIF migrating over 2 hours in CDM.

Movie S4: A2780 cell expressing mCherry-caveolin-1 (magenta) and mEmerald-Lifeact (green) imaged prior to fixation and processing for CLEM (see Figure S2P).

Movie S5: A2780 cell expressing Cherry-Cav-1 migrating in CDM in isotonic medium for 10 minutes, then subjected to osmotic shock for 10 minutes before medium reversion to isotonic conditions for a further 10 minutes.

Movie S6: A2780 cell expressing Cherry-Cav-1, migrating in CDM untreated for 5 minutes, then treated with Y-27632 and imaged for a further 60 minutes.

Movie S7: A2780 cell expressing Cherry-Cav-1 (magenta) and eGFP-Lifeact (green) migrating in CDM treated with 'caged' Cytochalasin-D which is photo-activated at t = 30s within the yellow box region.

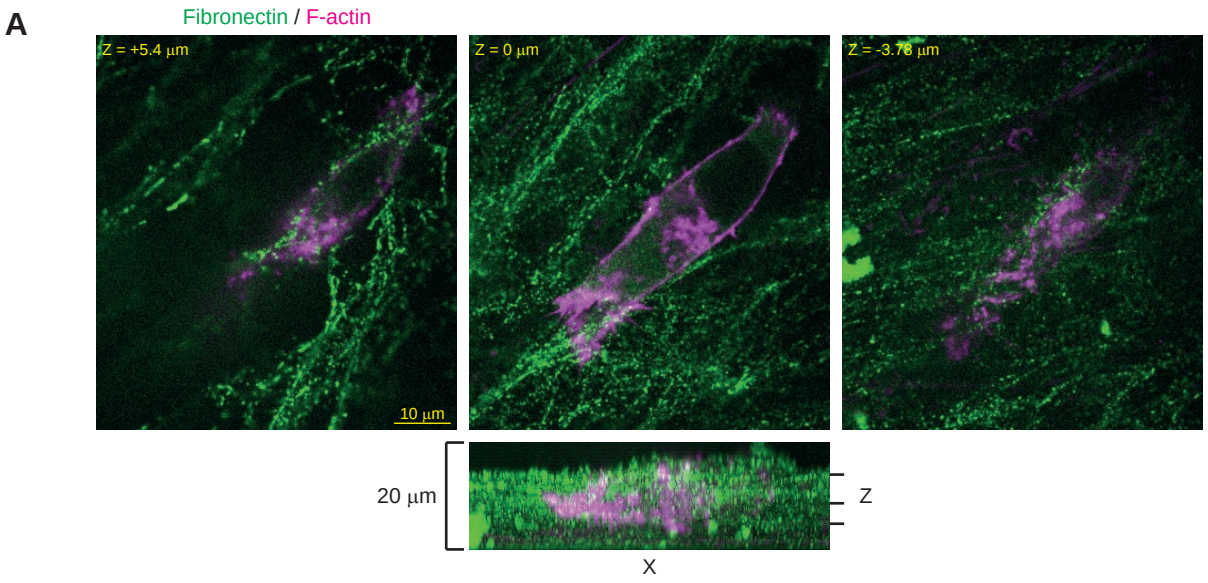

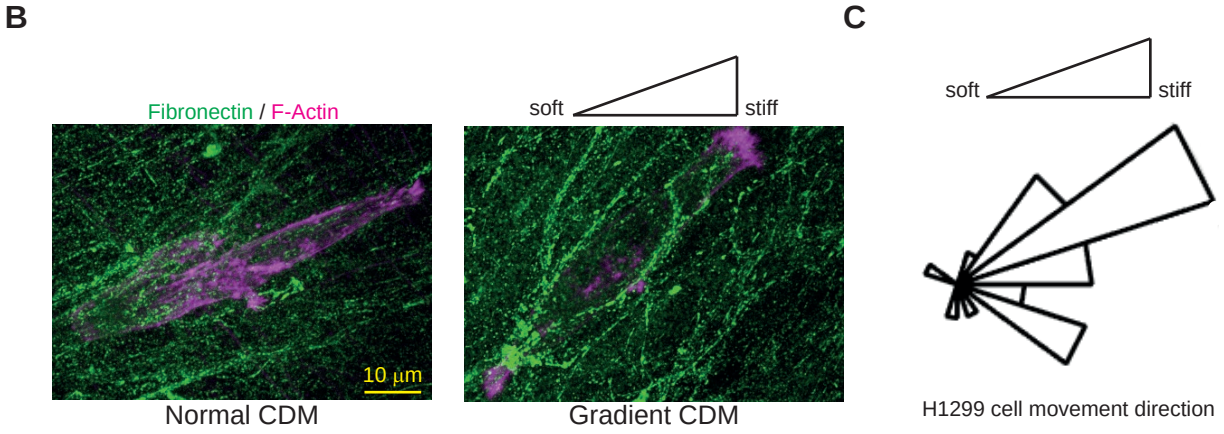

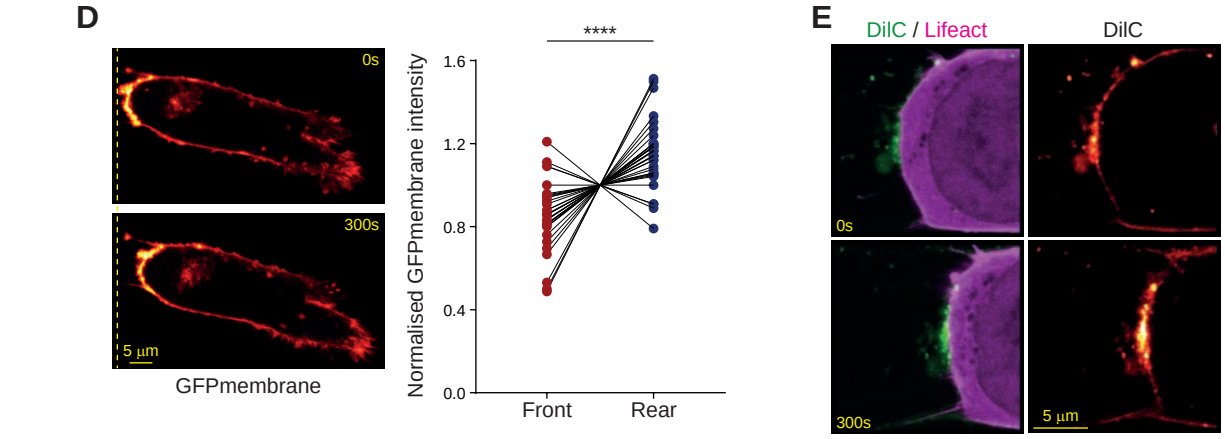

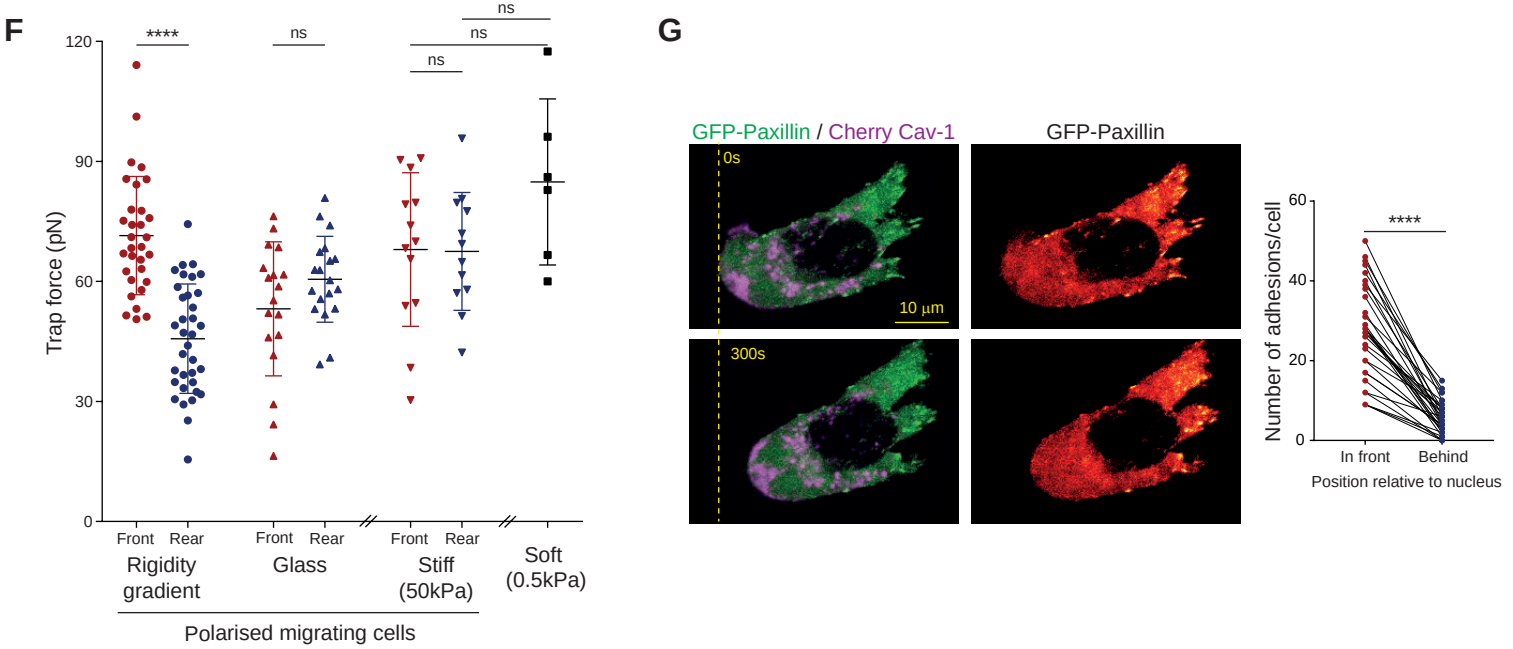

Figure S1 Hetmanski et al

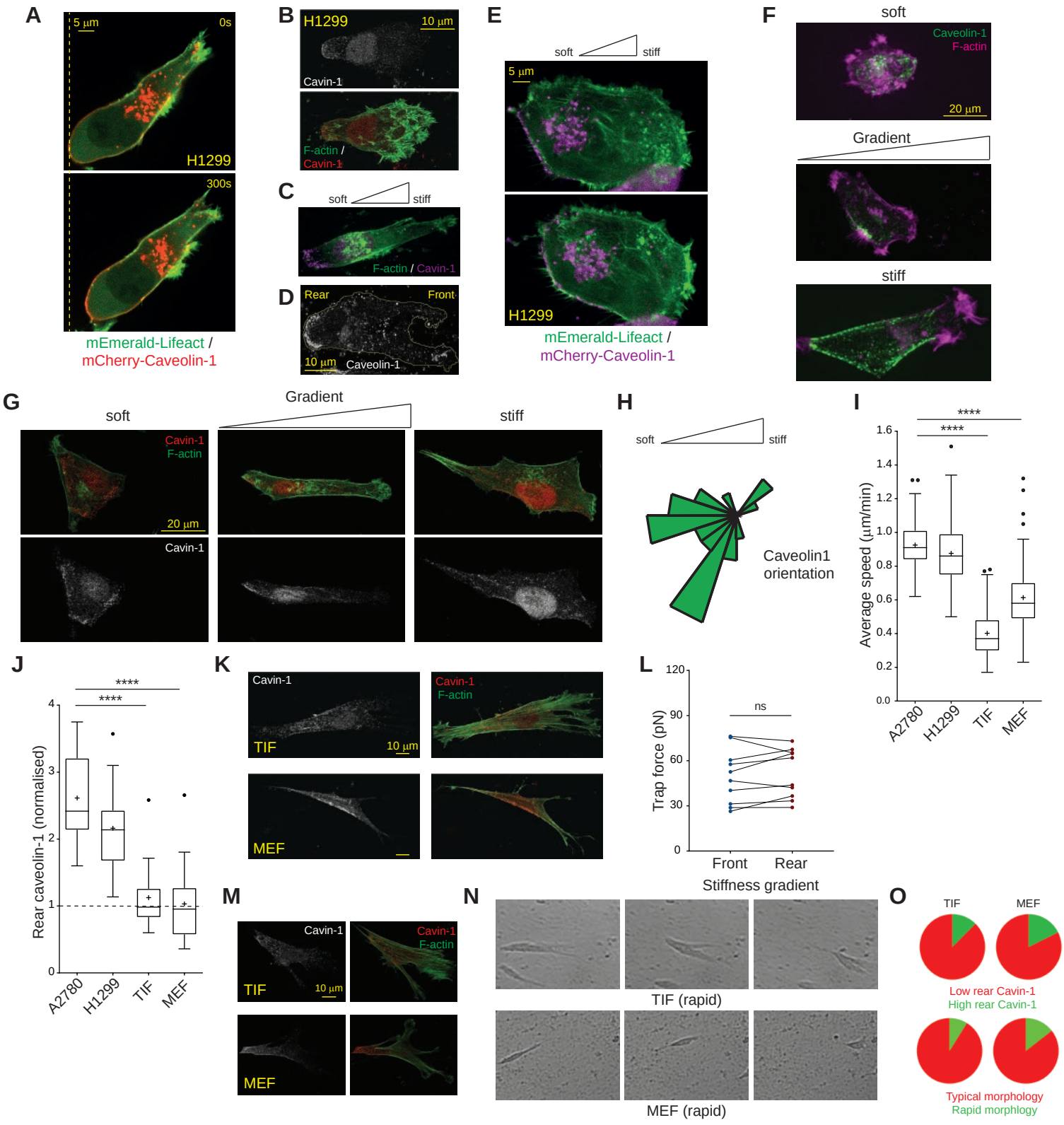

Figure S2 Hetmanski et al

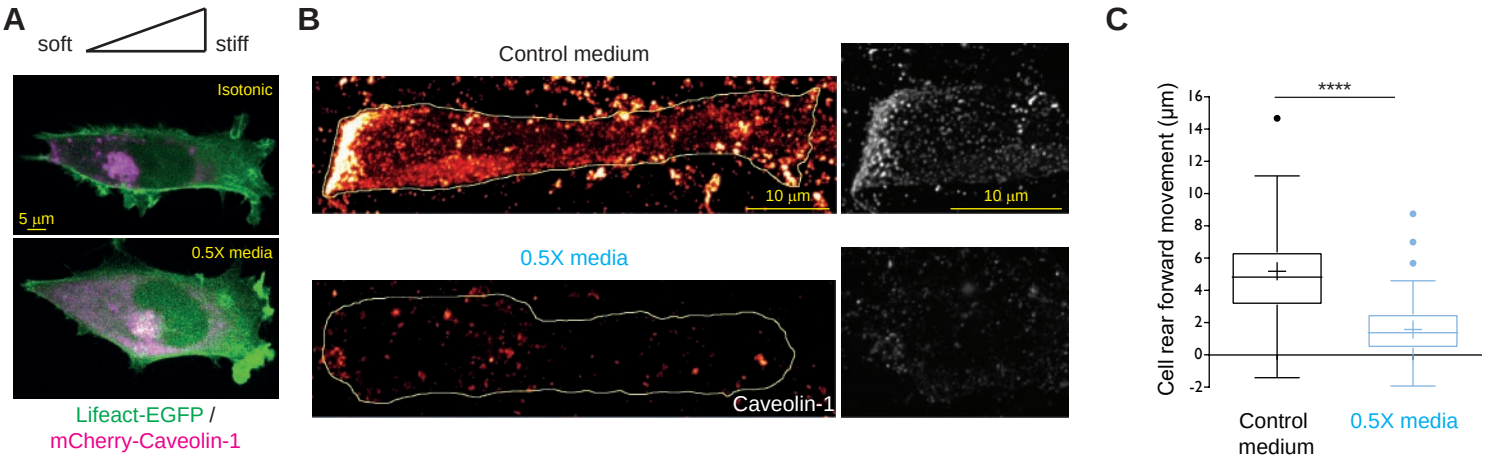

Figure S3 Hetmanski et al

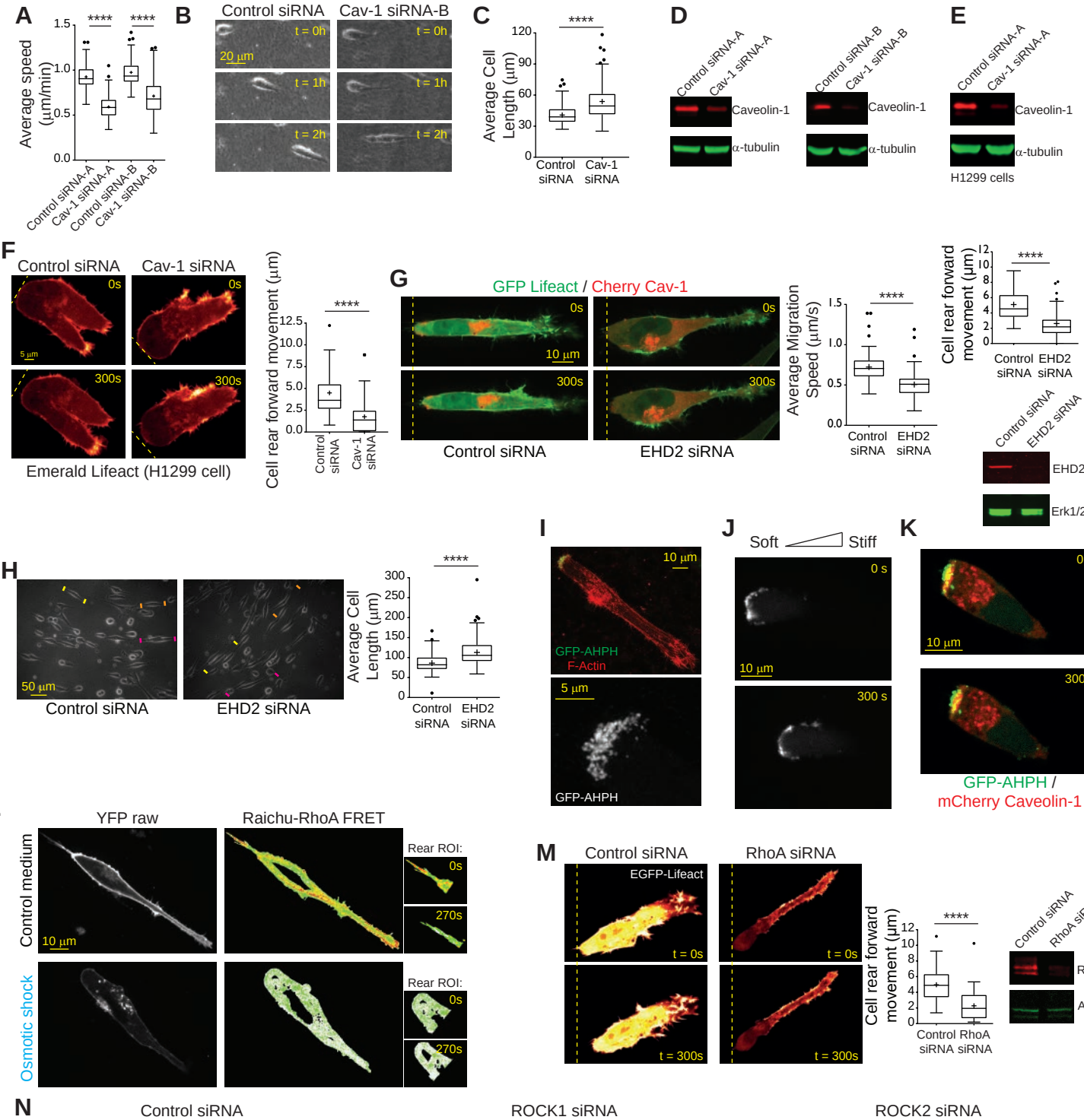

Figure S4 Hetmanski et al

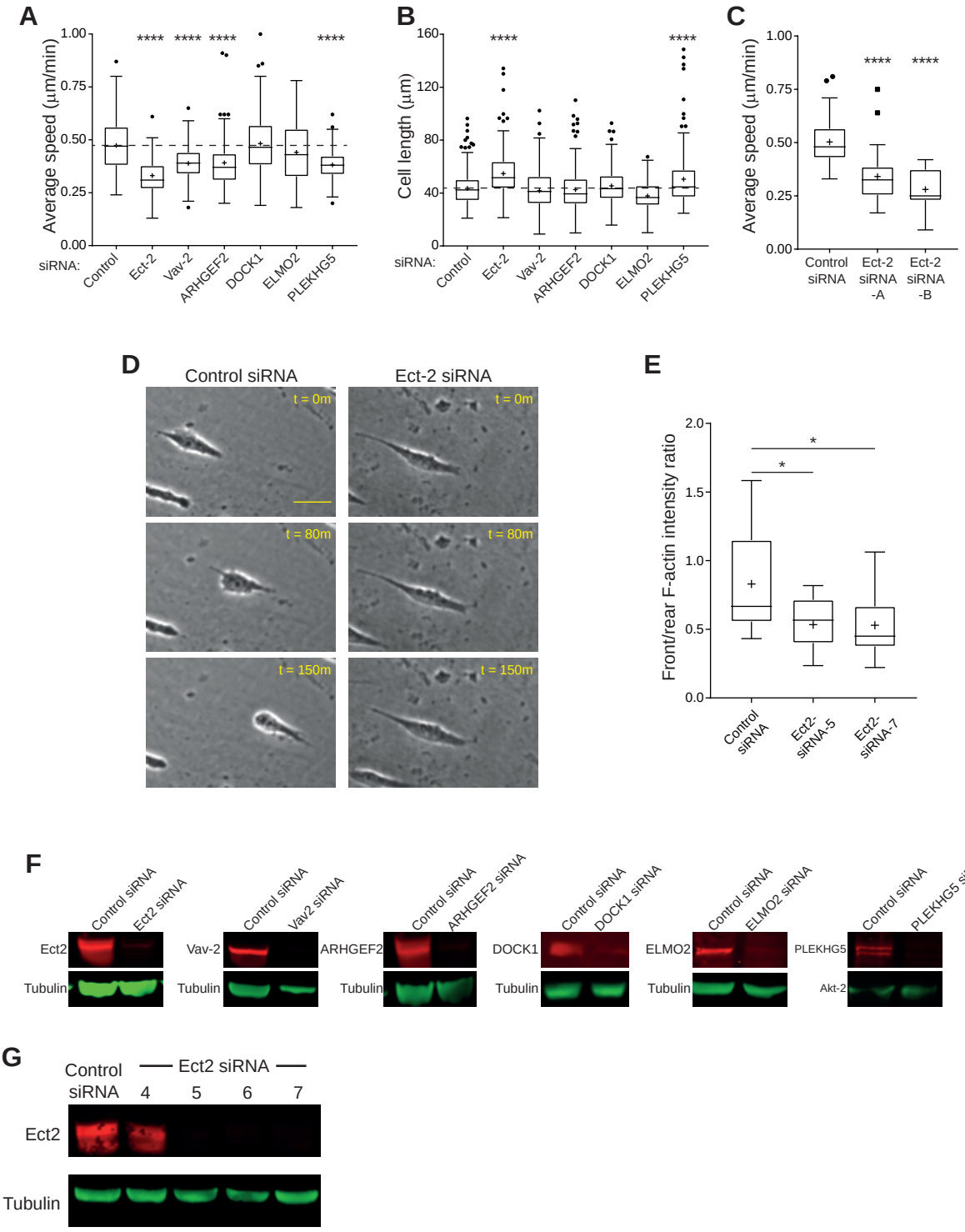

Figure S5 Hetmanski et al

A.

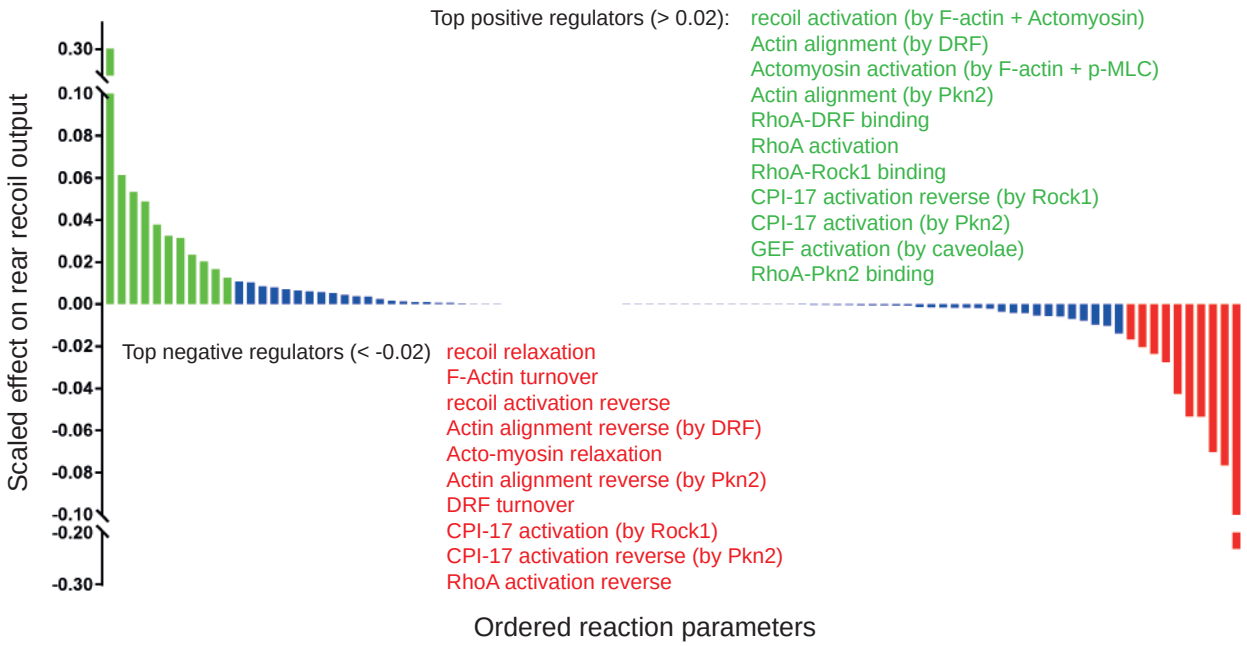

B.

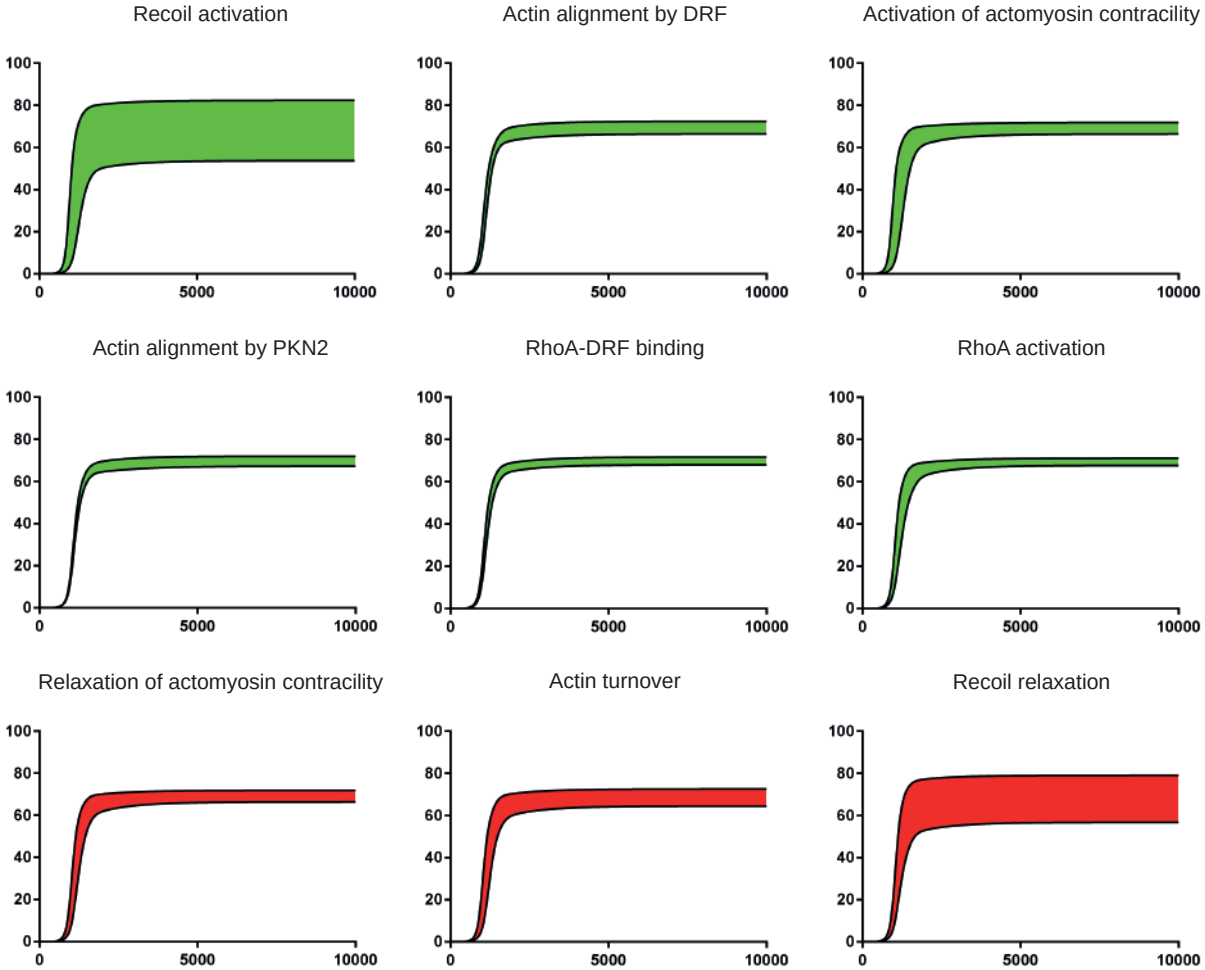

Figure S6 Hetmanski et al

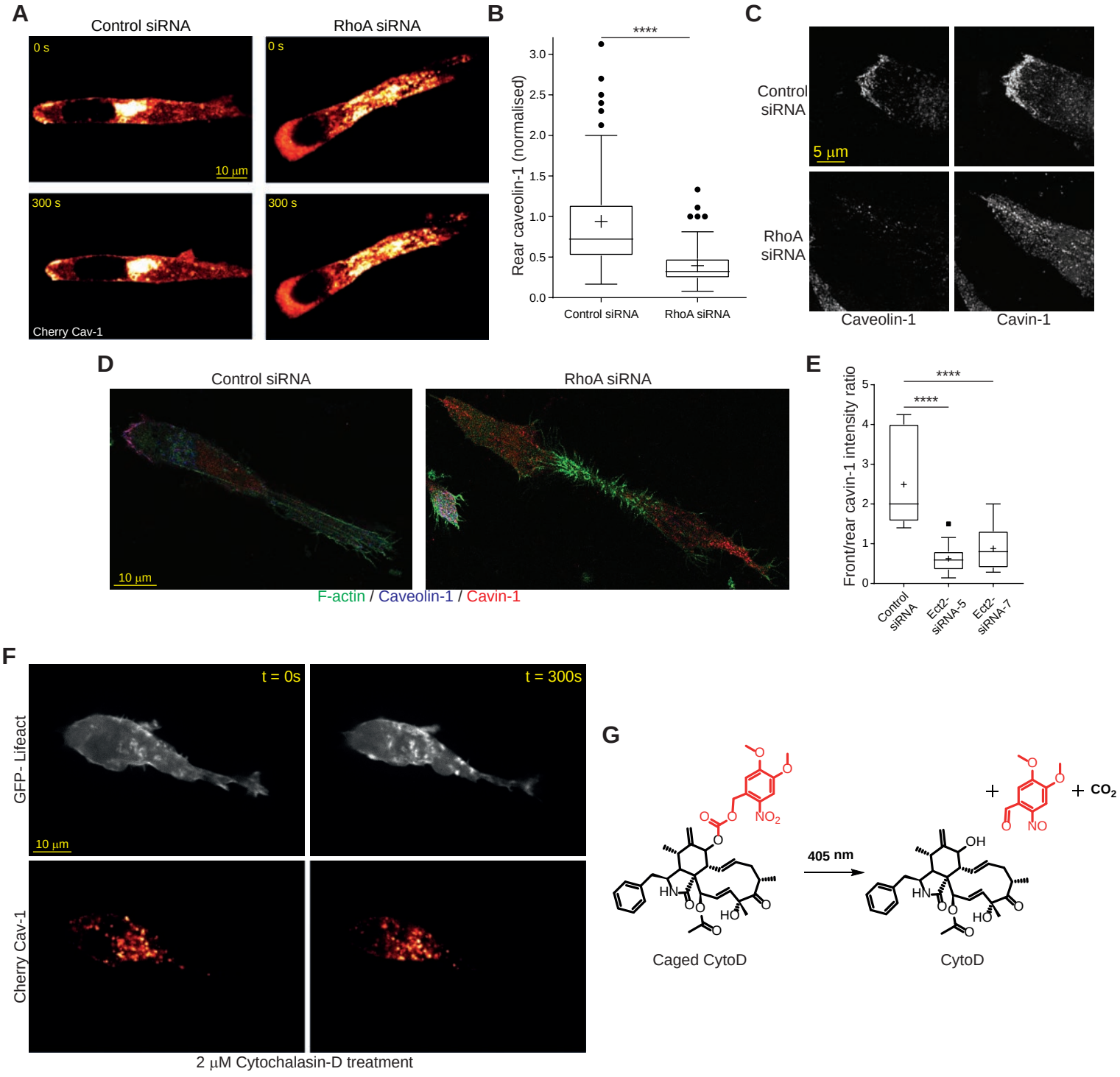

Figure S7 Hetmanski et al

Click here to access/download

Supplemental Videos and Spreadsheets

Movie S1.avi

Click here to access/download

Supplemental Videos and Spreadsheets

Movie S2.avi

Click here to access/download

Supplemental Videos and Spreadsheets

Movie S3.avi

Click here to access/download

Supplemental Videos and Spreadsheets

Movie S4.avi

Click here to access/download

Supplemental Videos and Spreadsheets

Movie S5.avi

Click here to access/download

Supplemental Videos and Spreadsheets

Movie S6.avi

Click here to access/download

Supplemental Videos and Spreadsheets

Movie S7.avi